ALMA MATER STUDIORUM — UNIVERSITÀ DI BOLOGNA

SCUOLA DI SCIENZE
Corso di Laurea Magistrale in Astrofisica e Cosmologia
Dipartimento di Fisica e Astronomia

A new void finder based on cosmic dynamics

Tesi di Laurea Magistrale

Candidato:
Carlo Cannarozzo

Relatore:
Chiar.mo
Prof. Lauro Moscardini

Co-relatore:
Dr. Federico Marulli

Sessione III
Anno Accademico 2015-2016

Ai miei genitori,
Ettore e Maria Rita.
A mia sorella,
Marcella.

Alla mia ragazza e collega,
Matilde.

Allo Zio.
"...'sti vuoti l'ama a ìnghiri!"

Once when Einstein was in Hollywood on a visit Chaplin drove him through the town. As the people on the sidewalks recognized two of their greatest, if very different, contemporaries, they gave them a tremendous reception which greatly astonished Einstein. "*They're cheering us both,*" said Chaplin: "*you because nobody understands you, and me because everybody understands me.*" There was a good-humoured pride in his remark, and at the same time a certain humility as at a recognition of the difference between ready popularity and lasting greatness.

Plesch, John (1947). *János: The Story of a Doctor*.

10.03.2016 - 10.03.2017

Table of Contents

Abstract

Cosmic voids are large empty regions of the Universe, having a huge range in size, from the so-called *minivoids*, with diameters around 3 Mpc, to *supervoids*, with diameters of few hundreds of Mpc. Voids separate filaments, sheets and haloes from each other, as predicted by numerical simulations in the framework of the *Cold Dark Matter* (CDM) models and confirmed by observations. They constitute a fundamental component of the *Cosmic Web*, accounting for about the 95% of the overall volume of the Universe. Cosmic voids point out the scale at which density fluctuations have decoupled from the Hubble flow and formed overdense regions, such as galaxy clusters (van de Weygaert and Platen, 2011). Because of their low-density nature, voids are powerful probes to underline several crucial aspects of the Universe. Indeed, their internal structures, shapes and other statistical properties such as number counts, clustering, density profiles and also their dynamics are supposed to be strongly dependent on *Dark Energy* (DE) properties. This implies that cosmic voids can be considered as laboratories for testing cosmological models and, in particular, to put constraints on DE and on the geometry of the Universe. Voids are formed from underdensities in the primordial field of density perturbations and, like clusters, may provide crucial information on the large scale structures. In addition, their underdense environment represents the ideal location to study galaxies in passive evolution, to investigate internal feedback phenomena in an environment where galaxy interactions are highly unlikely. On the other hand, precisely because of that pristine low-density environment, void sampling is not trivial. Indeed, Void Finders based on density, or even geometrical, criteria, generally suffer from significant shot noise uncertainties.

In this context, the main goal of this thesis is to implement a new Void Finder code based on a dynamical criterion, following the approach suggested by Elyiv et al. (2015). The method aims at sampling cosmic voids in Lagrangian coordinates, thus mitigating the uncertainties due to sparse sampling. The idea is to use tracers as *test particles*, reconstructing their orbits from the actual clustered configuration to a homogeneous and isotropic pristine distribution. This back-in-time evolution in the

displacement field can be performed adopting two different approaches. The first assumes the *Zel'dovich approximation* (Zel'dovich, 1970). In brief, the linear theory of density perturbations is applicable to a regime in which the *density contrast*, $\delta\rho/\rho$, is lower than unity. In the Lagrangian description of a cosmological fluid, one traces the path of a fluid element onto space and time. Given the position $\mathbf{q}$ of an element at t_0, its location at subsequent instants can be expressed in terms of the Lagrangian displacement field $\mathbf{\Psi}$. This approximation allows to extend the linear theory to the case of perturbations slightly larger than unity. Since objects have straight orbits in this approximation, in order to compute the displacement field we connect their Eulerian positions to those of a randomly distributed sample.

The second approach exploits the *two-point correlation function*, $\xi(r)$, that quantifies the clustering of a galaxy sample. It represents the excess in probability, dP, compared to that expected in a random distribution, of finding a pair of galaxies separated by a comoving distance r, in the two comoving volume elements dV_1 and dV_2. Although the local Universe is highly inhomogeneous, in an early epoch the space is supposed to be extremely homogeneous. This suggests that a practical way to trace galaxy orbits back in time is to relax their present spatial distribution to homogeneity, defined as a state in which the correlation function at all separations is zero.

Since, in both the approaches described above, the particle path depends on the initial random seeds, our Void Finder algorithm performs several reconstructions and then averages the obtained fields by using a Gaussian weighting. Then it computes the divergence field, $\mathbf{\Theta} = \nabla \cdot \mathbf{\Psi}$, that represents, by definition, the density at each point. We consider only the local minima with negative divergence. Each local minimum identifies a subvoid. In fact, a negative value of velocity field divergence implies the presence of a region acting as a sink of mass streamlines. Through a *watershed* method we can then "fill" the near subvoids in order to identify, eventually, a local void. The void centres are assumed to be the positions corresponding to the absolute minimum value of the divergence field inside each void. To estimate the void size, we calculate the *effective radius* of an equivalent spherical volume.

The new dynamical Void Finder implemented in this work has been included in the CosmoBolognaLib, a large set of Open Source C++/Python libraries for cosmological calculations (Marulli et al., 2016). In order to check the robustness of our new Void Finder, we compared this code to the `LZVF` algorithm (Elyiv et al., 2015), finding a good agreement in the detection of voids. In the next future, we will extend this work, applying our algorithm to observed datasets, such as the VIPERS catalogues (Guzzo

and The Vipers Team, 2013). The following step will be to include our Void Finder in a statistical numerical pipeline to be used to extract cosmological constraints from void number counts and clustering, and to study the ellipticity of cosmic voids.

Our Void Finder is currently competing in the new Void Challenge, that is being carried on to prepare the scientific exploration of the Euclid space mission (Laureijs et al., 2011), whose primary goal is to compare different methods to detect cosmic voids.

Sommario

I vuoti cosmici sono ampie regioni sottodense dell'Universo, le cui dimensioni variano dai cosiddetti *minivoids*, il cui diametro è di qualche Mpc, fino ai *supervoids*, con diametri dell'ordine delle centinaia di Mpc. I vuoti separano i filamenti e gli aloni di Materia Oscura tra loro, come previsto da simulazioni numeriche di modelli di Materia Oscura Fredda, confermati ulteriormente dalle osservazioni. I vuoti rappresentano una componente fondamentale della *Rete Cosmica*, occupando circa il 95% del volume totale dell'Universo. Queste strutture demarcano la scala alla quale le fluttuazioni del campo di densità si disaccoppiarono dal flusso di Hubble, andando a costituire regioni sovradense, come ad esempio gli ammassi di galassie (van de Weygaert and Platen, 2011). A causa della loro natura sottodensa, i vuoti rappresentano un importante mezzo per l'indagine di molti aspetti cruciali dell'Universo. Infatti, la loro struttura interna ed altre proprietà statistiche, come ad esempio i conteggi, i profili di densità ed anche la dinamica sono fortemente influenzati dalla presenza dell'Energia Oscura. Ciò implica che queste strutture possano essere considerate come dei laboratori nei quali testare i modelli cosmologici ed, in particolare, essere utili per porre alcuni vincoli sull'Energia Oscura e sulla geometria dell'Universo. Come gli ammassi di galassie, anche i vuoti possono fornire informazioni cruciali riguardanti la struttura su larga scala dell'Universo. Inoltre, il loro ambiente notevolmente sottodenso rappresenta il luogo ideale all'interno del quale le galassie possono evolvere passivamente, senza risentire di alcuna interazione esterna. Ciò consente quindi di poter investigare gli aspetti evolutivi interni delle galassie, in un ambiente in cui le interazioni esterne sono altamente improbabili. Tuttavia, proprio a causa della scarsa densità in questi ambienti, la loro identificazione non è affatto banale. Negli anni, infatti, molti algoritmi sono stati sviluppati per la ricerca dei vuoti cosmici. Alcuni di questi codici, basandosi su criteri di densità o di geometria, sono fortemente soggetti al campionamento delle sorgenti utilizzate per la ricerca dei vuoti. In questo quadro generale, lo scopo principale di questo progetto di tesi è stato quindi l'implementazione di un nuovo codice per la ricerca dei vuoti basato su criteri dinamici, seguendo l'approccio proposto da Elyiv et al. (2015). L'idea

di base consiste nell'impiegare i traccianti come *particelle di prova*, ricostruendo le loro orbite a partire dalla configurazione attuale fino al raggiungimento di una distribuzione omogenea ed isotropa dell'Universo. Questa evoluzione all'indietro nel tempo del campo di spostamento dei traccianti può essere eseguita utilizzando due diversi metodi. Il primo metodo si avvale dell'*approssimazione di Zel'dovich*. Sostanzialmente, la teoria lineare delle perturbazioni di densità è applicabile ad un regime in cui il *contrasto di densità*, $\delta\rho/\bar{\rho}$, è minore di uno. Nella descrizione Lagrangiana di fluido cosmologico, si può tracciare il percorso di un elemento di fluido nello spazio e nel tempo. Data una posizione $\mathbf{q}$ di un elemento di fluido all'istante t_0, la sua posizione agli istanti successivi può essere espressa in termini del campo di spostamento Lagrangiano, $\mathbf{\Psi}$. Questa approssimazione consente, perciò, di estendere la teoria lineare delle perturbazioni di densità poco al di sopra dell'unità. Poiché le orbite percorse dagli oggetti sono lineari, per ricostruire il campo di spostamento Lagrangiano basta connettere le posizioni Euleriane dei traccianti a quelle di una distribuzione casuale.

Il secondo approccio sfrutta invece le proprietà della *funzione di correlazione a due punti*, $\xi(r)$, che rappresenta l'eccesso di probabilità, dP, rispetto a quella attesa in una distribuzione casuale, di trovare una coppia di galassie ad una distanza comovente r, nei rispettivi elementi di volume comoventi, dV_1 e dV_2. Sebbene l'Universo locale è altamente disomogeneo, si ipotizza che, in un'epoca primordiale, l'Universo fosse stato caratterizzato da una distribuzione omogenea. Per questo motivo, un valido metodo per tracciare l'orbita delle galassie indietro nel tempo consiste proprio nel rilassare la distribuzione spaziale attuale fino al raggiungimento dell'omogeneità, quest'ultima caratterizzata da una funzione di correlazione ovunque nulla.

Dal momento che in entrambi gli approcci descritti il cammino percorso da una particella dipende dalla configurazione casuale iniziale, il nostro algoritmo esegue diverse ricostruzioni del campo di spostamento, successivamente mediate tra loro, introducendo un peso Gaussiano. Successivamente, viene calcolato il campo di divergenza, $\mathbf{\Theta} = \nabla\cdot\mathbf{\Psi}$, che rappresenta, per definizione, la densità in ogni punto. Ogni minimo locale identificherà così una regione sottodensa, detta $subvoid$. Attraverso la tecnica *watershed*, le regioni sottodense vicine identificheranno un unico vuoto locale. I centri dei vuoti saranno quindi definiti come i minimi assoluti del campo di divergenza all'interno di ogni vuoto. Per fornire una stima delle dimensioni dei vuoti cosmici identificati, viene calcolato il *raggio effettivo*, ossia il raggio di una sfera avente pari volume del vuoto considerato.

Il nostro metodo dinamico di ricerca dei vuoti cosmici è stato incluso nelle librerie C++/Python sviluppate da Marulli et al. (2016), le CosmoBolognaLib. Per testare la

robustezza del nostro nuovo algoritmo, abbiamo effettuato una comparazione diretta con il metodo LZVF proposto da Elyiv et al. (2015). Da questo confronto, abbiamo avuto un ottimo riscontro riguardante i vuoti identificati da entrambi i metodi. Abbiamo intenzione prossimamente di estendere l'impiego del nostro algoritmo su campioni di dati osservativi, come ad esempio i cataloghi VIPERS (Guzzo and The Vipers Team, 2013). Il passo successivo sarà quello di utilizzare questo algoritmo per estrarre vincoli cosmologici, a partire dai conteggi dei vuoti cosmici a studiarne la loro ellitticità.

Infine, il nostro metodo sta attualmente competendo nell'ambito della nuova Void Challenge, una competizione inerente alla preparazione della missione spaziale Euclid (Laureijs et al., 2011), il cui principale scopo è il confronto tra metodi differenti per identificare i vuoti cosmici.

CHAPTER 1

INTRODUCTION

The ΛCDM Cosmological Model, also called the Standard Cosmological Model, can be directly constructed from the Einstein's Field Equations, assuming the Cosmological Principle, i.e. the conditions of homogeneity and isotropy in the entire Universe, adding the further contribution of the Cosmological Constant, Λ. This theoretical model is constrained by a set of cosmological parameters, describing the energy content, principally due to the Cold Dark Matter and the Dark Energy. There are some still unsolved issues related to the Standard Cosmological Model, such as the intrinsic nature of Dark Matter and Dark Energy. Indeed, although the presence of the *Cosmological Constant*, Λ, provides an accurate description of the current accelerated expansion of the Universe, it does not provide information about the acting trigger mechanism.

The Large Scale Structure of the Universe, can be exploited to put constraints on all the parameters of the cosmological model. For instance, we can perform measurements of the matter perturbations, deviating from the assumption of the Cosmological Principle, by the smallness of the CMB anisotropies ($\delta T/\bar{T} \approx 10^{-5}$), on analysing wide galaxy redshift surveys, in order to describe the lower wavenumbers k of the power spectrum. The study of the the largest and most extreme structures in the mildly non-linear regime allows us to extend our knowledge of the Universe.

The Cosmological Principle is drastically violated at small scales, due to the growth of primordial perturbations in the matter density distribution of the Universe. In the earliest phases of the evolution of the Universe, the radiation and matter components

were coupled via the Thomson scattering. The fluctuations in the temperature spectrum generated anisotropies, and hence the inhomogeneous distribution of the density field. The following structure formation is the result of the gravitational instability acting on those perturbations of matter. The fluctuation distribution can be represented, in a first approximation, as a Gaussian random field. Thanks to the gravitational force, the perturbation amplitudes started to grow, eventually causing collapse. The overdense regions increased their density contrast, δ, while the cosmic depressions in the density field decreased their δ. As a consequence, the increasing of density in some zones produced an even stronger gravitational field. On the contrary, in the regions characterised by $\delta < 0$, the gravitational force became weaker than the mean value. So, the self-gravity reduced its effect, implying that the expansion decelerated less than the rest. In this scenario, the underdensities started to expand faster than the Hubble flow.

The formation and evolution of the cosmic structures generated the so-called *Cosmic Web*, as predicted in the framework of the CDM cosmology (Bond et al., 1998). The result of the gravitational anisotropic collapse is the formation of Dark Matter haloes, filaments, sheets, walls and large areas empty of matter, the so-called *cosmic voids*. Galaxies, following the Dark Matter distribution, were arranged in galaxy clusters, surrounded by a filamentary frame, the latter drawing the void boundaries. As a consequence of their underdensities, the void dynamics is mainly dominated by the Dark Energy. The presence of the Cosmic Web has been confirmed in all large redshift surveys (e.g., Alam et al., 2015; Guzzo and The Vipers Team, 2013; Colless et al., 2003; de Lapparent et al., 1986).

Cosmic voids emerged out of the density depressions of the Universe on the primordial fluctuation field. The presence of cosmic voids in the LSS distribution is one of the most important and earliest prediction of the CDM model (Hausman et al., 1983). Since their discovery (Gregory and Thompson, 1978; Jõeveer et al., 1978), cosmic voids have represented an important brick in the modern cosmological framework. The drastic change in the concept of the large scale structure of the Universe, due to the void discovery, has been carried out thanks to the realisation of several wide-angle and deep galaxy redshift surveys.

Though a widespread and unique definition of cosmic void has not yet been provided, we now have a coherent picture about the main void properties in the ΛCDM cosmological model. In this scenario, voids are underdense regions placed anywhere in the Universe, accounting for the $90-95\%$ of the entire volume (Platen et al., 2007). In a first approximation, we may consider voids as large spherical volumes, spanning a wide range

of scales, from the so-called *minivoids* (few Mpc in radii) (Tikhonov and Karachentsev, 2006), to the giant *supervoids*, with radii of around one hundreds of Mpc, as the Cold Spot in the CMB (Szapudi et al., 2014).

As already mentioned, cosmic voids can play a fundamental role in providing constraints on the Dark Energy (e.g., Granett et al., 2008), and are the ideal sites where to study modified gravity (e.g., Li et al., 2015). Indeed, several investigations can be performed with cosmic voids: through weak gravitational lensing (e.g., Sánchez et al., 2017; Clampitt and Jain, 2015), estimating the Integrated Sachs-Wolfe effect (e.g., Planck Collaboration et al., 2016; Cai et al., 2014), investigating the Dark Matter nature (e.g., Yang et al., 2015), studying the void ellipticity caused by the action of Dark Energy (e.g., Pisani et al., 2015; Sutter et al., 2015a), constraining the Universe geometry through the Alcock-Paczyński test (e.g., Sutter et al., 2014b; Lavaux and Wandelt, 2012), revealing the baryon acoustic oscillations (e.g., Kitaura et al., 2016), testing coupled Dark Energy models (e.g., Pollina et al., 2016), providing void size abundances and stacked density profiles for gravitational theories (e.g., Zivick et al., 2015; Cai et al., 2015), testing evolution models of isolated galaxies, thanks to their pristine environment (e.g., Penny et al., 2015), and much more.

One of the most tricky issues about voids concerns the non-general concordance of their definitions. During the last years, several algorithms able to identify the cosmic voids have been proposed. Lavaux and Wandelt (2010) classified the different Void Finder Algorithms into three broad classes.

The first category is based on a density criterion (e.g., Micheletti et al., 2014; Elyiv et al., 2013; Patiri et al., 2006; Hoyle and Vogeley, 2002; El-Ad et al., 1997). Void Finders belonging to the first class define cosmic voids as volumes with no tracers within, or with a local density value lower than the mean density of the Universe.

The second class refers to the Void Finders that identify voids following a geometrical approach, by using, for instance, polyedra, spheres or tessellations (e.g., Sutter et al., 2015b; Neyrinck, 2008; Platen et al., 2007; Colberg et al., 2005).

Finally, the third class includes the algorithms which detect voids using dynamical criteria. In this case, the tracers (e.g., galaxies) are considered as test particles able to identify "unstable" points in the density field (e.g., Elyiv et al., 2015; Lavaux and Wandelt, 2010; Hahn et al., 2009).

The first two categories of Void Finder algorithms detect cosmic voids using the Eulerian positions of the tracers. These approaches, however, are subject to various problems. When using mass tracers for the reconstruction of the density distribution, a

bias prescription has to be taken into account. The importance of the bias modelling has been discussed in Pollina et al. (2016), in particular to discriminate between different cosmological models. Another drawback is due to the definition of voids as underdensities. Indeed, Eulerian-position algorithms are strongly prone to the shot-noise error. On the contrary, the algorithms of the third-class, which rely on the Lagrangian positions, suffer less the shot-noise problem.

The main goal of this thesis work is the development of a new Void Finder algorithm based on a dynamical criterion, able to identify the depressions in the density field. This algorithm is composed by three main steps. The first step deals with the reconstruction of the displacement field of the tracers, the latter used as test particles, in a back-in-time evolution. This reconstruction can be performed by two different methods, `LaZeVo`, exploiting the Zel'dovich approximation, and `RIVA`, which relies on the measurement of the two-point correlation function. Once the displacement field has been reconstructed, the second step computes the divergence of the velocity field, which represents, by definition, the density field. Since voids are defined as regions of negative velocity divergence, the second step looks for the density local minima, as cosmic voids candidates. By performing a filling of the depressions in the density field, through the *watershed* technique, the third steps identifies the cosmic voids.

This new Void Finder is now part of the CBL project (Marulli et al., 2016), a set of C++/Python libraries for cosmological calculations.

We propose an application of our Void Finder to a DM halo catalogue, making also a direct comparison with an already existing algorithm, i.e. the `LZVF` method proposed by Elyiv et al. (2015).

Then, we discuss the first results obtained in the context of the new Void Challenge, proposed inside the Euclid space mission collaboration, whose aim consists in a comparison between different methods for the identification of cosmic voids.

This thesis work is organised as follows:

- Chapter 2 deals with an overview of the cosmological framework, introducing the theoretical basis of the Standard Cosmological Model;
- Chapter 3 illustrates the role of the cosmic voids in the Universe, reviewing some studies concerning their structure, formation, evolution and dynamics;
- Chapter 4 provides a general overview about the Void Finders, subdivided according to the criterion used to detect cosmic voids;

- Chapter 5 accurately describes the internal structure of our new Void Finder, explaining the methods used to reconstruct the displacement field and its divergence and the identification of voids;
- Chapter 6 deals with the main results obtained by applying our new Void Finder to a DM halo catalogue, comparing them to those of the LZVF algorithm; moreover, we present a first application of our method in the context of the new Euclid Void Challenge;
- Chapter 7 summarises the results of this project, focusing on the possible future perspectives.

CHAPTER 2

A Cosmological Background

In this chapter we summarise briefly the cosmological framework on which this thesis work is based. We provide the main equations which are the basis of the theoretical models, describing the growing and the dynamical evolution of the Universe. In section 2.1 we start by introducing some notions about General Relativity and in particular the Einstein's Field Equations. In section 2.2 we define the Friedmann–Lemaître–Robertson–Walker metric, that describes the curvature of the spatial hypersurfaces of the Universe. In section 2.3 we introduce the Hubble Law and the definition of Redshift. In section 2.4 we illustrate the Friedmann Equations, as the solutions to the Einstein's Field Equations and we make a comparison between the three possible geometrical models. In section 2.5 we illustrate the main features of the Standard Cosmological Model. The section 2.6 deals with the Jeans theory about the model gravitational instability and we discuss the growth of the primordial fluctuations in the linear regime and beyond.

2.1 Fundamentals of General Relativity

Gravity is expected to be the main force acting throughout the Universe on large scales. The best description of this force is given by the Theory of General Relativity (GR) proposed by Albert Einstein in 1915 (Einstein, 1915).

In this context, the geometry of space-time is described by the *metric tensor*, $g_{\mu\nu}$. The invariant *interval* between two different events in space-time, (t, x_1, x_2, x_3) and

$(t', x_1', x_2', x_3') = (t + \delta t, x_1 + \delta x_1, x_2 + \delta x_2, x_3 + \delta x_3)$ is defined by

$$\mathrm{d}s^2 = g_{\mu\nu}\,\mathrm{d}x^\mu\,\mathrm{d}x^\nu. \tag{2.1}$$

This interval can be explicitly separated out as

$$\mathrm{d}s^2 = g_{00}\,\mathrm{d}t^2 + 2g_{0i}\,\mathrm{d}x^i\,\mathrm{d}t + g_{ij}\,\mathrm{d}x^i\,\mathrm{d}x^j, \tag{2.2}$$

where $g_{00}\,\mathrm{d}t^2$ is the time component, $g_{ij}\,\mathrm{d}x^i\,\mathrm{d}x^j$ the spatial components and $2g_{0i}\,\mathrm{d}x^i\,\mathrm{d}t$ the mixed components. By defining the *Riemann tensor* as follows

$$R^\mu_{\alpha\beta\gamma} \equiv \frac{\mathrm{d}\Gamma^\mu_{\alpha\gamma}}{\mathrm{d}x^\beta} - \frac{\mathrm{d}\Gamma^\mu_{\alpha\beta}}{\mathrm{d}x^\gamma} + \Gamma^\mu_{\sigma\beta}\Gamma^\sigma_{\gamma\alpha} - \Gamma^\mu_{\sigma\gamma}\Gamma^\sigma_{\beta\alpha}, \tag{2.3}$$

in which $\Gamma^\cdot_{\cdot\cdot}$ are the terms of the *affine connection*, $R^\mu_{\alpha\beta\gamma}$ is a fourth-order tensor contractible to the *Ricci tensor*, $R^{\mu\nu}$, or further to the *curvature scalar*, R:

$$R_{\alpha\beta} \equiv R^\mu_{\alpha\beta\mu}, \qquad R \equiv R^\mu_\mu = g^{\mu\nu}R_{\mu\nu}. \tag{2.4}$$

We introduce the *energy-momentum tensor*, $T_{\mu\nu}$, which describes the content of energy and matter in the Universe. We can connect $T_{\mu\nu}$ with the space-time metric by using the *Einstein's Field Equations*:

$$R_{\mu\nu} - \frac{1}{2}g_{\mu\nu}R = \frac{8\pi G}{c^4}T_{\mu\nu}, \tag{2.5}$$

where G and c are the gravitational constant and the speed of light, respectively. Looking at the left-hand side of the equation (2.5), we can define the *Einstein tensor* $G_{\mu\nu}$ as

$$G_{\mu\nu} \equiv R_{\mu\nu} - \frac{1}{2}g_{\mu\nu}R. \tag{2.6}$$

This tensor has zero covariant divergence, according to what we want to obtain for $T_{\mu\nu}$ by virtue of the conservation laws. Combining the equations (2.5) and (2.6), we obtain the final formula of the *Einstein's gravitational field equations*:

$$G_{\mu\nu} = \frac{8\pi G}{c^4}T_{\mu\nu}. \tag{2.7}$$

We will consider a set of homogeneous and isotropic models. First of all, if the mean free path of particles constituting a fluid, λ_{mfp}, is lower than the physical scales of interaction, we may consider this fluid as perfect. The different energy components in a Big-Bang model description constitute the so-called *perfect fluid*. Considering this perfect fluid in its rest-frame, the related *energy-momentum tensor* $T_{\mu\nu}$ can be written as follows:

$$T_{\mu\nu} = -pg_{\mu\nu} + (p + \rho c^2)u_\mu u_\nu, \tag{2.8}$$

where p is the *pressure* term, ρc^2 is the *energy density* term and $u_\cdot$ are the components of the *4-velocity* of the fluid element.

2.2 THE FRIEDMANN–LEMAÎTRE–ROBERTSON–WALKER METRIC

In order to describe the Large Scale Structure (LSS), we can assume the *Cosmological Principle* (CP) that asserts that there are no observable inhomogeneities at large scales. Hence, the Universe appears to be *homogeneous* and *isotropic*. Homogeneity implies that all observers, in different places all around the Universe, observe the same properties, while isotropy involves that there are not favourite directions. Having established the concept of the CP, our goal is to see if it is possible to construct some models of the Universe in which this principle is satisfied. Hence, the task is to find solutions to the Einstein's Field Equations.

Assuming homogeneity and isotropy, we can define a *universal time* such that the spatial metric is the same in each point at all times. The isotropy, for which there are no preferential directions in the Universe, implies that the mixed components, g_{0i}, of the equation (2.2) have to be null. Thus we can obtain the following form of the metric:

$$\mathrm{d}s^2 = c^2\mathrm{d}t^2 - g_{ij}\,\mathrm{d}x^i\,\mathrm{d}x^j = c^2\mathrm{d}t^2 - \mathrm{d}l^2. \tag{2.9}$$

As already expressed in the previous section, we can regard the Universe as a continuous fluid in which each element is marked with a set of three spatial coordinates x^i (with $i = 1, 2, 3$). Furthermore, we define a *proper time*, that is measured by a clock moving with the perfect fluid.

The geometrical properties of the space-time are described by a metric. By using the time coordinate (the first term on the right-hand side of the equation (2.9)) and assuming the spatial isotropy, we can derive the most general form of the equation (2.9) that verifies the CP as follows:

$$\mathrm{d}s^2 = c^2\mathrm{d}t^2 - a^2(t)\left[\frac{\mathrm{d}r^2}{1-\kappa r^2} + r^2(\sin^2\theta\,\mathrm{d}\varphi^2 + \mathrm{d}\theta^2)\right]. \tag{2.10}$$

The formula (2.10) defines the *Friedmann–Lemaître–Robertson–Walker* (FLRW) *metric* expressed in spherical polar coordinates, where r, θ and φ are the dimensionless comoving coordinates and t is the proper time. In this metric also two new terms appear: $a(t)$ is the *cosmic scale factor* (or the *expansion parameter*), having the dimensions of a length, and κ is the *curvature parameter*. The value of κ and the function $a(t)$ can be derived by the Einstein's Field Equations, for any given energy-momentum tensor.

Let us consider a free massive particle at rest located at the origin of the comoving system at an instant in time. The absence of preferred directions ensures that no velocity variation can be induced on this particle by gravity. Thanks to the required homogeneity, the world lines $x^i = const$ are the so-called *geodesics*.

2.2.1 THE SPATIAL CURVATURE

The curvature of the spatial hypersurfaces of the Universe can be positive, zero or negative. Indeed, the curvature of the space-time depends on the value of the parameter κ, which can be scaled in such a way that the only three possible values are +1, 0 or -1.

To figure out what the scale factor $a(t)$ really is, we can calculate the proper distance at time t from the origin to a comoving particle at radial coordinate r. It is convenient to introduce a coordinate χ defined as

$$\chi \equiv \int \frac{\mathrm{d}r}{\sqrt{1-\kappa r^2}}. \tag{2.11}$$

By introducing the three possible values of κ in the equation (2.11), we obtain

$$\chi = \begin{cases} \sin^{-1} r & \text{for } \kappa = +1 \\ r & \text{for } \kappa = 0 \\ \sinh^{-1} r & \text{for } \kappa = -1 \end{cases} \tag{2.12}$$

or rewriting in terms of (χ, θ, φ), the FLRW becomes

$$\mathrm{d}l^2 = a^2[\mathrm{d}\chi^2 + f^2(\chi)(\mathrm{d}\theta^2 + \sin^2\theta\,\mathrm{d}\varphi^2)], \tag{2.13}$$

with

$$f(\chi) = \begin{cases} \sin\chi & \text{for } \kappa = +1 \\ \chi & \text{for } \kappa = 0 \\ \sinh\chi & \text{for } \kappa = -1 \end{cases}. \tag{2.14}$$

The three values of the curvature parameter lead to three different geometries of the Universe. If $\kappa = 0$, the space has an infinite curvature. This is the *flat Universe* case, where the geometry is Euclidean. For $\kappa = +1$, the properties of the hypersphere are more complex. This is the *closed Universe* case. The space has a finite volume, but has no boundaries, analogous to the two-dimensional case of a sphere. In this case, the equation (2.13) describes a 3D-sphere with radius a in a four-dimensional flat space. Such a sphere is defined by

$$x_1^2 + x_2^2 + x_3^2 + x_4^2 = a^2. \tag{2.15}$$

Introducing the angular coordinates (χ, θ, ϕ) we obtain:

$$\begin{aligned} x_1 &= a\cos\chi\sin\theta\sin\phi, \\ x_2 &= a\cos\chi\sin\theta\cos\phi, \\ x_3 &= a\cos\chi\cos\theta, \\ x_4 &= a\sin\chi. \end{aligned} \tag{2.16}$$

By expressing $\mathrm{d}x_i$ in terms of polar coordinates in the line element

$$\mathrm{d}L^2 = \mathrm{d}x_1^2 + \mathrm{d}x_2^2 + \mathrm{d}x_3^2 + \mathrm{d}x_4^2, \tag{2.17}$$

the metric takes the same form of the relation (2.13), for $\kappa = +1$:

$$\mathrm{d}L^2_{sphere} = a^2[\mathrm{d}\chi^2 + \sin^2\chi(\mathrm{d}\theta^2 + \sin^2\theta\,\mathrm{d}\phi^2)]. \tag{2.18}$$

The space of the closed Universe is totally covered by the following range of angles

$$\begin{aligned} 0 \le \chi < \pi, \\ 0 \le \theta < \pi, \\ 0 \le \phi < 2\pi, \end{aligned} \tag{2.19}$$

and the maximum volume is

$$V_{max} = \int_0^{2\pi}\mathrm{d}\phi\int_0^{\pi}\mathrm{d}\theta\int_0^{\pi}\mathrm{d}\chi = a^3\int_0^{2\pi}\mathrm{d}\phi\int_0^{\pi}\sin\theta\,\mathrm{d}\theta\int_0^{\pi}\sin^2\chi\,\mathrm{d}\chi = 2\pi^2a^3. \tag{2.20}$$

The surface of a 2D-sphere (with $\chi = const$) is

$$S = 4\pi a^2\sin^2\chi. \tag{2.21}$$

This surface has the maximum value for $\chi = \pi/2$ and it is null for $\chi = 0, \pi$. In such a space the surface S is larger than in flat geometry and the sum of internal angles of a triangle is greater than π.

The third case, for $\kappa = -1$, is characterized by a hyperbolic geometry. A 3D-hyperboloid is described by the following relation:

$$-x_1^2 - x_2^2 - x_3^2 + x_4^2 = a^2. \tag{2.22}$$

Analogously to the spherical case described above, the line element is

$$\mathrm{d}L^2 = \mathrm{d}x_1^2 + \mathrm{d}x_2^2 + \mathrm{d}x_3^2 - \mathrm{d}x_4^2. \tag{2.23}$$

We can also define a set of angular coordinates with

$$\begin{aligned} x_1 &= a \sinh\chi \sin\theta \sin\phi, \\ x_2 &= a \sinh\chi \sin\theta \cos\phi, \\ x_3 &= a \sinh\chi \cos\theta, \\ x_4 &= a \cosh\chi, \end{aligned} \tag{2.24}$$

so that the line element becomes

$$\mathrm{d}L^2_{hyperboloid} = a^2[\mathrm{d}\chi^2 + \sinh^2\chi(\mathrm{d}\theta^2 + \sin^2\theta\,\mathrm{d}\phi^2)]. \tag{2.25}$$

The properties of a geometrical space having a constant negative curvature are similar to those of a flat case. In fact, it represents an infinite *open Universe*. The range of coordinates are the following:

$$\begin{aligned} 0 \le \chi < \infty, \\ 0 \le \theta < \pi, \\ 0 \le \phi < 2\pi, \end{aligned} \tag{2.26}$$

and the surface, S, is defined by

$$S = 4\pi a^2 \sinh^2\chi. \tag{2.27}$$

In this particular case, the sum of the internal angles of a triangle is lower than π and the surface is greater than the Euclidean one.

2.3 THE HUBBLE LAW

Let us consider a point P at a distance d_P from another point P_0. The *proper distance*, d_P, is defined as the distance measured by observers which connect P to P_0 at a given time t. From the FLRW metric (eq. (2.10)), for $\mathrm{d}t = 0$, we have

$$d_P = \int_0^r \frac{a(t)\,\mathrm{d}r'}{\sqrt{1-\kappa r^2}} = a(t) f(r). \tag{2.28}$$

It can be observed that the nonstatic nature of the FLRW metric is due to the time dependence of $a(t)$. At time t, the proper distance is related to the present one (t_0) by the following relation:

$$d_C = d_P(t_0) = a_0 f(r), \tag{2.29}$$

where $a_0 \equiv a(t = t_0)$. The previous quantity is called the *radial comoving distance* because it remains the same as the Universe expands. The direct link between the two definitions is the following:

$$d_P = \frac{a(t)}{a_0} d_C. \tag{2.30}$$

We can observe from eq. (2.30) that the proper and comoving distances are equal at the present time, t_0.

The expansion parameter, $a(t)$, varies over time, and the proper distance, d_P, varies as well. This implies the existence of a *radial velocity*, v_r, as derivative of d_P with respect to t:

$$v_r = \frac{\mathrm{d}d_P}{\mathrm{d}t} = \frac{\mathrm{d}}{\mathrm{d}t}[a(t) f(r)] = \dot{a}(t) f(r) + a(t) \dot{f}(r). \tag{2.31}$$

Because of the time-independence of the $f(r)$ term, the relation (2.31) becomes

$$v_r = \dot{a}(t) f(r) = \frac{\dot{a}(t)}{a(t)} d_P. \tag{2.32}$$

The equation (2.32) is the so-called *Hubble Law* and the relative quantity

$$H(t) \equiv \frac{\dot{a}(t)}{a(t)} \tag{2.33}$$

is the *Hubble parameter*. Combining eqs. (2.31) and (2.32), we obtain the direct link between the radial velocity and the proper distance, as follows:

$$v_r = H(t) d_P. \tag{2.34}$$

The Hubble parameter provides information on the isotropic expansion velocity. This parameter is usually called the *Hubble constant*, erroneously. Though $H(t)$ is actually a function of time, it has the same value across the Universe at a given cosmic time. The most recent estimate of the Hubble constant at the present time, $H(t_0) \equiv H_0$, is provided by the SDSS-III Baryon Oscillation Spectroscopic Survey (BOSS) (Grieb et al., 2016), is

$$H_0 = 67.6^{+0.7}_{-0.6}\,\mathrm{km\,s^{-1}\,Mpc^{-1}}. \tag{2.35}$$

It is conventional to introduce a dimensionless parameter, h, redefining the Hubble parameter as

$$H_0 = 100\,h\,\mathrm{km\,s^{-1}\,Mpc^{-1}}. \tag{2.36}$$

The motion of objects due solely to the expansion of the Universe is called the *Hubble flow*. We can see that H_0 is expressed in units of s^{-1}: the inverse of the Hubble parameter may provide a rough estimate of the age of the Universe (approximately 14 Gyr).

2.3.1 THE REDSHIFT

The *redshift* is defined as the relative difference between the observed, λ_{oss}, and emitted, λ_{em}, wavelengths

$$z \equiv \frac{\lambda_{oss} - \lambda_{em}}{\lambda_{em}}, \tag{2.37}$$

or analogously for frequencies, by means of the relation $\lambda = c/\nu$. From eq. (2.37), we can see that z is a positive quantity when the electromagnetic radiation from an object is increased in wavelength, and so shifted to the red region of the spectrum.

Consider a source emitting a photon with wavelength λ_{em} at time t_{em}. An observer located at a distance d will receive the signal with wavelength λ_{oss} at t_{oss}. Photons move along null geodesics during the expansion of the Universe. Hence, the term $\mathrm{d}s^2$ is equal to zero. From the last assumption and the FLRW metric, one has the following relation:

$$c^2\mathrm{d}t^2 - a^2(t)\left(\frac{\mathrm{d}r^2}{\sqrt{1-\kappa r^2}} + r^2(\mathrm{d}\theta^2 + \sin^2\theta\,\mathrm{d}\varphi^2)\right) = 0. \tag{2.38}$$

Let us assume θ and φ constants for simplicity such that, integrating the metric along the path, eq. (2.38) becomes

$$\int_{t_{em}}^{t_{oss}} \frac{c\,\mathrm{d}t}{a(t)} = \int_0^r \frac{\mathrm{d}r'^2}{\sqrt{1-\kappa r'^2}} = f(r). \tag{2.39}$$

Now let us suppose that a second photon is emitted with a time delay, δt_{em}, with respect to the first one and reaches the observer at $t'_{oss} = t_{oss} + \delta t_{oss}$. Since for the two photons the path is the same ($f(r)$ does not change because of the assumption of comoving coordinates) and the difference is just in time, we can express eq. (2.39) as

$$\int_{t_{em}}^{t_{oss}} \frac{c\,\mathrm{d}t}{a(t)} = f(r). \tag{2.40}$$

If the time intervals are small ($\delta t \to 0$), we can consider $a(t)$ almost constant and therefore

$$\frac{\delta t_{oss}}{a(t_{oss})} = \frac{\delta t_{em}}{a(t_{em})}. \tag{2.41}$$

Since $\delta t = 1/\nu$ and $\lambda = c/\nu$, we obtain

$$1 + z = \frac{a_{oss}}{a_{em}}, \tag{2.42}$$

or, more generally, for an observer located at present time and a generic instant t, we have

$$1 + z = \frac{a_0}{a(t)}. \tag{2.43}$$

The redshift is usually used to measure distances of extragalactic sources.

2.4 THE FRIEDMANN EQUATIONS

GR describes the relation between the geometry of space-time, represented by the metric tensor $g_{\mu\nu}(x_i)$, and the energy content of the Universe, expressed by the energy-momentum tensor $T_{\mu\nu}(x_i)$. Without any futher assumption on the geometry of the Universe, we can apply the FLRW metric (eq. (2.10)) to the Einstein Equations (eq. (2.5)). Among the 16 equations of the system, just two are independent. The two solutions, assuming the CP and Perfect Fluid, provide the time evolution of $a(t)$ describing the growth of the Universe. They are called the *First* and the *Second Friedmann Equations* and can be expressed as follows:

$$\ddot{a} = -\frac{4\pi}{3} G \left(\rho + \frac{3p}{c^2} \right) a, \tag{2.44}$$

$$\dot{a}^2 + \kappa c^2 = \frac{8\pi}{3} G \rho a^2. \tag{2.45}$$

Assuming the Universe as a closed system, unable to lose energy, the two equations above can be linked to each other by the *adiabatic condition*

$$\mathrm{d}\mathscr{U} = -p\mathrm{d}V, \tag{2.46}$$

where $\mathscr{U}$ is the *internal energy* of the Universe. Equation (2.46) can also be expressed as follows:

$$\mathrm{d}(\rho c^2 a^3) = -p\mathrm{d}a^3, \tag{2.47a}$$

$$\dot{p}a^3 = \frac{\mathrm{d}}{\mathrm{d}t}(a^3(\rho c^2 + p)), \tag{2.47b}$$

$$\dot{\rho} + 3\left(\rho + \frac{p}{c^2}\right)\frac{\dot{a}}{a} = 0. \tag{2.47c}$$

Each constituent of the Universe has its own equation of state, but all of them contribute to the density term ρ.

2.4.1 THE FRIEDMANN MODELS AND THE COSMOLOGICAL CONSTANT

In 1922, the mathematician Alexander Friedmann provided the two solutions of the Einstein Equations, implementing a set of cosmological models. At that time, the Universe

was assumed to be static, and hence $\ddot{a} = \dot{a} = 0$. However, as we can see from equation (2.44), the Universe can be static if and only if

$$\rho = -3\frac{p}{c^2}. \tag{2.48}$$

In other words, either the pressure or the energy density must be negative. A fluid with these characteristics does not seem to be physically acceptable. Since also Einstein was convinced that the Universe was static, he added a new term to the eq. (2.5), modifying the equation as follows:

$$R_{\mu\nu} - \frac{1}{2}g_{\mu\nu}R - \Lambda g_{\mu\nu} = \frac{8\pi G}{c^4}T_{\mu\nu}. \tag{2.49}$$

Λ is the so-called *Cosmological Constant*. As we shall see, an *ad hoc* choice of Λ can imply a static model. Equation (2.49) is the most general possible modification of the original Einstein Equations, enough to satisfy the condition that $T_{\mu\nu}$ is equal to a tensor constructed only from the metric $g_{\mu\nu}$ and its first and second derivatives.

We can write eq. (2.49) by modifying the energy-momentum tensor, so as to obtain a similar form to the original one

$$R_{\mu\nu} - \frac{1}{2}g_{\mu\nu}R = \frac{8\pi G}{c^4}\widetilde{T}_{\mu\nu}, \tag{2.50}$$

where the new tensor is formally given by

$$\widetilde{T}_{\mu\nu} \equiv T_{\mu\nu} + \frac{\Lambda c^4}{8\pi G}g_{\mu\nu}, \tag{2.51}$$

or equivalently

$$\widetilde{T}_{\mu\nu} \equiv -\widetilde{p}g_{\mu\nu} + (\widetilde{p} + \widetilde{\rho}c^2)u_\mu u_\nu \tag{2.52}$$

with the *effective pressure* and *density*

$$\widetilde{p} \equiv p - \frac{\Lambda c^4}{8\pi G}, \qquad \widetilde{\rho} \equiv \rho + \frac{\Lambda c^2}{8\pi G}. \tag{2.53}$$

When Hubble finally discovered the expansion of the Universe (Hubble, 1929), Einstein regretted the introduction of Λ. Neverthless, Λ-models have been reintroduced recently to describe the accelerated expansion of the Universe, firstly observed from Supernovae (SNe) (Perlmutter et al., 1999; Schmidt et al., 1998; Riess et al., 1998). The Cosmological Constant has the effect similar to repulsive force that contrasts with the gravitational pull.

Nowadays, scientists have not yet figured out what Λ really is. The origin of this "push" shall be assigned to the *Dark Energy*.

We can specify the *Equation of State* (EoS) for the fluid in the form $p = p(\rho)$. In particular, by introducing the w parameter and assuming no variations in time of the entropy S (*adiabatic condition*) , the EoS becomes

$$p = w\rho c^2. \tag{2.54}$$

The w parameter lies in the so-called *Zel'dovich interval*:

$$0 \leq w < 1. \tag{2.55}$$

In the following, we will consider just perfect fluids described by EoS satisfying the condition given by eq. (2.55) and also assuming $w = -1$ in the case of a Λ-Universe.

The fluid can be in two different states: *non-relativistic* and *relativistic*. The first case is represented by *dust*, having $w = 0$, i.e. with null pressure. While a non-degenerate and ultra-relativistic fluid has an EoS with $w = 1/3$. This is the case for a *radiative fluid* or, more generally, for photons and relativistic particles like neutrinos.

The w parameter is directly related to the adiabatic sound speed of a fluid:

$$c_s = \sqrt{\frac{\partial p}{\partial \rho}}\bigg|_S. \tag{2.56}$$

We can note that w can not go beyond 1, because it would imply a speed of sound greater than c. A peculiar case, out of the range given by eq. (2.55), is $w = -1$, that describes a perfect fluid with effects equivalent to the ones of the cosmological constant.

By replacing the p term in the left-hand side of the adiabatic condition (eq. (2.47a)) with the right-hand side of the EoS (eq. (2.54)), one can derive how the density evolves in time:

$$\rho = \rho_0 \left(\frac{a}{a_0}\right)^{-3(1+w)} = \rho_0 (1+z)^{3(1+w)}. \tag{2.57}$$

The density evolution depends on the value of w. This can be used to determine which component dominates over the others at a given redshift.

The Second Friedmann Equation can provide us information about the curvature. Indeed, we can rewrite the equation as follows

$$\left(\frac{\dot{a}}{a}\right)^2 \left(\frac{\rho}{\rho_c} - 1\right) = \frac{\kappa c^2}{a^2}, \tag{2.58}$$

where ρ_c is the *critical density*, for which the spatial geometry of the Universe is flat:

$$\rho_c(t) \equiv \frac{3H^2(t)}{8\pi G}. \tag{2.59}$$

The expansion of the Universe will go on indefinitely if $\rho < \rho_c$, while it will be halted and then followed by a contraction if $\rho > \rho_c$. We can define the dimensionless *density parameter* as

$$\Omega(t) \equiv \rho(t)\rho_c(t). \tag{2.60}$$

As well as the energy density term represents one or more of the components, the Ω parameter can be composed of one or more contributions. It is greater than, equal to or less than unity if the Universe is *closed* ($\kappa = +1$), *flat* ($\kappa = 0$) or *open* ($\kappa = -1$), respectively. By assuming a cosmological model with a single dominant component, one can re-express eq. (2.57) in terms of the density parameter as follows:

$$\Omega_w^{-1}(z) - 1 = \frac{\Omega_0^{-1} - 1}{(1+z)^{1+3w}}, \tag{2.61}$$

where the dependence on the kind of component (e.g., dust, radiation, Λ) is made explicit. Moreover, it is useful to express the Second Friedmann Equation in term of Ω, H and z. By combining this equation with the definition of the density parameter, the Hubble Law and the eq. (2.43), we obtain

$$H^2(z) = H_0^2(1+z)^2\left(1 - \sum_i \Omega_{0,w_i} + \sum_i \Omega_{0,w_i}(1+z)^{1+3w_i}\right), \tag{2.62}$$

in which $H(z)$ is the Hubble parameter at a generic redshift and $\sum_i \Omega_{0,w_i}$ is the total sum of all i-th components with corresponding w_i value. The difference $1 - \sum_i \Omega_{0,w_i}$ values is related to the curvature of the Universe.

2.4.1.1 The Big Bang Singularity

All possible models of the Universe, assuming it is composed of fluids with $-\frac{1}{3} < w < 1$, have necessarily an instant in which a vanishes and the density value diverges. This instant is called the *Big Bang*. From the First Friedmann Equation, we note that $\ddot{a} < 0$ for each t, and this provides that $(\rho + 3p/c^2) > 0$, or (by using the EoS) $(1+3w) > 0$. This implies the existence of an instant at which $a(t)$ is equal to zero, at some finite time in the past. The following growth of the Universe is not due to some kind of pressure, but rather it is intrinsically determined by the conditions of homogeneity and isotropy laid down by the Cosmological Principle.

2.4.2 FLAT, OPEN AND CLOSED MODELS

We can find the solutions of equation (2.62) for a generic flat Universe in which $\sum_i \Omega_w = 1$. It is useful to start considering some special cases of the Universe composed of by just one component, e.g. dust or radiation. In this case, the generic solution for a perfect fluid, assuming a flat geometry, is called *Einstein-de Sitter Model* (EdS) and eq. (2.62) becomes

$$H(z) = H_0(1+z)^{\frac{3(1+w)}{2}}. \tag{2.63}$$

Table 2.1 provides a list of some useful equations in the EdS Universe both for a generic fluid and for *matter-dominated* and *radiation-dominated* models.

TABLE 2.1 - Some useful relations in the EdS Universe: generic component (left column), matter-dominated Universe (central column) and radiation-dominated Universe (right column).

Generic fluid	*Dust* - $w = 0$	*Radiation* - $w = 1/3$
$a(t) = a_0\left(\frac{t}{t_0}\right)^{\frac{2}{3(1+w)}}$	$a(t) = a_0\left(\frac{t}{t_0}\right)^{\frac{2}{3}}$	$a(t) = a_0\left(\frac{t}{t_0}\right)^{\frac{1}{2}}$
$t = t_0(1+z)^{-\frac{3(1+w)}{2}}$	$t = t_0(1+z)^{-\frac{3}{2}}$	$t = t_0(1+z)^{-2}$
$H(t) = \frac{2}{3(1+w)}\frac{1}{t}$	$H(t) = \frac{2}{3t}$	$H(t) = \frac{1}{2t}$
$t_0 = \frac{2}{3(1+w)}\frac{1}{H_0}$	$t_0 = \frac{2}{3H_0}$	$t_0 = \frac{1}{2H_0}$
$\rho = \frac{1}{6\pi G(1+w)^2}\frac{1}{t}$	$\rho = \frac{1}{6\pi G t^2}$	$\rho = \frac{3}{32\pi G t^2}$

Let us now briefly examine the *curved* cases, considering model with only a single component characterized by $\Omega_w \neq 1$. For small values of a or, equivalently, at high redshifts we have

$$\Omega_0\left(\frac{a_0}{a}\right)^{1+3w} \gg (1-\Omega_0). \tag{2.64}$$

If we introduce a critical value z^* (or a^*) so that

$$\Omega_0\left(\frac{a_0}{a^*}\right)^{1+3w} = \Omega_0(1+z^*)^{1+3w} = |1-\Omega_0|, \tag{2.65}$$

when $z \gg z^*$ (or $a \ll a^*$), the relation (2.62) is reduced to

$$H(z) = H_0\Omega_0^{1/2}(1+z)^{\frac{3(1+w)}{2}}. \tag{2.66}$$

Equation (2.66) is similar to what we found for an EdS Universe (eq. (2.63)), with the only difference that Ω_0 is not equal to one. Therefore it can be concluded that for high

redshift values, the curved models have the same behaviour of the EdS one. So, it is impossible to assess the curvature of the Universe, if we consider t too close to the Big Bang.

On the other hand, for $z \ll z^*$ (or $a \gg a^*$) for an *open Universe* ($\kappa = -1$) the expansion parameter grows indefinitely with time. While a *closed Universe* is characterized by the existence of an instant t_m at which $\dot{a}$ is zero and, after this time, the expansion parameter decreases. It implies that there is a second singularity (symmetrical in time with respect to the Big Bang) usually called *Big Crunch*. Figure 2.1 below shows four possible scenarios (open, flat, closed and ΛCDM models) for the evolution of the expansion parameter a as a function of time.

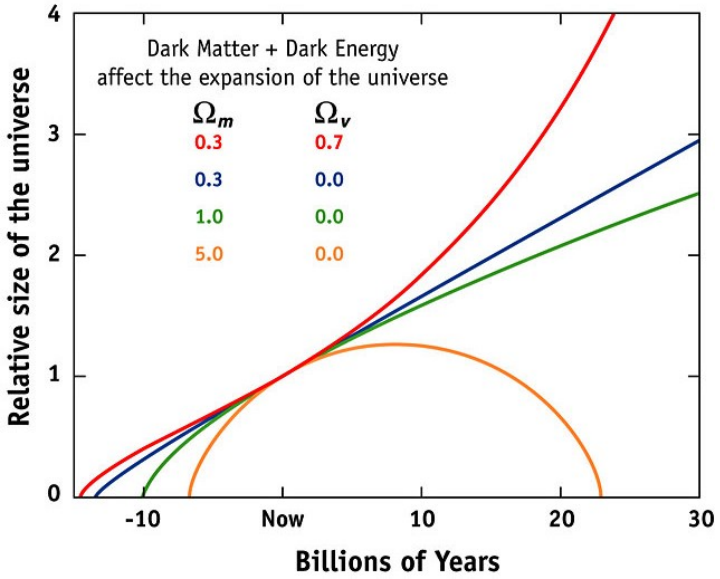

FIGURE 2.1 - Evolution of the expansion parameter a as a function of time for four possible scenarios. The orange curve represents a closed Universe ($\Omega_m = 5 > 1$), which initially expands, then turns around and collapses under its own weight (Big Crunch). The green curve describes a flat model ($\Omega_m = 1$) , in which the expansion rate continually slows down. The blue curve represents an open Universe ($\Omega_m = 0.3 < 1$) with a lower density than the previous two models. The red curve shows a Universe having a large amount of Dark Energy ($\Omega_\Lambda = 0.7$), which causes an accelerated expansion of the Universe.
Credit: https://map.gsfc.nasa.gov/universe/WMAP_Universe.pdf.

2.5 THE ΛCDM UNIVERSE

By the beginning of the 21st century, the ΛCDM Cosmological Model, or simply the Standard Cosmological Model, was generally accepted. The ΛCDM predicts the presence of the Cosmic Microwave Background (CMB), which is the radiation left over from the recombination after Big Bang, but also describes very well the LSS of the Universe (such as clusters, galaxies).

According to this model, the Universe is composed principally by a radiative fluid with a negligible density, approximately 4% Baryonic Matter, about 26% Cold Dark Matter and for the remaining 70% an unknown form of Dark Energy (in the form of Λ), the latter responsible of the accelerated expansion of the Universe (for more details on the estimates of these values, see Planck Collaboration et al. 2016). The *radiative fluid* consists of relativistic particles and photons. This component does not play a fundamental role at $z = 0$, since its density parameter is $\Omega_{0,r} \approx 10^{-5}$, as can be estimated from the CMB temperature measurement.

Regarding the matter component, the model assumes that the Universe is composed of both already mentioned *baryonic* and *non-baryonic matter*, also called *ordinary matter* and *Dark Matter*, respectively. The difference between the two matter components concerns their interactions. Though both of them are able to interact via gravity, just the ordinary matter can interact with photons. Fritz Zwicky in 1937 was the first scientist who proposed the existence of another kind of matter to explain the dynamics of galaxies in the Coma cluster (Zwicky, 1937). By measuring the velocity dispersion of the galaxies inside the cluster, Zwicky estimated the average virial mass of the system be larger than $4.5 \times 10^{10} M_{\odot}$. However, the mass related to the luminosity of these "nebulae" was far smaller. Zwicky calculated a mass-to-light ratio of about 500, much larger than the ratio of about 3 measured for the local Kapteyn stellar system. Since the Zwicky's discoveries and later works, from the 1970s many studies have been done in order to understand the nature of DM. For instance, Vera Rubin and Kent Ford measured the rotation curves of M31, noticing a difference between the expected angular motion and the observed one (Rubin and Ford, 1970). A large list of DM particle candidates have been suggested so far. It is thought that DM could be constituted by what are called *weakly interacting massive particles* (WIMPs), that is particles able to interact only through gravity and weak force (Jungman et al., 1996). Other studies investigated new theories of modified gravity to describe the observations without having to assume any form of non-baryonic matter (for a review, see Clifton et al. 2012).

Maddox et al. 1990, Efstathiou et al. 1990 and Geller and Huchra 1989 suggested that the CDM model was not able to explain the observed distribution of cosmological structures on very large scales. So they argued that the Universe is now lead by the Cosmological Constant.

Nowadays, the ΛCDM model is broadly accepted, though most of its theoretical bases are still unexplained. In particular, the physical origin of the accelerated expansion is still unknown.

In subsection 2.4.1 we have derived the contribution of Cosmological Constant in the FLRW metric. If we set $T_{\mu\nu} = 0$, in equation (2.51) only the Λ term remains. It represents the *energy of vacuum* that provides a repulsive force in contrast to gravity. Λ is described by an EoS with $w_\Lambda = -1$. It can be noted that density of Λ is constant throughout the expansion of the Universe (eq. (2.61)), $\rho_\Lambda = \Lambda c^2/8\pi G$ (in line with the effective density term in eq. (2.53)).

The *deceleration parameter* is defined as follows:

$$q(t) \equiv -\frac{a(t)\ddot{a}(t)}{\dot{a}^2(t)}. \tag{2.67}$$

The deceleration parameter of a Universe composed of only matter, so with $w = 0$ and without any pressure term, is $q = \Omega_m/2$. This corresponds to a decelerated expansion (given the negative sign in eq. (2.67)), in contrast to observational evidences. Now let us consider a Universe composed of matter and Λ. The First Friedmann Equation will become

$$\ddot{a} = -aH^2\frac{\Omega_m}{2} + aH^2\Omega_\Lambda = -aH^2\left(\frac{\Omega_m}{2} - \Omega_\Lambda\right) = -aH^2 q. \tag{2.68}$$

If the expansion is accelerated, then $q < 0$ and the following condition has to be satisfied:

$$\Omega_\Lambda > \frac{\Omega_m}{2}. \tag{2.69}$$

Moreover, q_0 can be constrained from the relation between z and the magnitude of Supernovae type Ia. The current observations leads to a negative value of the deceleration parameter

$$q_0 \simeq -0.55, \tag{2.70}$$

corresponding to $\Omega_{0,m} \simeq 0.3$ and $\Omega_{0,\Lambda} \simeq 0.7$. Adding together the individual values Ω_{0,w_i}, the Universe results to be flat ($\sum_i \Omega_{0,w_i} = 1$). As stated in the subsection 2.4.2, the early Universe is well described by an EdS model, having $\ddot{a} < 0$. However, the recent

observed acceleration implies a change of $\ddot{a}$ at late times. This change (or flex) occurs at $z_f \simeq 0.68$, as shown in Figure 2.1. By imposing $\Omega_m(z_{eq_\Lambda}) = \Omega_\Lambda(z_{eq_\Lambda})$, we obtain the redshift equivalence, $z \simeq 0.33$. The observational fact that the present values of the densities of DE and DM are of the same order of magnitude implies that we are living in a peculiar moment of the history of the Universe. A density ratio $\rho_{\Lambda,0}/\rho_{m,0} \approx \mathcal{O}(1)$ at the present epoch can be seen as coincidental, since it requires very special initial conditions in the early Universe. This is what is generally called the cosmological *Coincidence Problem* (Velten et al., 2014).

2.6 Gravitational Jeans Instability

The *Jeans theory* on gravitational instabilities is now regarded as one of the cornerstones of the standard model. In 1902, Jeans demonstrated the existence of this instability in interstellar gas clouds to explain the formation of stars (Jeans, 1902). Starting from a homogeneous and isotropic fluid, small fluctuations can evolve in time, when the internal gas pressure is unable to counteract the gravitational pull.

As discussed in section 2.5, the CMB, as a fossil of the density perturbations, presents fluctuations with small amplitude, observed close to the recombination epoch. By analysing the CMB spectrum, it has been possible to derive the amplitude of temperature perturbations

$$\frac{\delta T}{\overline{T}} \approx 10^{-5}, \tag{2.71}$$

where $\overline{T} = 2.72548 \pm 0.00057 K$ is the mean Black Body temperature of the CMB radiation (Fixsen, 2009). Current observations showed that the Universe seems to be rather inhomogeneous at megaparsec scales, as result of a non-linear evolution (Peacock and Dodds, 1996).

The overdense regions of the Universe are capable to attract matter from nearby underdense regions. This process thus amplifies the inhomogeneities. The Jeans theory provides an analytical description of this phenomenon in the linear regime. It describes just non-relativistic matter, on scales inside the *particle horizon*, that is the spherical region causally connected with an observer defined as

$$R_H(t) \equiv \int_0^t \frac{c\,\mathrm{d}t'}{a(t')}. \tag{2.72}$$

The particle horizon separates two different regions. The region beyond R_H is totally dominated by gravity, and needs a relativistic treatment. While on scales below R_H, the Jeans theory can be used to describe the evolution of perturbations.

The Jeans instability describes the dynamics of a self-gravitating fluid. We shall begin by investigating the case of a collisional gas in a static background. Subsequently, we will extend the discussion to an expanding Universe towards a non-linear regime.

2.6.1 The Jeans Instability in a Static Universe

By assuming the Newtonian approximation, we consider a homogeneous and isotropic fluid, having a constant matter density ($\rho(\mathbf{x},t) = const$) embedded in a static framework. The equations of motion of such a fluid are the following

$$\begin{cases} \dfrac{\partial \rho}{\partial t} + \nabla \cdot \rho \mathbf{v} = 0 \\ \dfrac{\partial \mathbf{v}}{\partial t} + (\mathbf{v}\cdot\nabla)\mathbf{v} + \dfrac{1}{\rho}\nabla p + \nabla\Phi = 0 \\ \nabla^2\Phi - 4\pi G\rho = 0 \\ p = p(\rho, S) = p(\rho) \\ \frac{\mathrm{d}S}{\mathrm{d}t} = 0 \end{cases} . \tag{2.73}$$

These are the *continuity equation*, the *Euler equation*, the *Poisson equation*, the *equation of state* and the *adiabatic condition*, respectively. In this set of equations, $\mathbf{v}$ is the velocity vector of a fluid element, Φ the gravitational potential, ρ the density, p the pressure and S the Entropy. The last equation has been introduced, to neglect any dissipative terms, i.e. viscosity or thermal conduction.

Let us define the dimensionless density perturbation, the so-called *density contrast*, for the background as

$$\delta(\mathbf{x}, t) \equiv \frac{\delta\rho(\mathbf{x}, t)}{\rho}. \tag{2.74}$$

We consider small fluctuations, so that $\delta \ll 1$. We can thus linearise the equations in (2.73). The density equation becomes a differential equation which in Fourier space reads

$$\ddot{\delta}_{\mathbf{k}} + (k^2 c_s^2 - 4\pi G\rho)\delta_{\mathbf{k}} = 0, \tag{2.75}$$

where $k = |\mathbf{k}|$ is the absolute value of the wavenumber, $\delta_{\mathbf{k}} = \delta_k(t)$ is the Fourier transform of $\delta(\mathbf{x}, t)$, c_s the speed of sound (as defined in eq. (2.56)). The previous differential equation has two independent solutions of the form

$$\delta_{\mathbf{k}} = \delta_{\mathbf{k},0} \exp(\pm i\omega t), \tag{2.76}$$

where

$$\omega(k) = \sqrt{k^2 c_s^2 - 4\pi G\rho}\,. \tag{2.77}$$

The solutions are of two types, according to whether the wavelength $\lambda = 2\pi/k$ is greater than or lower than the *Jeans length*:

$$\lambda_J = \frac{2\pi}{k_J} \equiv c_s\sqrt{\frac{\pi}{G\rho}}\,. \tag{2.78}$$

In the $\lambda < \lambda_J$ case, we obtain two sound waves in the directions $\pm\mathbf{k}$, corresponding to two adiabatic perturbations with a phase velocity $c_{ph} = \omega/k$. The latter tends to become equal to c_s, when $k \gg k_J$ (or $\lambda \ll \lambda_J$). Instead, when $\lambda > \lambda_J$, the frequency ω is imaginary and we obtain a non-propagating solution (*stationary wave*) of ether increasing or decreasing amplitude. The characteristic timescale for the propagation is

$$\tau = |\omega|^{-1} = \sqrt{\frac{1}{4\pi G\rho_0\left(1 - \left(\frac{\lambda_J}{\lambda}\right)^2\right)}} \tag{2.79}$$

For very large scales, $\lambda \gg \lambda_J$, the gravity force leads and the perturbations can grow up with an exponential behaviour in time, tending to a *free-fall collapse*, $\tau_{ff} \sim (G/\rho_0)^{-1/2}$. This is the so-called *Jeans instability*.

2.6.2 The Jeans Instability in an Expanding Universe

Let us now consider an expanding homogeneous and isotropic Universe. In this framework, the background density evolves as a function of time, $\rho_B = \rho_B(t)$. The continuity equation becomes

$$\dot{\rho}_B + 3H(t)\,\rho_B = 0. \tag{2.80}$$

Now let us introduce a small perturbation into the set of equations (2.73) as before, and consider a double component velocity as

$$\mathbf{u} = \dot{\mathbf{x}} = H(t)\mathbf{x} + \mathbf{v_p}. \tag{2.81}$$

The first term on the right-hand side of eq. (2.81) results directly from the Hubble Law, while the second term is the *peculiar velocity* due to the inhomogeneous distribution of matter in the Universe and it represents the perturbation with respect to the Hubble flow. Given that the unperturbed solutions have no scale dependencies, we can search for

solutions for each Fourier mode of the type shown in eq. (2.76). The resulting equation is the so-called *dispersion relation*

$$\ddot{\delta}_{\mathbf{k}} + 2H(t)\dot{\delta}_{\mathbf{k}} + (k^2 c_s^2 - 4\pi G\rho)\delta_{\mathbf{k}} = 0. \tag{2.82}$$

The $2H(t)\dot{\delta}_{\mathbf{k}}$ term is related to the Hubble friction, that hampers the growth of perturbations, while the $k^2 c_s^2 \delta_{\mathbf{k}}$ term describes the characteristic fluid velocity. For wavelengths λ such that the second term in the parenthesis of eq. (2.82) is lower than the first one and when $\lambda \ll \lambda_J$ with

$$\lambda_J \simeq c_s \sqrt{\frac{\pi}{G\rho}}, \tag{2.83}$$

we obtain two oscillating solutions. The solutions of this dispersion relation have the following form

$$\delta(\mathbf{x}, t) = A(\mathbf{x})\delta_+(t) + B(\mathbf{x})\delta_-(t), \tag{2.84}$$

where A and B are two functions that depend on the comoving coordinates, while the time-dependent terms, δ_+ and δ_-, represent the growing and decaying modes, respectively.

In the $\lambda \gg \lambda_J$ case there are two solutions, one of which leads to instability. Indeed, for an EdS Universe (with $\Omega_m = 1$) the two solutions have the following trends:

$$\delta_-(t) \propto t^{-1} \propto a^{-3/2} \tag{2.85}$$

and

$$\delta_+(t) \propto t^{2/3} \propto a. \tag{2.86}$$

The first solution decays and does not give rise to the formation of structures, while the second one leads to gravitational instability.

For a Universe with a cosmological constant, the growing instability solution has the following integral form

$$\delta_+(z) = H(z) \int_z^\infty \frac{\mathrm{d}z'(1+z')}{a_0 H^3(z')}. \tag{2.87}$$

A more complex model, describing a multi-component Universe, has not such a general integral expression, and so the differential equation has to be solved directly. We can provide an approximate formula to parametrise the previous findings, the so-called *growth factor*, as a function of the density parameter evaluated at $z = 0$:

$$f(\Omega_0) = \frac{\mathrm{d}\log\delta_+}{\mathrm{d}\log a} \simeq \Omega_{m,0}^{0.55} + \frac{\Omega_{\Lambda,0}}{70}\left(1 + \frac{1}{2}\Omega_{m,0}\right). \tag{2.88}$$

This formula shows that Λ does not play a crucial role for the growth of the fluctuations. The exponent $\gamma \simeq 0.55$ is a result of General Relativity and it represents a method to test this theory on cosmological scales (Coles and Lucchin, 2002).

2.6.3 THE LINEAR REGIME THEORY

To describe the distribution of matter in the whole Universe at a given cosmological time and its following evolution, one can divide the entire volume into several independent sub-volumes. Nevertheless, these sub-volumes will not stay independent long, because of gravity action. So, it is convenient to describe a generic fluctuation as a superposition of plane waves in Fourier space, that have the advantage to be independent during the evolution. This approach requires a statistical treatment of the initial perturbations.

The spatial Fourier transform of the $\delta(\mathbf{x})$ is

$$\delta(\mathbf{k}) = \frac{1}{(2\pi)^3} \int \delta(\mathbf{x}) \exp(-i\mathbf{k}\cdot\mathbf{x})\, \mathrm{d}\mathbf{x}. \tag{2.89}$$

Let us define the *Power Spectrum* of the density field as follows

$$\langle \delta(\mathbf{k}) \delta^*(\mathbf{k}') \rangle = (2\pi)^3 P(k) \delta_D^{(3)}(\mathbf{k} - \mathbf{k}'), \tag{2.90}$$

where $\delta_k^* = \delta_{-k}$ (because of the reality of δ) and $\delta_D^{(3)}$ is the 3D *Dirac delta function*. Moreover, we introduce the *two-point correlation function* (from now on, 2PCF), that quantifies the spatial clustering of the objects, defined as

$$\xi(\mathbf{r}) = \langle \delta(\mathbf{x}) \delta(\mathbf{x}') \rangle, \tag{2.91}$$

where $\mathbf{r}$ is the comoving distance between $\mathbf{x}$ and $\mathbf{x}'$. It quantifies the probability excess, dP_{12}, compared with that expected one, of finding a pair of objects separated by a comoving distance r, in two comoving volume elements dV_1 and dV_2, respectively:

$$dP_{12} = n^2 [1 + \xi(r)] dV_1 dV_2, \tag{2.92}$$

where n is the mean comoving number density of the sample. The *Wiener-Khintchine theorem* relates the power spectrum to the *two-point correlation function*, $\xi(r)$, (2PCF) via a Fourier transform:

$$\xi(\mathbf{r}) = \frac{1}{(2\pi)^3} \int P(k) \exp(-i\mathbf{k}\cdot\mathbf{r})\, \mathrm{d}\mathbf{r}. \tag{2.93}$$

The inflation scenario[1] states that the distribution of current structures is generated by stochastic primordial quantum fluctuations. One of its predictions is that the power spectrum, $P(k)$, is described by a *power law*

$$P(k) = Ak^n, \tag{2.94}$$

where A is the amplitude and n is called *spectral index*, that is predicted to be close to 1. The growth in the linear regime does not alter the value of n, while A may change.

The distribution of a stochastic perturbation field is well described by a Gaussian function. Although the mean value of perturbations is null, its mean square value is not. This quantity is the *variance* σ^2

$$\sigma^2 = \langle \delta^2 \rangle = \sum_{\mathbf{k}} \langle |\delta_{\mathbf{k}}| \rangle = \frac{1}{V_u} \sum_{\mathbf{k}} \delta_k^2, \tag{2.95}$$

where the mean value is obtained from an ensemble of realisations. By considering the $V_u \to \infty$ limit and the framework in which the CP is valid, we obtain

$$\sigma^2 = \frac{1}{V_u} \sum_{\mathbf{k}} \delta_k^2 \to \frac{1}{2\pi^2} \int_0^\infty P(k) k^2 dk. \tag{2.96}$$

It can be noted that σ^2 does not depend on spatial position but only on time.

2.6.3.1 Mass Scales and Filtering

The variance does not contain any information on the relative contribution to the perturbations from different $\mathbf{k}$ modes. It provides a statistical description of the fluctuation field as a function of some resolution scale R. One can define the *mass variance* as

$$\sigma_M^2 \equiv \langle \delta_M^2 \rangle = \frac{\langle (M - \langle M \rangle)^2 \rangle}{\langle M^2 \rangle}, \tag{2.97}$$

where $\langle M \rangle$ is the mean mass contained into a spherical volume of radius R. The mass variance is the convolution of the *punctual variance*, σ^2, with a *window function*, $W(\mathbf{x})$. The direct link between the two quantities can be expressed in terms of the density contrast, as follows:

$$\delta_M(\mathbf{x}) = \delta(\mathbf{x}) * W(\mathbf{x}). \tag{2.98}$$

[1] The *inflation* theory describes the early Universe during its exponential expansion just after the Big-Bang. For further information, see Guth 1981.

Moving to a continuous distribution of plane waves as in eq. (2.96), the mass variance becomes

$$\sigma_M^2 = \frac{1}{(2\pi)^2}\int_0^\infty P(k)W^2(kR)k^2\,\mathrm{d}k < \sigma^2. \tag{2.99}$$

The main contribution to σ_M^2 is given by perturbations with $\lambda \simeq k^{-1} > R$, because those with higher frequencies tend to be averaged out within the window volume.

2.6.4 Towards the Non-Linear Evolution

The formation of structures, such as galaxies, clusters, haloes, filaments, walls, voids and the *Cosmic Web* in its entirely, is the result of gravitational instabilities occurred throughout the cosmological history.

Perturbations in the matter component δ on a scale $M > 10^5 M_\odot$ (the lower limit predicted by the Jeans theory) can evolve since $|\delta| \ll 1$ (Coles and Lucchin, 2002). The description reported in subsection 2.6.3 can no longer be used to follow the evolution of structures in the strongly non-linear regime, characterized by $\delta \gg 1$. When the density contrast, δ, reaches a value close to unit, the *quasi-linear* regime is achieved. Already at this stage, the fluctuation distribution function starts to take a non-Gaussian shape. So, some approximated peculiar analytical models have been proposed to describe what happens during this phase. However, for a detailed description, cosmologists are forced to rely on computations, such as N-body simulations, in order to model non-linear regimes.

Furthermore, also the spatial distribution of baryons changes during the evolution. This is different from the DM one, because of several further phenomena, for example hydrodynamical interactions, star formation and evolution, SNe, etc. The complexities of these phenomena make it difficult to construct a full and solid theory. In order to approximately model these effects, one can develop *semi-analytical* models (e.g., Lacey 2001) or can assume that the distribution of the objects is connected to δ via a simple analytic function (Scoccimarro 2000; Mo and White 1996; Bardeen et al. 1986; Kaiser 1984). By defining a discrete point-like distribution of objects, as $n(\mathbf{r}) = \sum_i \delta_d^{(3)}(\mathbf{r} - \mathbf{r}_i)$, the fluctuations in number counts are proportional to matter density ones, as follows:

$$\frac{\delta n}{\overline{n}} = b\,\frac{\delta\rho}{\overline{\rho}}. \tag{2.100}$$

The factor b is called the *linear bias parameter*. This parameter is used to quantify the difference between mass and galaxy clustering. Considering eq. (2.100) as a guess, one may use the linear approach on large scales to relate galaxy clustering statistics to the

density fluctuation statistics, as

$$P_g(k) = b^2 P(k). \tag{2.101}$$

This simple model is widely adopted, but it does not allow to provide a full description about of the complex relationship between galaxy formation and environment (e.g., Dekel and Lahav 1998).

2.6.4.1 THE ZEL'DOVICH APPROXIMATION

In order to extend the linear theory to the case of density perturbations slightly larger than unity with a good accuracy, we can use approximate methods, like the *Zel'dovich approximation* or the *Adhesion model*[2] (the latter is not explained in this compendium).

In the Lagrangian description of a cosmological fluid, one traces the path of a fluid element into space and time. Given the position, $\mathbf{q}$, of an element at t_0, its location at subsequent instants can be written in terms of the Lagrangian displacement field, $\mathbf{\Psi}$, as follows:

$$\mathbf{r} = a(t)(\mathbf{q}) + \mathbf{\Psi}(\mathbf{q}, t), \tag{2.102}$$

where the first term describes the expansion of the Universe.

It is conventional to consider the Zel'dovich approximation as a first-order Lagrangian perturbations theory. Furthermore, equation (2.102) assumes that the position and time dependences of the displacement between the initial position and the final one can be separated. Under this approximation, particles execute a kind of inertial motion on straight line trajectories.

2.7 N-BODY SIMULATIONS

Analytical studies allows to describe limiting cases of structure formation. Generally, gravitational dynamics is very complicated to be analytically treated. For this reason, cosmologists rely on N-body simulations, that is numerical methods able to study the large-scale structure formation and evolution.

The main advantage of N-body simulations is that they allow to examine the non-linear regimes of fluctuations, with no simplifying assumptions. Since the LSS is widely

[2]The Adhesion model is a method used to extend the Zel'dovich approximation, which is not able to deal with the problem of *shell-crossing*. For further information, see Padmanabhan 1993.

dominated by gravity exerted by DM, it is usually sufficient to analyse the behaviour of this component. Indeed, only in the last years a hydrodynamical description has been introduced, so that also the baryonic matter may be traced. Moreover, radiative transfer processes, such as cooling or heating of matter component can be introduced too, for a more detailed description.

Specifically, the most simple case of a N-body simulation only regards the gravitational action. A N-body problem may be described by the following dynamical system:

$$\begin{cases} \mathbf{F}_i = G M_i \sum_{i \neq j} \dfrac{M_i}{r_{ij}^2} \hat{r}_{ij}^2 \\ \ddot{\mathbf{x}} = \dfrac{\mathrm{d}\mathbf{v}_i}{\mathrm{d}t} = \dfrac{\mathbf{F}_i}{M_i} \\ \dot{\mathbf{x}} = \dfrac{\mathrm{d}\mathbf{x}_i}{\mathrm{d}t} = \mathbf{v}_i \end{cases} , \tag{2.103}$$

where $\mathbf{F}_i$ is the i-th component of the gravitational force, G is the *gravitational constant*, M_i is the i-th particle mass, $\mathbf{x}_i$ are the comoving coordinates of the i-th particle, $\mathbf{v}_i$ are the velocity components of the i-th particle, r_{ij} is the comoving distance between the i-th and j-th particles, and $\hat{r}_{ij}$ is the related versor. Since the system eq. (2.103), the *Euler equation* in eq. (2.73) can be re-expressed as follows:

$$\frac{\mathrm{d}\mathbf{v}_i}{\mathrm{d}t} + 2\frac{\dot{a}}{a}\mathbf{v}_i = -\frac{1}{a^2}\nabla\phi = -\frac{G}{a^3}\sum_{i \neq j} \frac{\mathbf{x}_i - \mathbf{x}_j}{\left|\mathbf{x}_i - \mathbf{x}_j\right|^3} = \frac{\mathbf{F}_i}{a^3}, \tag{2.104}$$

where a is the *expansion parameter*. By using the *Second Friedmann Equation* (eq. (2.45)), the *Poisson equation* in eq. (2.73) becomes

$$\nabla^2\phi = 4\pi G\bar{\rho}(t)a^2\delta = \frac{3}{2}H_0^2\,\Omega_0\frac{\delta}{a}, \tag{2.105}$$

where $\bar{\rho}(t)$ is the average density of the non-relativistic matter component.

A N-body simulation consists in the integration of the dynamical equations through discretized time steps, δt. At every time step, the total gravitational force of the system, $\mathbf{F}_i$, is computed. Then, the numerical integration of the motion equation is evaluated and the following positions, $\mathbf{x}_i(t+\delta t)$, and velocities, $\mathbf{v}_i(t+\delta t)$, are updated. The final output of a simulation is a set of snapshots, representing the evolution of particles at each instant, as a result of the acting force.

There are several computational techniques for developing a N-body simulation, differing in implementation, CPU efficiency, both spatial and mass resolutions, and more. In the following, we provide a brief description of some of the most used techniques.

Particle-Particle (PP) This method allows to compute the force acting on the i-th particle, as the sum of the contributes by the other $N_p - 1$ particles of the considered system. For this reason, this technique has the highest computational cost among the methods. In fact, the execution time of this algorithm is proportional to the square of the particle number, N_p^2. However, this method provides the most accurate description of the gravitational force, because it is estimated for all particles. Hence, this direct method does not introduce approximation in solving the motion equations.

Tree codes The tree code algorithms, firstly proposed by Barnes and Hut (1986), introduced a hierarchical tree subdivision of the considered simulation volume. The subregions are characterised by a proper centre of mass. It implies that the acting force from distant particles is approximated to the force exerted by the centre of mass of those regions. The resulting computational cost is proportional to $N_p \log(N_p)$. The resolution is increased, by subdividing the grid in cells until each cell has just one particle within.

Particle Mesh (PM) This computational technique determines the total gravitational force of a particle system, by implementing a grid, where a density value per cell is computed. Specifically, the Poisson equation is solved for the grid, and the force is applied to each particle. This method is faster than the PP one, but it is less accurate, due to the limited resolution of the considered grid.

Particle-Particle Particle Mesh (P^3M) The P^3M technique is based on the PM, but it enhances the latter by introducing a direct-summation force within a fixed-radius sphere. This algorithm is more accurate than the PM parent: in presence of zones with strong clustering, particles directly interact with each other. However, it implies an increasing of computational cost, which locally tends to be proportional to $\mathcal{O}(N_p^2)$. A way to reduce this problem consists in the implementation of an adaptive mesh, so that it is possible to redefine the local spatial resolution of overcrowded regions. The computational cost of the adaptive P^3M scales as $\mathcal{O}(N_p \log(N_p))$.

CHAPTER 3

Cosmic Voids in the Universe

Galaxies in the Universe are grouped into a complex spatial pattern. This pattern is often referred to as the *Cosmic Web*. This structure consists of elongated filaments and walls, that surround large nearly empty voids. At the nodes of the web, we find dense and compact clusters, agglomerates that have thousands of galaxies (Bond et al., 1998). The Cosmic Web is also confirmed by several large galaxy surveys (i.e. Alam et al. 2015; Guzzo and The Vipers Team 2013; Cole et al. 2005; Colless et al. 2003; de Lapparent et al. 1986). The presence of voids in the galaxy distribution has been identified even in the first redshift surveys. Over the past decade, the Sloan Digital Sky Survey (SDSS) (Tegmark et al., 2004) has provided a map of a large region of the nearby Universe, that reaches out to distances of hundreds of millions of light-years. The map consists of about a million of galaxies. Moreover, SDSS made entire void catalogues, such as those presented in Nadathur and Hotchkiss 2014 and Pan et al. 2012.

Under the gravitational influence of a homogeneous mass distribution, the tiny perturbations in the primordial density field start to grow. Matter starts to migrate towards the higher density regions; meanwhile, it evacuates the regions of lower gravitational attraction, to form low density regions: the so-called *Cosmic Voids*. Hence, voids emerge out of the density troughs in the primordial Gaussian field of density fluctuations.

In this chapter we discuss the first observations of cosmic voids (in section 3.1). In section 3.2 we illustrate the role of voids in a ΛCDM model and review some studies done by using them as both cosmological and astrophysical tools. Finally, we discuss about the most important features concerning voids, such as the structure properties (in

section 3.3), formation and evolution (in section 3.4) and dynamics (in section 3.5).

3.1 The Historical Discovery of Voids

In the late 70's, two different research groups observed for the first time giants voids. Both studies showed that there are large underdense volumes in the Local Universe having diameters of approximately 20 h^{-1} Mpc. These two papers were published in 1978, by Gregory and Thompson 1978 and then by Jõeveer et al. 1978.

The first group was empirically driven. Their aim was to understand the distribution of galaxies in and around what Abell had called the "second-order clusters" (Abell, 1961), that is groups of rich cluster cores. Their first target was the pair composed by the Coma and A167 clusters. They revealed the first void in the wide gap between the Milky Way and Coma/A167 pair.

The second research program was aimed at testing the specific model of structure formation proposed by Zel'dovich, who postulated the *top-down model* of galaxy formation, in which the largest structures are the first to form (Zel'dovich, 1970). Jõeveer et al., mapped the distribution of galaxies and clusters. They called those empty regions "big holes", while Gregory and Thompson were the first to call them "voids".

The discovery of cosmic voids changed dramatically the concept of the Large Scale Structure of the Universe. Before that, it was thought that the Universe was filled with field galaxies and occasional density enhancements could be located into rich galaxy clusters and superclusters. In the new state of the art, voids are disseminated between complex filamentary structures. The key observational prerequisite was a wide-angle redshift survey capable of showing a fair sample of the Universe. Systematic and quantitative studies came later with the arrival of the first large spectroscopic surveys (Bahcall, 1995; Geller and Huchra, 1989; Huchra et al., 1988). In fact, this discovery was hindered for several years, because it was unclear how filaments and voids could have emerged from what appeared to be a homogeneous Universe (Thompson and Gregory, 2011).

3.2 Voids in a ΛCDM Scenario

Cosmic voids delineate the transition scale at which density fluctuations have decoupled from the expanding flow of the Universe. Voids act as a trigger for arranging matter into the cosmic network (Sheth and van de Weygaert, 2004; van de Weygaert, 1991; Regos

and Geller, 1991; Icke, 1984). Indeed, as a consequence of the void expansion, matter is pushed and sheets and filaments take shape, forming void boundaries. Numerical simulations performed to describe the gravitational evolution of cosmic voids confirmed this view (Padilla et al., 2005; Colberg et al., 2005; Goldberg and Vogeley, 2004; van de Weygaert and van Kampen, 1993; Dubinski et al., 1993; Regos and Geller, 1991; Martel and Wasserman, 1990).

3.2.1 The Role of Voids

Several studies pointed out why voids are so intriguing and, above all, useful for cosmology. Their simple shape makes them relevant probes to constrain the value of cosmic parameters, such as the Dark Energy EoS. Indeed, voids provide a broad amount of information about the cosmological framework and relative parameters and they can be exploited to discriminate between competing cosmological models. Furthermore, void abundance and void lensing are possible probes to test for theories of gravity modified.

3.2.1.1 The Importance of Dark Energy

As stated in section 2.5, our Universe is now accelerating due to the presence of a "negative pressure" (Spergel et al., 2003; Perlmutter et al., 1999; Riess et al., 1998). We might consider voids as bubbles, the form of which is extremely sensitive to the cosmological background.

Lee and Park (2009) have demonstrated analytically that, by assuming a flat model, a value of matter density parameter, $\Omega_m = 0.75$, and a value of the dimensionless Hubble parameter, $h = 0.73$, the elliptical expansion of voids may be a sensitive tool able to constrain the Dark Energy Equation of State. (Lee and Park, 2009).

By using the `VIDE` toolkit, Sutter et al. (2015b) found that a model of coupled DM-DE produces a population of larger voids, while they did not find any statistical differences in the ellipticity, according to what argued by Tavasoli et al. (2013). Indeed the latter authors, using a sample of galaxies from the SDSS DR7 (Abazajian et al., 2009), compared the observed properties of the void catalogues with the results obtained from simulations (Mock Millennium I catalogue) based on the ΛCDM model and a semi-analytical model of galaxy formation. They found that voids tend to be spherical, both in observations and simulations. The number of voids and the total occupied volume obtained from simulations are slightly larger than in the observed data. This mismatch could be due to

the over-abundance of small-size haloes in the ΛCDM model (for further information, see Tavasoli et al. 2013 and references therein).

In addition to shape and relative dimensions, Pisani et al. (2015) showed that also the number of observed voids depends on the Equation of State of DE. In order to provide forecasts for the number of voids to be detected by the ESA Euclid satellite (Laureijs et al., 2011) and the NASA WFIRST mission (Spergel et al., 2013a,b), and to establish constraints on the Dark Energy EoS, they analysed the error ellipses in the $w_0 - w_a$ plane, by using a Fisher analysis (Fisher, 1925), considering a parametrization of the Dark Energy EoS given by the *Chevallier-Polarski-Linder* one (Linder, 2003; Chevallier and Polarski, 2001), $w_{CPL}(z) = w_0 + w_a z/(1+z)$[1]. In particular, they argued that void count is well performing to constrain $w(z)$, when added to other probes. Indeed, by combining void constraints to the SNe probe, the $w_0 - w_a$ space is considerably reduced, obtaining a value of w_0 between about -1.05 and -0.95 and a value of w_a between about -0.4 and 0.4 (as shown in figure 6 of Pisani et al. 2015).

Pollina et al. (2016) studied the properties of voids in two different cosmological models, the standard ΛCDM and the coupled DE (cDE). By using numerical simulations, they explored the influence of Dark Energy on the filling factor, the size distribution and the stacked void profiles. They report that the bias of the tracers of the density field affects significantly the void sampling. Moreover, they found that voids can discriminate between the two considered cosmological models.

3.2.1.2 Passive Evolution of Galaxies within Voids

Cosmic voids play a major role for testing the evolution of galaxies. Their pristine environment represents the ideal location to study galaxies in passive evolution, that is to investigate internal feedback phenomena in an environment where galaxy interactions are highly unlikely.

By examining the properties of galaxies inside mid-voids in the GAMA survey, Penny et al. (2015) identified almost six hundred voids and, inside them, 26 void galaxies, *retired* or *passive*, in accordance with the WHAN dignostic diagram[2] proposed by Cid

[1]The *Chevallier-Polarski-Linder parametrization* provides a description from a value of $w = w_0 + w_a$ at early epochs to a value of $w = w_0$ at $z = 0$, where a is the expansion parameter.

[2]The WHAN diagram combines the equivalent width of Hα (WHa) and [NII]/Hα to provide a classification of the ionization sources in a galaxy. Cid Fernandes et al. (2011) has classified five galaxy types in the WHAN diagram: *pure star-forming galaxy* (log ([NII]/Hα) < −0.4 and $W_{\mathrm{H}\alpha}$ > 3 Å), *strong AGN* (log ([NII]/Hα) > −0.4 and $W_{\mathrm{H}\alpha}$ > 6 Å), *weak AGN* (log ([NII]/Hα) > −0.4 and 3 Å < $W_{\mathrm{H}\alpha}$ < 6 Å), *retired galaxy* ($W_{\mathrm{H}\alpha}$ < 3 Å) and *passive galaxy* ($W_{\mathrm{H}\alpha}$ < 0.5 Å and $W_{[NII]}$ < 0.5 Å).

Fernandes et al. (2011), having old stellar populations.

Using the SDSS catalogue in the nearby Universe ($z < 0.025$), Kreckel et al. 2014 selected 59 galaxies for a new Void Galaxy Survey (VGS). This selection was obtained by applying the Delaunay Tessellation Field Estimator to recover the DM density field (van de Weygaert and Schaap, 2009; Schaap and van de Weygaert, 2000). Through UV, optical, Hα, IR and HI imaging, the authors examined morphologies, kinematics and dynamics of that galaxy components and studied the statistical properties of void galaxies. They noticed that void galaxies typically have a large amount of HI-gas in their disks. A large sample of sources shows disturbed gas morphologies or kinematics, whereas it is nevertheless a standard feature for galaxies with the same stellar mass in an average density environment. It can be concluded that while the large scale environment affects the shape during the evolution of void galaxies, at fixed stellar mass the galaxy HI properties are quite independent of the environment.

3.2.1.3 The Void Phenomenon

Some studies need for alternative cosmological models, as for instance, the cDE scenario (Baldi, 2011; Farrar and Peebles, 2004; Amendola, 2004, 2000; Wetterich, 1995). Although the ΛCDM model is widely accepted and fully consistent with most of the available observations, there are still some possible problems. Cosmic voids allow to analyse the behaviour of isolated sources. The *deficit* of dwarf galaxies in nearby voids is a potential evidence against the standard scenario (Peebles, 2001). The termed *Void Phenomenon*, introduced by Peebles (2001), refers to the tendency of early-type galaxies (ETG) to be preferentially located in high-density regions (Hubble, 1936), while rich-gas and star-forming galaxies reside in the void edges (Thompson, 1983; Lee et al., 2000; Salzer et al., 1990). This leads to a *morphology-density* correlation (Dressler, 1980). The mismatch can be alleviated if the formation of observable voids is suppressed, or by properly reviewing the model for structure formation.

Tinker and Conroy (2009) analysed the properties of cosmic voids, by using N-body simulations and halo occupation distribution (HOD) models, in order to provide a solution for the void phenomenon. By assuming that the galaxy luminosity is a function of DM halo mass, they demonstrated that voids with diameters of $\simeq 15\,h^{-1}$ Mpc are expected also for sources having seven magnitudes lower than the L_*. Their results support a scenario in which the galaxy formation is driven mainly by the DM haloes. Moreover, they assert that a standard ΛCDM model, supported by an appropriate bias description,

may predict the void phenomenon as a dearth of faint objects (for further details, refer to Tinker and Conroy 2009).

3.2.1.4 The Impact on the Cosmic Microwave Background

There are still controversial anomalies represented by the presence of very large cosmic voids along the line-of-sight (los), such as the Cold Spot (CS) in the Cosmic Microwave Background. The CS is a large cold region in the CMB (Vielva et al., 2004) that could have been originated by the presence of a structure along the los, or by a primordial fluctuation on the last scattering surface. Finelli et al. (2014a) looked for a supervoid in this region, at $z < 0.3$, and Kovács and Szapudi (2015) found a wide underdense region in the WISE-2MASS catalogue. They showed for the first time that the CMB and void profiles can be fit assuming the LTB (Lemaître-Tolman-Bondi) model (further information in Garcia-Bellido and Haugbølle 2008). This description appears to explain exactly the CS anomaly (more details in Finelli et al. 2014a,b and references therein).

According to these works, Nadathur et al. (2014) examined the CS. Research studies carried out to investigate the CMB secondary anisotropies (due to the presence of under/overdensities) explained this phenomenon through the combination of the *Integrated Sachs-Wolfe* (ISW) (Sachs and Wolfe, 1967) and the second-order *Rees-Sciama* (RS) (Rees and Sciama, 1968) effects (e.g., Inoue et al. 2010; Inoue 2012; Inoue and Silk 2007, 2006). Nadathur et al. (2014) estimated the true temperature of the supervoid using the LTB model and perturbation theory, and found that the RS effect is much smaller than the contribution of ISW anisotropy, in contrast to the previous findings.

The potential of the ISW effect in cosmic voids is still under investigation, through complementary studies on the CS (Naidoo et al., 2016), but also on other structures (Kovács and García-Bellido, 2016), or on the CMB analysis (Kovács and Granett, 2015).

3.2.1.5 The Alcock-Paczynski Test

One of the most common and effective cosmological application of cosmic voids is through the *Alcock-Paczynski test* (AP) (Alcock and Paczynski, 1979). The AP test is a geometric probe of the expansion of the Universe, because it estimates the shapes of objects that are known to be isotropic. An uncorrected assumption on the cosmological model leads to a stretched or elongated view of the objects along the los. So, the AP test provides the ratio between the observed angular size and the radial size. The main advantage is that this test does not depend on the evolution of galaxies. In fact, it only depends on

the geometry of the Universe. The AP test can be performed through the 2PCF, that is expected to have a spherical symmetry in real space, in an isotropic Universe. Hence, the 2PCF shape has to be the same along the los ($r_\parallel$) and across it ($r_\perp$), where

$$r_\parallel = \frac{c}{H(z)}\Delta z, \qquad r_\perp = D_A(z)\Delta\theta. \tag{3.1}$$

These, in turn, depends on the Hubble rate

$$H(z) = H_0\sqrt{\Omega_m(1+z)^3 + \Omega_\kappa(1+z)^2 + \Omega_\Lambda}, \tag{3.2}$$

and the angular diameter distance

$$D_A(z) = \frac{c}{H_0\sqrt{-\Omega_\kappa}}\sin\left(H_0\sqrt{-\Omega_\kappa}\int_0^z \frac{1}{H(z')}\mathrm{d}z'\right), \tag{3.3}$$

with the Hubble constant H_0, the matter content Ω_m, the energy content Ω_Λ and the curvature Ω_κ evaluated today. The distance between two sources perpendicular to the los is the angular separation, $\Delta\theta$, while the the distance along the los is the difference of redshifts, Δz (for further details and uses of the AP test, see Li et al. 2015; Melia and Lopez-Corredoira 2015; López-Corredoira 2014). The AP test can be performed by measuring the size of stacked voids along and across the los, and looking for a possible mismatch that could arise due to an uncorrected assumption of the cosmological model (Sutter et al., 2014a, 2012).

The first use of the AP test with cosmic voids has been provided by Sutter et al. (2012). In particular, they considered 10 voids from the SDSS Data Release 7 (Abazajian et al., 2009) and used a modified version of the ZOBOV void finder (Neyrinck 2008, described in chapter 4). Sutter et al. (2012) performed the test by measuring the ellipticities of stacked voids. The stacking, in addition to reduce the noise, allowed them to apply the *shape-fitting method* (Lavaux and Wandelt, 2012). However, the stretch induced by the stacked voids did not provide any indication of geometrical distortions. Two years later, Sutter et al. 2014b performed the AP test using about 1500 stacked voids from the SDSS-DR7 main sample, SDSS-DR10 (Ahn et al., 2014) LOWZ and CMASS galaxy catalogues and implemented VIDE (as a heavily modified and extend version of ZOBOV). From the application of the AP test, they derived a best-fitting value of the signal corresponding to $\Omega_m \simeq 0.15$.

3.3 Void Morphology

Observations of cosmic voids have become more accurate and deeper during the last years and able to cover ever greater areas. Nowadays, it is well accepted that the range of

void radii is very wide, from *minivoids* to *supervoids*. Tikhonov and Karachentsev (2006) considered a sample composed by 355 galaxies. They founded six minivoids ($\simeq 30\,\mathrm{Mpc}^3$) in the Local Universe occupying 58% of the volume, around which there are 24 middle-size "bubbles" ($\simeq 5\,\mathrm{Mpc}^3$) and 52 small "pores". The identification of these voids, with radii of about $1-3\,\mathrm{Mpc}$, was based on theoretical assumptions by Peebles (2001). Tikhonov et al. (2009), using high-resolution simulations in Cold and Warm Dark Matter models, compared the Local mini-void spectrum with the one obtained from simulations. They concluded that a Warm DM model (ΛWDM) is able to explain the observed spectrum of mini-voids in our Local Universe. However, a potential problem in preferring a ΛWDM is represented by the late formation of DM haloes, in which gas can be photo-evaporated (further information is available in Tikhonov et al. 2009). On the other hand, supervoids have radii of the order of 100 Mpc. An example is the Northern Local Void, the empty region surrounded by the Local, Coma and Hercules superclusters. Lindner et al. (1995) argued that there is a hierarchical fine structure into this void, such as a system of galaxies and poor clusters. Furthermore, they highlighted that voids embedded in high-density environments are smaller than voids located in low-density regions (see Lindner et al. 1995 and references therein). Another classical example of supervoid is the Boötes void, having approximately a $10^6\,\mathrm{Mpc}^3$ volume (Kirshner et al., 1987, 1981).

Cosmic voids account for about 95% of the entire volume of the Universe (Platen et al., 2007; Rojas et al., 2005; Fairall and Kauffman, 1991). It should be noted that void sizes depend on the sample population used to find them. Hoyle and Vogeley (2002) highlighted that voids identified by using bright galaxies usually have diameters in the range $10-20\,h^{-1}\,\mathrm{Mpc}$, while voids defined from low-luminosity galaxies have diameters above $30\,h^{-1}\,\mathrm{Mpc}$, according to the problem of void sampling.

3.4 Formation and Evolution of Voids

Cosmic Voids are a manifestation of the process of structure formation in the Universe. The first theoretical models of the formation of these empty regions focused on the evolution of isolated voids. The low-density environments expand faster than the Hubble flow, and thus expand with respect to the background Universe. As matter streams out of the voids, the value of density decreases asymptotically to $\delta = -1$. Since the density gradually decreases going towards the centre of void, matter in the centre moves outward faster than matter in the external boundaries. This implies that objects accumulate around the voids.

An important timescale characterising the void evolution is related to the *shell-crossing*. The shell-crossing effect occurs when interior shells of matter take over the external ones. Bertschinger (1985) demostrated that after the shell-crossing stage there is a phase of *self-similar expansion*, which slows down with respect to the earlier phases. Blumenthal et al. (1992) identified voids in the local galaxy distribution that reach the shell-crossing step. It occurs when a primordial depression in density reaches a linearly extrapolated underdensity, $\delta_v = -2.81$, for an EdS Universe. The spherical evolution of voids was proposed by Gunn and Gott (1972). The model considers a spherical underdensity inside a homogeneous background. The evolution of each radius is determined by the mass within it. This model allows to solve the evolution of under/overdensities (Sheth and van de Weygaert, 2004; Lilje and Lahav, 1991; Peebles, 1980). The spherical *bucket* void has evolved into an underdensity that corresponds to $\delta_{v,n-l} = -0.8$. Nowadays, the cosmic voids are generally defined as regions having a density of about 20% of the mean density of the Universe.

3.5 VOID DYNAMICS

The main features of an expanding void can be assessed by examining its density and velocity profiles. The velocity profile of a void is directly linked to that of the density field, by the relation

$$\Theta = \frac{\nabla \cdot \mathbf{v}}{H}. \tag{3.4}$$

A growing velocity implies an expansion of the void. Since voids are emptier than average structures, their expansion will be faster than the Hubble-flow, with a velocity divergence equal to

$$\nabla \cdot \mathbf{v} = 3(H_v - H), \tag{3.5}$$

where H_v is the *super-Hubble flow* expected for a void.

Recently, Hamaus et al. (2016) constrained some cosmological parameters by examining the dynamics of voids. Using `VIDE`, they identified 3457 voids spread over the range of $0.43 < z < 0.7$, in a volume of about $3.5\,h^{-3}\,\mathrm{Gpc}^3$, from the Baryon Oscillation Spectroscopic Survey (BOSS) (Dawson et al., 2013) of the SDSS-III (Eisenstein et al., 2011), in particular the CMASS sample from DR11 (Alam et al., 2015). They obtained a constraint on the average matter content, $\Omega_m = 0.281 \pm 0.031$, and on the linear growth rate of structures, $f/b = 0.417 \pm 0.089$, at the median redshift $\overline{z} = 0.57$, where b is the galaxy bias (more details in Hamaus et al. 2016).

Further information about the formation, evolution and dynamics of Cosmic Voids is available in Padilla et al. (2014) and van de Weygaert and Platen (2011).

3.5.1 From Aspherical to Spherical Shapes

Icke (1984) argued that the isolated underdense regions, initially aspherical, tend to become spherical, due to their expansion. Gravity acts more strongly along shorter axes than along longer ones. This implies that voids undergo outward accelerations along their minor axes, so that their asphericity gets less and less during the expansion. In particular, van de Weygaert and van Kampen (1993) showed this behaviour in the void internals, by using N-body simulations. They analysed the structure and dynamics of isolated underdense regions in a gravitational instability regime, in an EdS scenario. They did not considered spherical voids, but rather low-density regions in a density fluctuation field. Hence, they examined the structure and kinematics dependencies of cosmic voids on their initial depth and on the perturbed background field. This analysis revealed the effect of small perturbations on the dynamics of large voids, and how void internal structures are affected by the surrounding environment. In addition, they found that the central regions of void tend to be more and more spherical during the non-linear evolution, while the properties of void boundaries are affected by the influence of the structures surrounding them. These structures make the external shells more irregular (more details in van de Weygaert and van Kampen 1993). Indeed, voids never reach a total sphericity. Platen et al. (2008) studied the shapes and the mutual alignment of voids in the LSS distribution of a ΛCDM simulation. The identified cosmic voids that are slightly prolate, having axes ratios in the order of $c : b : a \approx 0.5 : 0.7 : 1$. Indeed, cosmic voids are quite non-spherical. Further studies confirmed the non-sphericity of voids. For instance, Shandarin et al. (2006) investigated the distribution of voids in N-body simulations for a ΛCDM cosmology. In order to examine the void shapes, they fit the void profiles with ellipsoids. They defined three parameters: the *Sphericity*, α, that is the ratio between the smallest and the largest axes, c/a; the *Porosity*, that is the ratio $P = V_{\rm E}/V_{\rm V}$, where $V_{\rm E}$ is the volume of the ellipsoid, $V_{\rm E} = (4\pi/3)abc$, and $V_{\rm V}$ is the volume of considered void; and the *Inverse Porosity* that is defined as $IP = V_{\rm V}/V_{\rm E}$. They derived a mean value of $\alpha \approx 0.45$, that is correspond to a non-spherical shape. Furthermore, the P values that they estimated showed that larger voids are more porous than smaller ones, that appear more regular.

The void shape can be also affected by tidal forces. External tidal stresses can be responsible of strong anisotropic distortions of voids, during their evolution. To quantify

these tidal effects, Lee and Park (2006) introduced the concept of *void spin* (details about notation are provided in the article). In their work, they used both analytical and numerical approaches. In particular, they considered a *linear-tidal torque* model to derive analitically the *void spin-spin* and *spin-density* correlations. Moreover, they used on the Millennium Run galaxy catalogue to identify voids and measure their spins. The authors obtained an excellent agreement between the two methods. Subsequently, Park and Lee (2007) extended their work in order to demonstrate the correlation between cosmic voids and surrounding superclusters, by using the Millennium Run too. They found that the void spin axes is extremely correlated with the minor axes of superclusters, with negligible dependences on void and superclusters definitions. They also derived an analytical relation, linking both axes, that has turned out to be in agreement with numerical results.

CHAPTER 4

LOOKING FOR COSMIC VOIDS

The detection of Cosmic Voids is not a trivial task. For this reason, during the last decades, many Void Finder algorithms have been proposed. In this chapter we illustrate the properties of some Void Finders and discuss the problems arising due to the shot noise sampling. In section 4.1, we illustrate the three main classes of void finders proposed by Lavaux and Wandelt (2010). In section 4.2, we describe in details some Void Finders, belonging to the different categories. Finally, in section 4.3, we review the *Aspen-Amsterdam void finder comparison project* (Colberg et al., 2008), and we discuss the main results.

4.1 THREE CATEGORIES OF VOID FINDERS

Lavaux and Wandelt (2010), in the same article in which the `DIVA` (subsection 4.2.6) algorithm is presented, proposed to classify the Void Finder algorithms in three different broad classes, based on the criterion used to identify these regions. Specifically, the three classes are based on *density*, *geometrical* and *dynamical* criteria.

Density criterion This first class includes Void Finders that identify cosmic voids as regions empty of galaxies, or at least with densities lower than a given fraction the mean cosmic density (e.g. Micheletti et al., 2014; Elyiv et al., 2013; Foster and Nelson, 2009; Brunino et al., 2007; Patiri et al., 2006; Gottlöber et al., 2003; Hoyle and Vogeley, 2002; El-Ad et al., 1997; Kauffmann and Fairall, 1991). Tracers, tipically galaxies, are divided

in two general types: *wall tracers* and *field tracers*. The former reside in high-density regions, while the latter lie in *mildly* underdense regions. The separation between the two depends on an *ad hoc* parameter that is a fraction of the local density of tracers. Cosmic voids are regions empty of wall tracers.

Geometrical criterion This second class of algorithms detects cosmic voids as underdense geometrical structures, such as spherical cells, polyedra, etc (e.g. Sutter et al., 2015b; Neyrinck, 2008; Platen et al., 2007; Shandarin et al., 2006; Colberg et al., 2005; Plionis and Basilakos, 2002). These Void Finders search for particular features in the continuous 3D distribution of cosmic tracers. The mass density field is reconstructed from these features. After the reconstruction, the local density minima are used to obtain the void distribution.

Dynamical criterion This class is characterized by Void Finders that identify the structures dynamically, by analysing gravitationally unstable points in the matter distribution, using galaxies as test particles of the cosmic velocity field (e.g. Elyiv et al., 2015; Lavaux and Wandelt, 2010; Forero-Romero et al., 2009; Hahn et al., 2009).

The third class of Void Finders is significantly different from the previous two categories. The most striking feature that distinguishes these methods from the other two classes is that it assumes a different definition of what a cosmic void is. Indeed, voids are generally defined as underdense regions of space. In this case, instead, a void is a region in which matter runs away. So, the definition of void centre is also different. In this case, it is the point from which particles escape with the maximal velocity.

The first two classes of Void Finders identify voids from the Eulerian positions of tracers. This approach has two disadvantages. The former is a direct consequence of considering galaxies as *mass tracers*. This requires to adopt some biasing descriptions to explain the relation between the galaxy distribution and the density field, that has to be considered when voids are used to discriminate among different cosmological models (Pollina et al., 2016). The second problem regards the large *shot noise error* caused by the few galaxies used to identify voids as underdense volumes. The Void Finders belonging to the third class have the advantage that they can be defined in Lagrangian coordinates. This considerably reduces the shot noise problem.

4.2 Some Specific Void Finder Algorithms

In this section we analyse more accurately some Void Finders belonging to each of the categories discussed in the previous section.

4.2.1 Patiri's Geometrical Void Detection

In order to perform statistical analyses using the 2df Galaxy Redshift Survey (2dFGRS) (Colless et al., 2003), Patiri et al. (2006) used two different complementary Void Finder algorithms.

The first method is called `CELLS void finder`. It is designed to look for cosmic voids in galaxy or halo samples on a grid, which defines the working resolution. `CELLS` determines void centres computing the distances between each of the empty cells and all the galaxies (or haloes) in the entire sample, keeping the minimum distance. A list with the minimum distances is obtained. The algorithm then searches for the local maxima, corresponding to the void centres. Naturally, the radius of a void is the maximum distance.

The second method is dubbed `HB Void Finder`. This algorithm looks for the maximal non-overlapping spheres, having a radius greater than a given threshold. By generating a random distribution of spheres, with a fixed radius, `HB` finds all the empty-galaxy spheres. The following step consists in "inflating" these spheres until they find objects around them. The overlapping spheres are removed from the final catalogue and the larger ones are kept.

4.2.2 Void Detection in VIPERS

The VIMOS Public Extragalactic Redshift Survey (VIPERS) (Garilli et al., 2014) is an ESO programme with the purpose of examining the LSS distribution of galaxies at $z = 0.5-1.2$, in a covering total sky area of 24 deg^2. Similarly to the `HB Void Finder`, Micheletti et al. (2014) implemented an algorithm for the void detection using empty spheres. In this case, cosmic voids are defined as volumes empty of galaxies, the latter having an absolute magnitude B-band brighter than $M_B = -19.8$. This method has one disadvantage: a single sphere is not always able to entirely cover an empty region, and so, to reconstruct the void shape. Hence, unlike the `HB` method, this void finder uses more than one sphere to "build" a void. Moreover, a percolation analysis is performed to define the void volumes, corresponding to topologically linked spheres, that satisfy an imposed density cut-off,

$\delta_g < 1/V(r_{cut-off}) - 1$, with V the volume of the sphere of the radius $r_{cut-off}$[1]. Figure 4.1 shows the positions of the maximal spheres in the two fields of the VIPERS sample, W1 and W4, projected along the RA-z plane. Micheletti et al. (2014) obtained 229 maximal spheres from the W1 field and 159 in the W4.

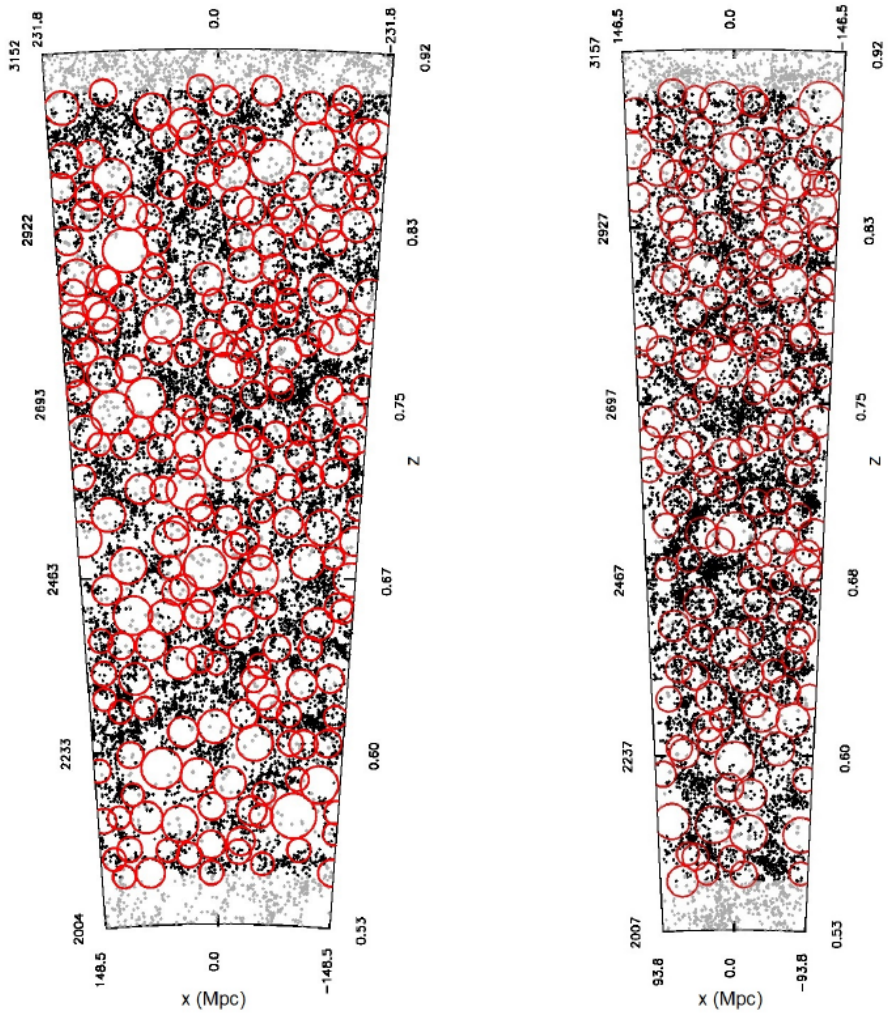

FIGURE 4.1 - Maximal spheres (2D-projected red circles) in the RA-z plane for the W1 (*left panel*) and W4 (*right panel*) fields. The black dots are the galaxies of the sample in the given z-range, while the grey dots are the galaxies detected as isolated, or outside the redshift range.
Credit: Micheletti et al. (2014).

[1]For further information about the trend in redshift of the cut-off radius, please refer to the subsection 5.4 of Micheletti et al. (2014).

4.2.3 THE COLBERG'S VOID FINDING ALGORITHM

The Colberg et al. (2005) algorithm searches for cosmic voids as regions having a mean overdensity equal to or less than -0.8. The choice of this value is essentially based on dynamical considerations (see Dubinski et al., 1993; Blumenthal et al., 1992). Similarly to what argued by Aikio and Mähönen (1998), voids are considered as cosmic depressions, generated by primordial negative overdensity fluctuations. During the cosmic evolution, perturbations grow and eventually reach the *shell-crossing* phase (see section 3.4). According to the Lavaux and Wandelt's classification, this method is based on a geometrical criterion.

4.2.3.1 METHOD

The method consists of four main steps. Firstly, the particle sample is binned into a 3D-grid. It has been demonstrated that the bin size has a negligible effect on void locations and sizes. Then, the grid is smoothed adaptively. This is a more convenient choice than, for instance, a Gaussian smoothing, that tends to delete small underdense regions. The third step consists in finding the local minima in the density distribution. Spheres of different dimensions are located at the centre of these minima. Finally, the underdense "ocean" that forms a big interconnected void (in which haloes are isolated regions, like "islands"), is divided into several smaller voids. These voids can be spherical, ellipsoidal, or of any other shapes. To avoid structures formed by low-density volumes connected with one another by filamentary tunnels, voids are grouped as follows. Any sphere totally located inside another one is removed from the final catalogue, while a sphere whose centre lies within a larger sphere is added to the latter. Instead, a sphere whose centre is located outside the boundary of another one is merged to the latter if the two spheres overlap. Morevorer, by connecting two sphere centres with a line, if the central segment within the intersection of both spheres is longer than one of the other two segments, the regions are merged.

4.2.3.2 RESULTS

Colberg et al. (2005) tested their method on four simulations: the ΛCDM GIF (Kauffmann et al., 1999), the ΛCDM GIF2 (Gao et al., 2004), the ΛCDM VLS (Ménard et al., 2003) and the Hubble Volume (Evrard et al., 2002). From the latter simulation, with an area of 10000 deg^2, they obtained about 80000 cosmic voids larger than 10 h^{-1}Mpc. In this

simulation, the largest void found has a radius of approximately 56 h^{-1}Mpc, that is rather similar in size to the Boötes supervoid (see section 3.3). Furthermore, they obtained that the *halo mass function* in voids is quite different from that in mean-density regions, according to what claimed by Gottlöber et al. (2003).

4.2.4 WVF - WATERSHED DFTE

The *watershed*-based void detection technique has been proposed by Platen et al. (2007). The `Watershed Void Finder` (`WVF`) is a geometrical algorithm based on the so-called *Delaunay Tessellation Field Estimator* (DFTE). This provides an optimal sensitivity to the structure morphologies. The `WVF` method does not need any *a priori* assumption on the size and shape of cosmic voids. This provides also the basis to analyse the evolving void hierarchy.

4.2.4.1 METHOD

The `WVF` consists of nine steps. Firstly, the DFTE transforms a point distribution (e.g., from N-body simulations or galaxy redshift surveys) into a continous density field. The DFTE technique (Schaap and van de Weygaert, 2000) is based on the *Voronoi* and *Delaunay tessellations* of a spatial point distribution. The *Delaunay tessellation* of a point sample is the volume-covering method of mutually Delaunay thetraedra, each of them defined by a 4-point set inscribed in a sphere that does not contain other points (Delaunay, 1934). The DFTE process ensures a density field which retains the morphological feature of the point distribution, that is the hierarchical nature. Then, the DFTE is sampled on a grid. The grid is built in such a way that its size guarantees the resolution of all structures, while minimising the number of used cells. The third step deals with the smoothing of the DFTE density field, via *natural neighbour* (NN) *maxmin* and *median filtering*. The minimum, median and maximum values of the density are computed within the adjacent Voronoi cells, that is the volume defined by a point and its natural neighbours. For any point, the *Delaunay triangulation* defines its NNs, that is all points are connected through that tessellation. As shown in Figure 4.2, the central Voronoi polyhedron is surrounded by its related Delaunay thetraedra (in 2D, triangles), defining the NNs of the central black dot. As visible, the Voronoi tesselation of the discrete point sample is the dual graph of the Delaunay triangulation.

Subsequently, the method transforms the image into a discrete set of density levels. These contour levels are identified by an uniform partitioning of the cumulative density

distribution. The next step consists in reducing occasional pixel-by-pixel fluctuations, by means of *opening* and *closing* operations of 2-pixel radius. For a detailed description about the mathematical morphology procedure of opening/closing, refer to the APPENDIX A of Platen et al. (2007).

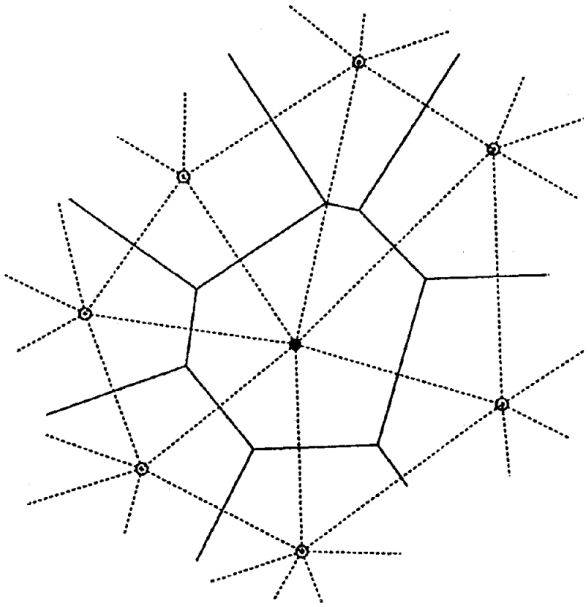

FIGURE 4.2 - The *natural neighbours* (open circles) of the black dot point. The solid lines mark the Voronoi cells around the dot, while the dashed edges represent the *Delaunay triangulation*.
Credit: Platen et al. (2007).

In order to identify the field minima, `WVF` looks for grid cells having neighbours with a higher density. The seventh step is the *flooding* procedure in which, starting from local minima, the flood level increases, until a given threshold is reached. During the raising, all the surrounding regions, that have a value of density lower than the threshold, are added to the basin of a starting minimum. Figure 4.3 shows three frames of the *watershed* procedure. From local density minima, the flood level starts to rise (*left panel*). Where two or more near basins meet up ridges, *dams* are erected (as visible in the top of the *central panel*). Finally, the entire landscape is immersed in the water (*right panel*) and the partitioning segments are well identified.

Once the flood level reaches a pixel shared by two different basins, it is considered as a part of the segmentation boundary. This process is iterated while the region has been segmented into a void. The final step of the method corrects possible effects due to the

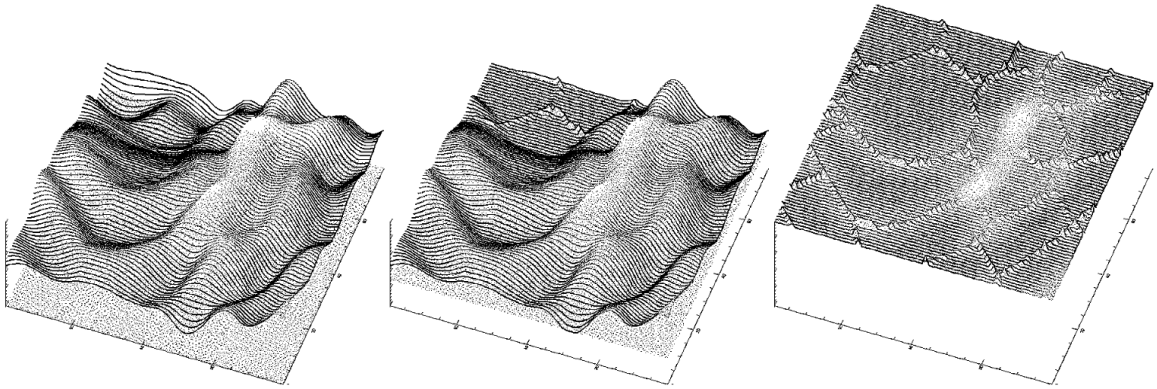

FIGURE 4.3 - Three frames of the *watershed transform*.
Left panel - The surface in the shape of a landscape before the rising of the "water" level.
Central panel - An intermediate stage of the watershed procedure, in which some basins are filled by the "water".
Right panel - The final result of the fully immersed landscape, which shows a division into cells separated by dams.
Credit: Platen et al. (2007).

hierarchical nature of voids. The subtraction of boundaries occurs where the density is lower than the threshold. Usually, this threshold is set to the typical void underdensity, $\delta = -0.8$.

A more accurate description of the nine steps of WVF can be found in section 3 of Platen et al. (2007), while for further information about tessellations, DFTE (theory and procedure) and other methods, please refer to van de Weygaert et al. (2009).

4.2.4.2 RESULTS

Platen et al. (2007) tested meticulously the WVF algorithm, by applying it to a kinematic Voronoi model (van de Weygaert and Icke, 1989), belonging to the class of Voronoi clustering models. The WVF method has turned out to be able to reproduce the qualitative cellular frame of the Voronoi models, and also to match $1-1$ cell sizes with the WVF segment volume, and so the relative void size distribution.

In the Aspen-Amsterdam project (see section 4.3) (AAp), by using a DM halo sample, Platen et al., obtained 167 voids, whereof the largest one is 14.3 h^{-1} Mpc in radius, and also a volume filling factor close to 1.

4.2.5 ZOBOV & VIDE

The ZOBOV (ZOnes Bordering On Voidness) algorithm is a parameter-free void finder based on a geometrical approach, presented by Neyrinck (2008) as an inversion of the previous VOBOZ (VOronoi BOund Zones) method (Neyrinck et al., 2005). The substantial difference between the two methods is that ZOBOV searches for low-density zones, while VOBOZ for density maxima.

4.2.5.1 THE ZOBOV METHOD

The first step of ZOBOV consists in computing the density value for each tracer, using the *Voronoi Tessellation Field Estimator* (VFTE) (Schaap, 2007). The *Voronoi Tessellation* (Voronoi, 1908) divides a given space into regions around each point, i, called *seed*. Any cell represents the region of space closer to i than to any other seed. This implies that the segments in the Voronoi plane are constitued by all the equidistant points between two nearest seeds. The density related to the i-th particle is given by the inverse of the volume of the Voronoi cell around it, $1/V(i)$.

The following step concerns the partitioning of the tracers into *zones* around each density minimum. This is to increase the computational speed, and it also allows to compress the datasets. A density minimum is defined as the position of a tracer having a value of density lower than any other Voronoi neighbours. By addressing particles to their most underdense neighbours, a minimum's *zone* is the particle set moving downward into it. Moreover, a minimum's *core* can be defined as the minimum-density particle into a given zone.

The following step consists in merging some zones into larger voids. ZOBOV exploits the *watershed* technique (see subsection 4.2.4). The "water level" in a zone, z, raised gradually, from the minimum in density. During the process, contiguous zones are joined together. The filling process ends when the water overflows into a deeper zone, or if the z region is the deepest nearby. Once a void is detected, its core is identified as the density minimum. The value of the density at which the water flows downward in a deeper region is labelled as the *linking density*, $\rho_l(z)$.

The algorithm provides in output a catalogue of void "candidates". Furthermore, the algorithm gives also the probability, $P(r)$, that each candidate is a "real" void. This probability is related to the proper density contrast and it is defined as the ratio between the minimum-density particle located on a ridge and the minimum density of that void, $r(v) = \rho_l(v)/\rho_{min}$. The density contrast is linked to $P(r)$, by making a comparison with a

Poisson particle distribution. Specifically, this probability quantifies the likelihood that a void with $r(v)$ could have emerged from Poisson noise. This *fakeness probability* is estimated as

$$P(r) = \exp\left(-5.12(r-1) - 0.8(r-1)^{2.8}\right), \tag{4.1}$$

where the factors are computed by fitting the cumulative probability function of voids with the Poisson distribution.

ZOBOV provides three different methods to define the void edges. The simplest one is to consider the raw ZOBOV outputs. They would consist of a large void, surrounded by subvoids, each of them with a proper significance level. This implies that a z zone is built by several voids and their substructures. A more accurate option is to specify a significance level for each subvoid. All subvoids that exceed this limit are removed. Finally, the third option exploits the void density contrasts to find a most-probable extent of voids. Further details about the definition of void edges are provided in the related article.

4.2.5.2 RESULTS

Neyrinck (2008) tested ZOBOV on a DM simulation, in a periodic cubic box with a side of 60 h^{-1} Mpc, extracted from the Millennium Run. Many of the obtained results were also compared in the Aspen-Amsterdam project. The adapted non-periodic version of ZOBOV, used in the AAp, detected on average about two order of magnitude more cosmic voids with respect to the other algorithms, because of the many low-significance detected structures.

ZOBOV has the virtue of being a free-parameter code. This implies that no constants have to be set for the run, although it is possible to set the value of the density threshold. Furthermore, this algorithm provides the full hierarchical distribution of voids, with *parent voids* and all their subvoids.

4.2.5.3 VIDE

Sutter et al. (2015b) proposed VIDE, the `Void IDentification and Exaination toolkit`, as an enhanced and extended version of ZOBOV. VIDE is an *open-source* Python/C++ void finder algorithm, able to extract a void catalogue from N-body simulations or galaxy redshift surveys, characterising their properties and providing a platform for a more detailed analysis. VIDE provides a *void hierarchy*, by using the identification of the various

basins and ridges. In this substructure-partitioning, shown in Figure 4.4, a parent void holds a multitude of subvoids. Each void derives from one parent and could have several *child subvoids*, subdivided into different levels.

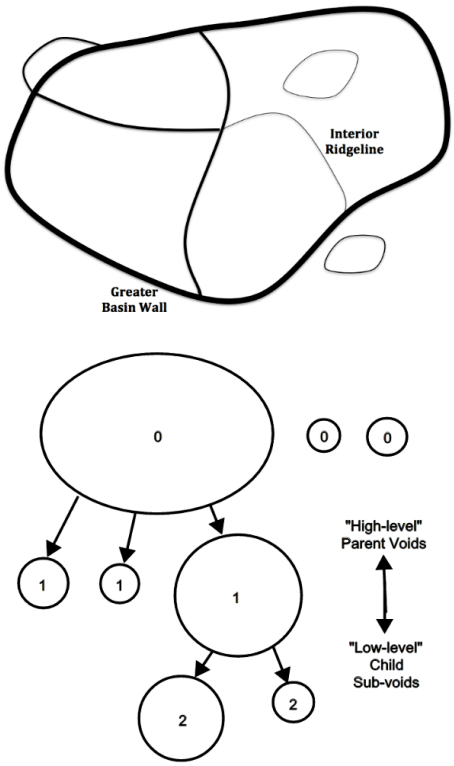

FIGURE 4.4 - A schematic diagram of void hierarchy.
Top panel - The ridgelines thickness is proportional to density.
Bottom panel - The tree levels of a parent void (identified with 0) with its subvoids (1) and subsubvoids (2).
Credit: Sutter et al. (2015b).

The VIDE performances have been improved as compared with ZOBOV, both in speed and robustness of the algorithm. Unlike ZOBOV, VIDE offers the possibility of working both with DM particles and haloes. It can also provides subsamples randomly extracted from the input catalogue.

The VIDE output includes the original ZOBOV void catalogue, plus various other *post-processed* quantities. Indeed, the resulting catalogue contains many useful properties related to each void: ID, centre coordinates, effective radius, density contrast, statistical relevance, etc, and also a set of additional information about the level of cosmic voids in the dependencies' tree. One of the most important quantities is the so-called *macrocenter*,

defined as

$$\mathbf{X}_v = \frac{\sum_i \mathbf{x}_i V_i}{\sum_i V_i}, \tag{4.2}$$

that represents the weighted volume centre, where $\mathbf{x}_i$ are the positions of each particle i and V_i its Voronoi volume. All the voids and subvoids found by the algorithm are stored in this output catalogue, without any restriction on the shape, on possible overlapping or on density.

VIDE also allows to make a direct comparison between two void catalogues, performing the overlapping of structures, to match voids from both the lists. Moreover, there is a Python application, API, useful to easily handle void catalogues, perform analysis and plot results.

4.2.6 DIVA

The first two classes of void detectors considered by Lavaux and Wandelt (2010) look for cosmic voids from Eulerian positions of tracers, as already mentioned in section 4.1. These approaches suffer from the sparse sampling of the objects in underdense regions used as mass tracers. In order to alleviate this problem, a third class of algorithms has been proposed. These methods detect cosmic voids using the Lagrangian displacement field. The Dynamical Void Analysis (DIVA) (Lavaux and Wandelt, 2010) algorithm is an example of this class.

4.2.6.1 Method

DIVA is based on the *Monge-Ampère-Kantorovitch* (MAK) reconstruction and the *Zel'dovich Approximation* (see subsubsection 2.6.4.1).

The MAK reconstruction provides a description of the back-in-time trajectories of galaxies in a completely non-linear regime. By assuming local mass conservation, the MAK theory[2] provides a reconstruction map, $\mathbf{q} \to \mathbf{x}(\mathbf{q})$, onto a grid, from the discretised equation:

$$S_\sigma = \sum_i (\mathbf{x}_i - \mathbf{q}_{\sigma(i)})^2, \tag{4.3}$$

where $\mathbf{q}$ is the comoving Lagrangian coordinate, $\mathbf{x}(\mathbf{q})$ is the Eulerian-Lagrangian change of variables and σ is the i-th perturbation of the particles. In order to minimise the equa-

[2] A more detailed description of the MAK reconstruction theory and its mathematical formalism are provided in section 2 of Lavaux and Wandelt (2010).

tion (4.3), Lavaux and Wandelt implemented a high-performance algorithm (parallelised by MPI[3]).

The authors redefined *ad hoc* the concept of void. DIVA considers a void as the region of maximum displacement of particles. By assuming the Lagrangian approach and the following Eulerian-Lagrangian linking map

$$\mathbf{x}(\mathbf{q}) = \mathbf{q} + \boldsymbol{\Psi}(\mathbf{q}), \tag{4.4}$$

where $\boldsymbol{\Psi}$ is the displacement field, they introduced the displacement field source, $S_{\boldsymbol{\Psi}}$, as follows:

$$S_{\boldsymbol{\Psi}}(\mathbf{q}) = \sum_{i=1}^{3} \frac{\partial \Psi_i}{\partial q_i}. \tag{4.5}$$

The $S_{\boldsymbol{\Psi}}$ maxima identify the centres of the *candidate void* (sometimes called the *protovoid*). Moreover, the types of voids can be defined from the eigenvalues of the *shear matrix*, $T_{l,m}$, of the displacement field. In particular, Lavaux and Wandelt called *true voids* the structures having $\lambda_1 > 0$, $\lambda_2 > 0$ and $\lambda_3 > 0$, *pancake voids* the ones with $\lambda_1 > 0$, $\lambda_2 > 0$, but $\lambda_3 < 0$, and the *filament voids* the ones with $\lambda_1 > 0$, $\lambda_2 < 0$ and $\lambda_3 < 0$ (Figure 4.5).

The reconstructed displacement field is then smoothed and the tidal matrix is computed. Subsequently, the algorithm calculates $S_{\boldsymbol{\Psi}}(\mathbf{x})$ on a grid, by summing the three eigenvalues (corresponding to what expressed by eq. (4.5)). Finally, the last step consists in computing the void boundaries and volume, through a modified *watershed transform*. In this version, cosmic voids are sources of maximum displacement for particles. Contrarily to the original watershed algorithm, DIVA enforces that $S_{\boldsymbol{\Psi}} > 0$ within void boundaries.

4.2.6.2 Results

Lavaux and Wandelt (2010) tested their void finder on N-body simulations in different cosmological models (i.e. ΛSIM/ΛSIM2 with $w = -1$ and wΛSIM with $w = -0.5$). They obtained very successful results with the MAK method. In particular, they set the mean ellipticity of cosmic voids with radii greater than 4 h^{-1}Mpc and with a precision of about 0.1% .

[3]The *Message Passage Interface* is a network protocol used to link different nodes of computer clusters, in order to parallelise the execution of a program (Gropp et al., 1996).

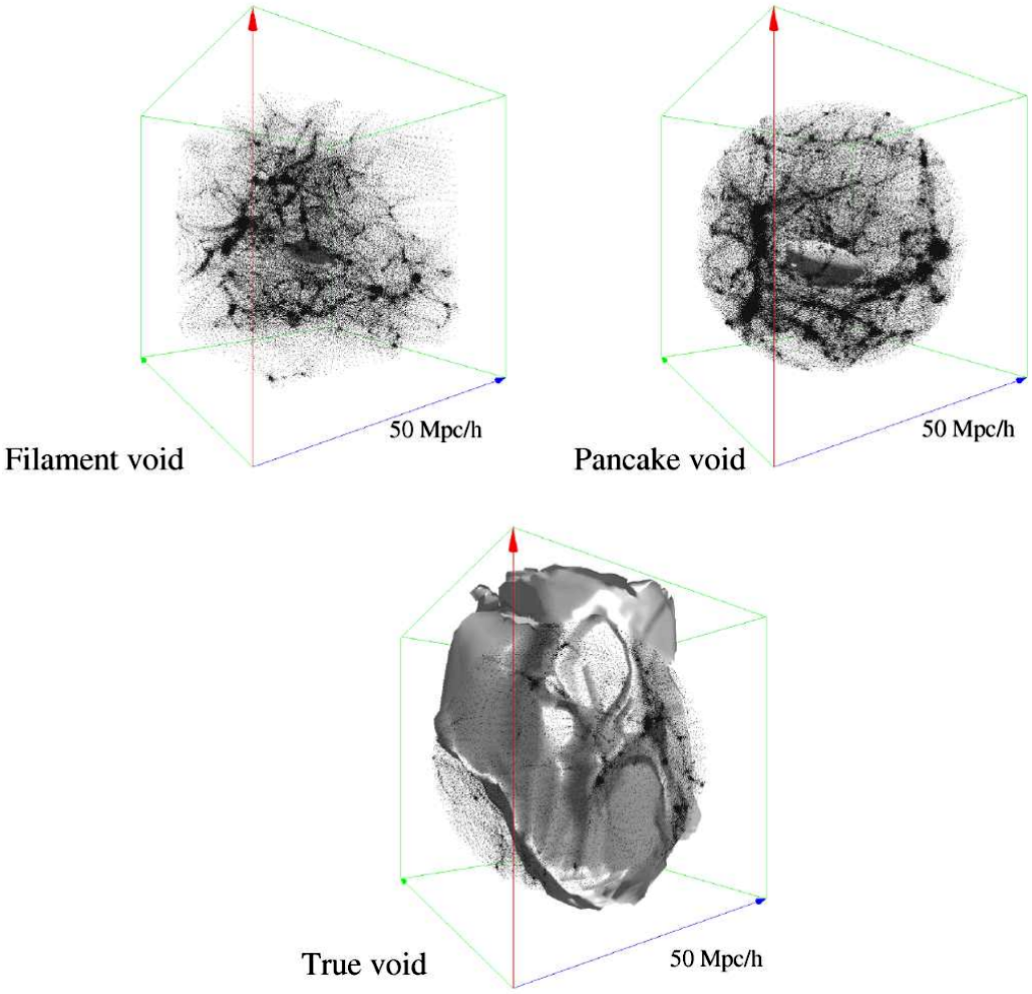

FIGURE 4.5 - The three classes of possible voids detected by the DIVA algorithm.
Credit: Lavaux and Wandelt (2010).

For more details about the MAK reconstruction, please refer to Brenier et al. (2003), while for the reconstruction method, the analytical models and the comparison with simulations, see Lavaux and Wandelt (2010).

4.2.7 UVF & LZVF ALGORITHMS

Elyiv et al. (2015) designed two dynamical Void Finder methods, the `Uncorrelating Void Finder` (`UVF`) and the `Lagrangian Zel'dovich Void Finder` (`LZVF`), belonging to the third class of Lavaux and Wandelt (2010). Both algorithms are able to reconstruct the Lagrangian positions of galaxies, by randomising the Eulerian ones.

4.2.7.1 METHOD

The UVF method relies on the measure of the 2PCF. At the present epoch, galaxies are inhomogeneously distributed, while an early Universe is characterised by almost no spatial correlation. In order to describe the back-in-time evolution of galaxies, UVF exploits the 2PCF. Specifically, tracers are randomly moved along straight lines. If the 2PCF amplitude has been reduced as a result of this displacement, the new position is stored. The process ends when an uncorrelated distribution of tracers has been reached.

The LZVF method aims to achieve a random distribution of particles, by exploiting the *Z*el'dovich Approximation. This method performs a reconstruction, similarly to that proposed by Croft and Gaztanaga (1997), in their PIZA algorithm. To find the tracer displacements, LZVF needs a homogeneous distribution to describe the initial particle positions. It assigns a final particle position to each tracer from the inhomogeneous sample. The displacement vector field is given by the spatial separations between the initial and the final positions of tracers. Specifically, all particles are randomly connected with one of the random distribution. The *total action* of the system is proportional to the sum of the amplitudes of the square displacement. As shown in Figure 4.6, after the pairing between the initial and final positions of particles, a *swapping* procedure is performed, to minimise the action, by interchanging the final points (*central panel*). If this change leads to a lower value of the total action, this configuration is kept.

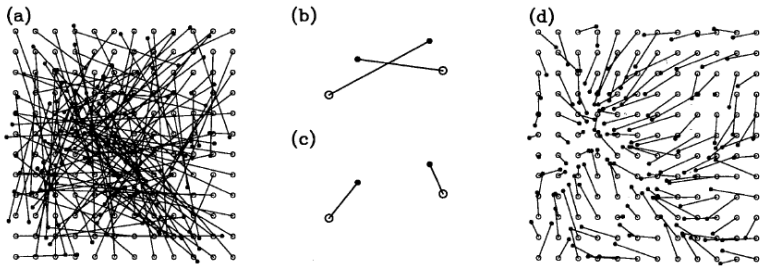

FIGURE 4.6 - A 2D slice of a particle distribution that shows the minimisation procedure of the total action, performed by PIZA and LZVF. Open circles are the initial particle positions, while black dots represent the final positions. The black lines represent the linking path between the two positions.
Panel (a) - The first random association between initial and final positions.
Panels (b) & (c) - The interchange procedure between two particle pairs. In this case, the interchange in (c) leads to a lower total action with respect to the (b) configuration.
Panel (d) - The final particle distribution with the lowest total action, representing a "cool" state of the system.
Credit: Croft and Gaztanaga (1997).

After the reconstruction of the Lagrangian positions, the displacement field of tracers is obtained by connecting their positions to the Eulerian coordinates. A measure of the velocity divergence provides information about the density. Negative values of the velocity divergence identify cosmic voids, as sinks of the back-in-time path of mass tracers. By performing a *watershed* process, local density minima are found, each of which will identify a subvoid. Then, subvoids are merged together in a hierarchical void-tree scenario to form cosmic voids. The final void catalogue provides the comoving coordinates of the void centres, found as the position of the minimum divergence field inside a given void, and the related effective radii.

4.2.7.2 RESULTS

By testing both methods on a $z = 0$ halo catalogue extracted from the CoDECS simulations (Baldi, 2012)[4], Elyiv et al. (2015) found almost the same number of subvoids (427 with UVF, 433 with LZVF), also obtaining quite similar features in the related reconstructed divergence fields. Furthermore, they made a comparison with the ZOBOV method. The overdensity profiles provided by UVF and LZVF show more self-similar shapes with respect to the ZOBOV ones. In particular, their stacked density profiles appear quite smooth, showing a negligible compensation in correspondence of void boundary, contrary to ZOBOV.

4.3 THE ASPEN-AMSTERDAM PROJECT

As discussed in the previous sections, the growing interest in exploiting voids as cosmological probes led scientists to implement a large number of different void finder algorithms. To compare the results of the main algorithms proposed, Colberg et al. 2008 presented a systematic analysis of different Void Finders (13 in total) using a $z = 0$ galaxy mock catalogue, extracted from the Millennium Simulation (Springel et al., 2005) with a semi-analytical galaxy formation model (Croton et al., 2006). Specifically, from a ΛCDM cosmological simulation, containing 2160^3 DM particles[5], in a periodic box of 500 h^{-1}Mpc in side, it has been extracted a subsample composed by ≈ 12.5 billion of particles, in a volume whose density contrast is $\delta = 0.28$. Finally, they considered a

[4]Specifically, Elyiv et al. (2015) used the H-CoDECS, a hydrodynamical N-body simulation with a side of 80 h^{-1}Mpc and a number of particles equal to $N_p = 2 \times 512^3$.

[5]The initial conditions have been obtained by setting $\Omega_m = 0.25$, $\Omega_\Lambda = 0.75$, $h = 0.73$ and σ_8=0.9. This implies that the particle mass is $8.6 \times 10^8\ h^{-1}\mathrm{M}_\odot$.

subsample of 17604 galaxies and 4006 DM haloes, the latter having masses greater than $10^{11}\,h^{-1}\mathrm{M}_{\odot}$.

The goal of this project was not to find the best void finder or the best method, but rather to understand the main differences between the adopted approaches. The participants have been required to use proper code on the above-mentioned catalogues and to provide an output void sample.

4.3.1 THE COMPARISON

As outlined in table 2 of Colberg et al. (2008), the number of voids detected by the considered algorithms, and relative properties, are largely different. This is mainly due to different assumptions on how to define a cosmic void. Indeed, from the same input catalogue, the number of voids varies from 3 (for the algorithms of Brunino et al. 2007 and Foster and Nelson 2009) to 167 (for the method of Platen et al. 2007). Moreover, the radius of the largest void spreads over a range between 10 h^{-1}Mpc (for the algorithm of Plionis and Basilakos 2002) and 29.9 h^{-1}Mpc (for the void finder of Colberg et al. 2005).

As a result of this comparison, it has been shown that both the shapes and sizes of voids, as computed by different methods, can be significantly different. This problem is also enhanced by the choice of *ad hoc* parameters in many of the proposed algorithms.

The 15 panels of Figure 4.7 show a slice with a thickness of 5 h^{-1}Mpc of the central region of the sample considered. The *top-left panel* shows the DM distribution, while the *top-central panel* contains also the galaxies, overplotted to the DM distribution. The subsequent panels illustrate the largest void (the green area), with its centre (red dot), found by the thirteen groups, and those galaxies included within all voids. As easily visible, there are significant differences between the void properties detected by the different groups, as a consequence of the wide variety of employed methods. The different algorithms result in a wide spread in basics numbers and on their appearances.

This was the first project aimed at comparing different void finders based on various selection criteria and methods. As reported in the paper, *void sizes depend quite strongly on how voids are found, so one has to be very careful about using void sizes to make statements about the large-scale structure*.

For all considerations and comments about basic numbers, void density profiles, detected void galaxies and much more, please refer to Colberg et al. 2008.

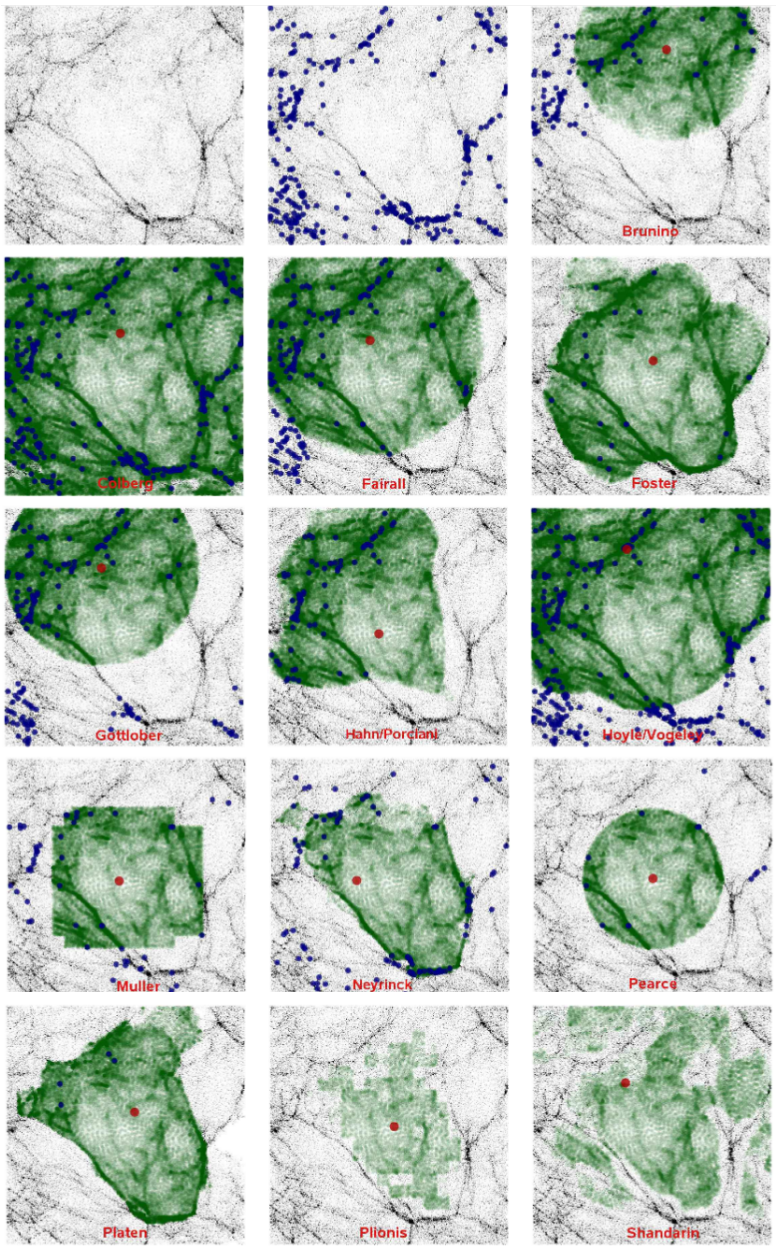

FIGURE 4.7 - A slice of 5 h^{-1}Mpc thick extracted from the Millennium Simulation. The picture illustrates the DM distribution in the central region of 40 h^{-1}Mpc (*top-left panel*). Void galaxies (blue dots) are overplotted on the DM distribution (*top-central panel*). The other 13 panels show the largest cosmic voids (green areas), with their centres (red dots), found by (in order, from top to bottom and from left to right) *Brunino, Colberg, Fairall, Foster, Gottlöber, Hahn & Porciani, Hoyley & Vogeley, Müller, Neyrinck, Pearce, Platen & van de Weygaert, Plionis & Basilakos and Shandarin & Feldman*. It can be noticed that the last two Void Finders found no void galaxies.
Credit: Colberg et al. (2008).

CHAPTER 5

A New Void Finder

Similarly to the DIVA algorithm, Elyiv et al. (2015) developed a Void Finder based on a dynamical criterion. Following a similar approach, we implemented a new Cosmic Void Finder algorithm, that is the main focus of this thesis. First, we present the CosmoBolognaLib, a large set of numerical libraries, in which we included our new Void Finder as an extension of the existing software (Marulli et al., 2016) (section 5.1). Then, in section 5.2, we describe the structure of our Void Finder. Finally, we illustrate in more detail the procedure adopted in the three main steps of the algorithm: the reconstruction of the displacement field (section 5.3), the measurement of the divergence field (section 5.4), and the identification of cosmic voids (section 5.5).

5.1 The CosmoBolognaLib

Our Void Finder has been implemented inside the CosmoBolognaLib (hereafter, CBL) (Marulli et al., 2016), a large set of open source C++/Python libraries for cosmological computing. CBL is a *living project* aimed at defining a common numerical environment for cosmological investigations of the large-scale structure of the Universe. In particular, this suite allows to handle astronomical catalogues, both simulated and observed, to make cosmological analyses, to perform statistical measures in configuration space, to extract cosmological constraints and much more.

The wide set of provided functions are easily usable, thanks mainly to the adopted *object-oriented* programming technique. This makes the CBL quite flexible to be used

for many different computations as, for instance, handling astrophysical catalogues of different sources, such as galaxies, AGN, clusters, DM haloes and, of course, cosmic voids.

Among many other things, the CBL environment can be used to measure the *two-point* and *three-point correlation functions*, to model *redshift-space distortions* and *baryon acoustic oscillations*, in both Standard and alternative cosmologies. Recently, new algorithms to predict the number counts of cosmic voids have been added (Ronconi and Marulli, 2017; Ronconi et al., 2017, in preparation). Our new void finder takes part in this living project.

CBL and its related doxygen documentation are available at `https://github.com/federicomarulli/CosmoBolognaLib`. Several examples are also provided in order to explain how to use the main internal classes and functions.

5.2 THE VOID FINDER ALGORITHM

With the aim of extending and improving the Void Finder algorithm proposed by Elyiv et al. (2015), we have implemented a new algorithm.

The new proposed Void Finder can be divided into three basic parts. The first step is employed to reconstruct *dynamically* the displacement field of cosmic tracers. This stage can be performed with two different algorithms: the former, called `LaZeVo`, the `Lagrangian Zel'dovich approximation for Void finder algorithm`, exploits the *Zel'dovich Approximation* in order to reproduce the back-in-time evolution of tracers located in voids and around them; while the latter, called `RIVA`, the `Random-Induced walk for Void finder Algorithm`, relies on the measure of the 2PCF to relax the distribution of objects to a homogeneous configuration.

The second step consists in performing several reconstructions of the density field, that are then averaged by using a Gaussian filter. By implementing the *watershed* technique, the code finds the local density minima, corresponding to the sources of maximum displacement, similarly to what done by the `DIVA` algorithm. The *watershed* allows also to find subvoids and to merge them under suitable conditions.

Finally, once all subvoids are identified, the algorithm provides a catalogue of cosmic voids, with their centres and dimensions. Figure 5.1 is a flux diagram describing the main execution steps of our Void Finder. The new Void Finder has been included in the CBL, extending the existing software to find cosmic voids from an input catalogue of extragalactic sources. Specifically, we introduced a new specific method of the C++ class `Catalogue`, implemented in VoidCatalogue.cpp.

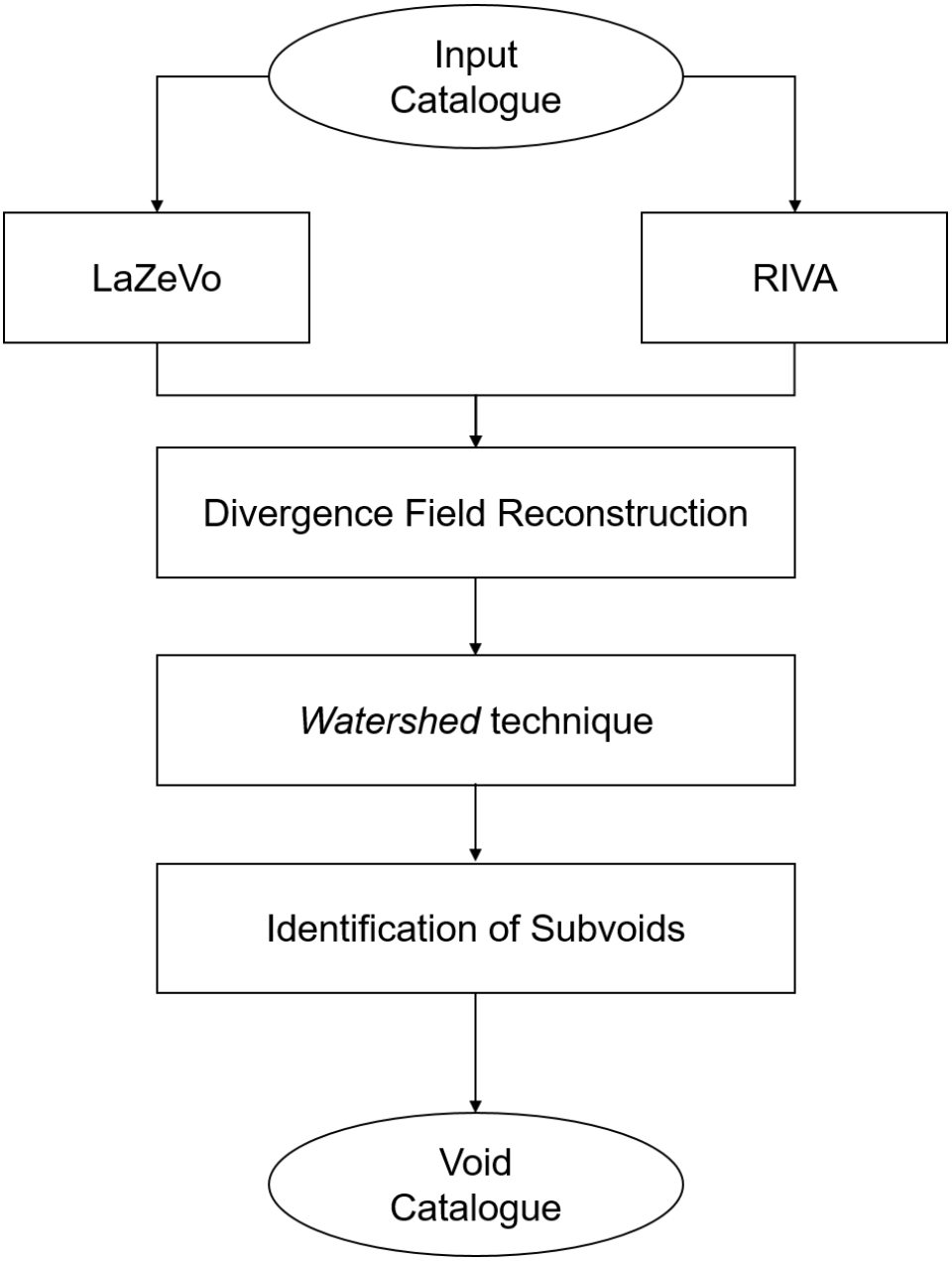

FIGURE 5.1 - A flux diagram showing the main steps of this Void Finder algorithm.

In the following, we provide the list of all parameters of the method:

- ◇ the `VoidAlgorithm` parameter – the specific method used to reconstruct the displacement field, i.e. either `LaZeVo` or `RIVA`;
- ◇ the `input` catalogue – the provided input catalogue of cosmic tracers used for the reconstruction of the displacement field;
- ◇ the `random` catalogue – an external random catalogue used by the `LaZeVo` method;
- ◇ the `dilution` parameter – a dilution factor possibly used to extract a subsample from the input catalogue;
- ◇ the `n_rec` parameter – number of reconstructions to be performed by the algorithm;
- ◇ the `mode` parameter – it specifies if *periodic* or *non-periodic* conditions should be used to measure distances;
- ◇ the `output` directory – path of the output directory where to store the `n_rec`-reconstructions, the divergence field, the subvoid and void catalogues;
- ◇ the `rmax` parameter – maximum radius used by the `ChainMesh` method (see subsection 5.3.2);
- ◇ the `cell_size` parameter – cell dimension of the grid used by `ChainMesh` method;
- ◇ the `shuffle_index` – the number of iterations performed by the `shuffle` function of the `LaZeVo` method (see subsection 5.3.2);
- ◇ the `iteration_index` – the number of iterations performed in order to obtain a flat-shape 2PCF in the `RIVA` method (see subsection 5.3.3).

5.3 THE DISPLACEMENT FIELD RECONSTRUCTION

Both the `LaZeVo` and `RIVA` methods aim at reconstructing initial galaxies' Lagrangian positions by randomising the Eulerian coordinates. As we will show in detail, a random distribution is used to obtain a displacement field, that approximates the velocity field of cosmic structures. Cosmic voids are considered as *sinks* in the reverse streamlines of galaxies (Elyiv et al., 2015).

5.3.1 THE THEORETICAL BACKGROUND

This Void Finder is based on sample randomisation, in order to reproduce an early homogeneous and isotropic distribution of objects in the pristine Universe. Objects are used as *test particles*, not mass tracers, to trace back in time their straight orbits, by minimising the action of the system. Once the Lagrangian positions $\mathbf{q}$ are reconstructed (see subsection 5.3.2 and subsection 5.3.3, for details), we derive the displacement field, $\mathbf{\Psi}$, linking them to the Eulerian coordinates, $\mathbf{v}$. So, by assuming straight trajectories in the displacement field, we obtain

$$\mathbf{\Psi}(\mathbf{q}) = \mathbf{q} - \mathbf{v}. \tag{5.1}$$

By definition, the divergence of the reconstructed field, $\mathbf{\Theta}$, is the density of sources or sinks of the mass distribution

$$\mathbf{\Theta} = \nabla \cdot \mathbf{\Psi} = \sum_{i=1}^{3} \frac{\partial \Psi_i}{\partial x_i}, \tag{5.2}$$

where x_i is the i-th Cartesian coordinates.

5.3.2 THE LAZEVO RECONSTRUCTION ALGORITHM

One of the two methods, implemented in this Void Finder for the reconstruction of the density field, is `LaZeVo`, based on the *Zel'dovich approximation* (subsubsection 2.6.4.1). Particles are supposed to move along straight orbits during their "backwards" evolution. `LaZeVo` thus connects their actual positions to the ones of a random distribution, representing an early Universe scenario.

5.3.2.1 THE ALGORITHM

The `LaZeVo` algorithm is subdivided in two main substeps. The first part handles the random distribution. If an external random sample is provided, a specific implementation of the `Catalogue` constructor[1] will read it[2]. Otherwise, a random catalogue is created.

The second substep deals with the search of closest pairs of objects between the input and random catalogues. This search is carried out thanks to the *chain-mesh* technique.

[1] A class constructor is a special member function of a C++ class. Constructors are very useful for setting initial values for certain member variables, as expressed in section 5.2.

[2] The random file must have the same number of objects or a multiple of the input catalogue ones. In the latter case, the random sample will be divided into n parts and then the reconstruction will be performed n times.

This method allows to count pairs, in a certain range of scales, in an efficient and fast way, by performing a *pixelization* scheme (similar to Alonso, 2012). The `ChainMesh` algorithm divides the considered volume into cubic cells. The indexes of objects are stored in *linked-list* vectors in each cell. Subsequently, in order to find only those random objects that are close to one object of the input catalogue, the search is done on cells inside a selected region, specified by `r_max`, as shown in Figure 5.2. This allows to reduce the number of unused counts of object pairs.

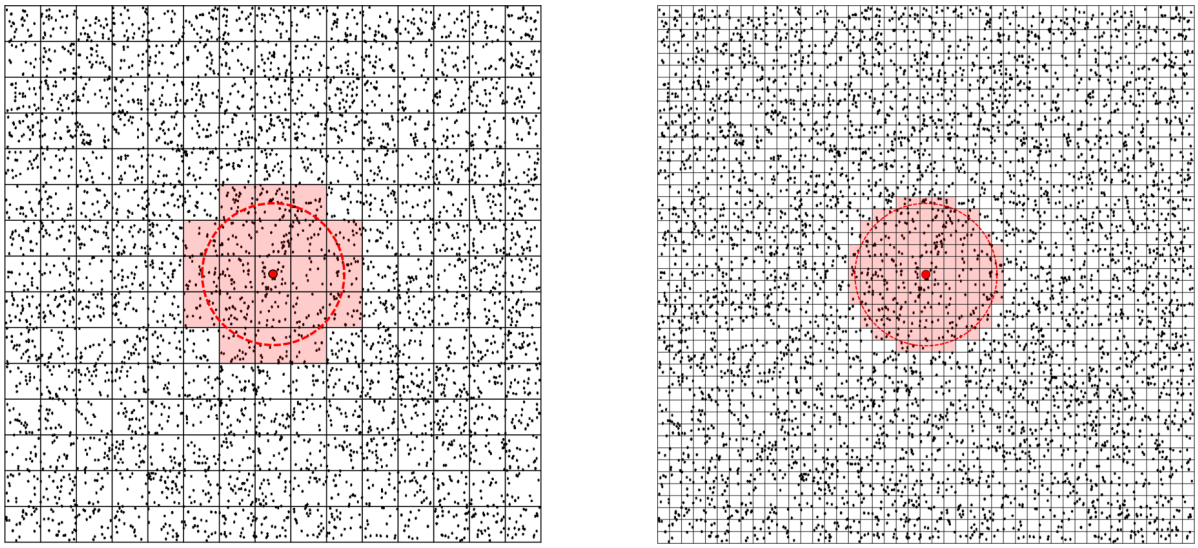

FIGURE 5.2 - A schematic picture of the *chain-mesh* technique for two different `cell_size` values. For a given point (the red dot), `ChainMesh` looks for closest objects within the region (marked by the red dashed circle) having `r_max` radius.

The efficiency of the algorithm depends on the ratio between the scale of the searching region and the maximum separation between the objects.

After sorting the distances between the i-th object and the close random ones within the searching radius, `rmax`, the *object-random* couple is identified, by choosing the shorter distance. This process is performed for all the objects of the input catalogue.

It may happen that the i-th object has no random objects within the given searching regions. In order to minimise the number of *unpaired* objects, several iterations are performed, for each reconstruction. Hence, with the aim of obtaining the best configuration with the lowest number of unpaired objects per reconstruction, `LaZeVo` performs an *index shuffling*, starting the research from a different object at each iteration. Hence,

the configuration having the minor unpaired objects is kept. As shown in Figure 5.3, the first configuration (*left panel*) allowed to pair just two particles of the input catalogue (1 – 2). Instead, by performing the *index shuffling*, the new configuration (*right panel*) "paired" all the input objects. The problem of unpairing is also mitigated by realising more reconstructions.

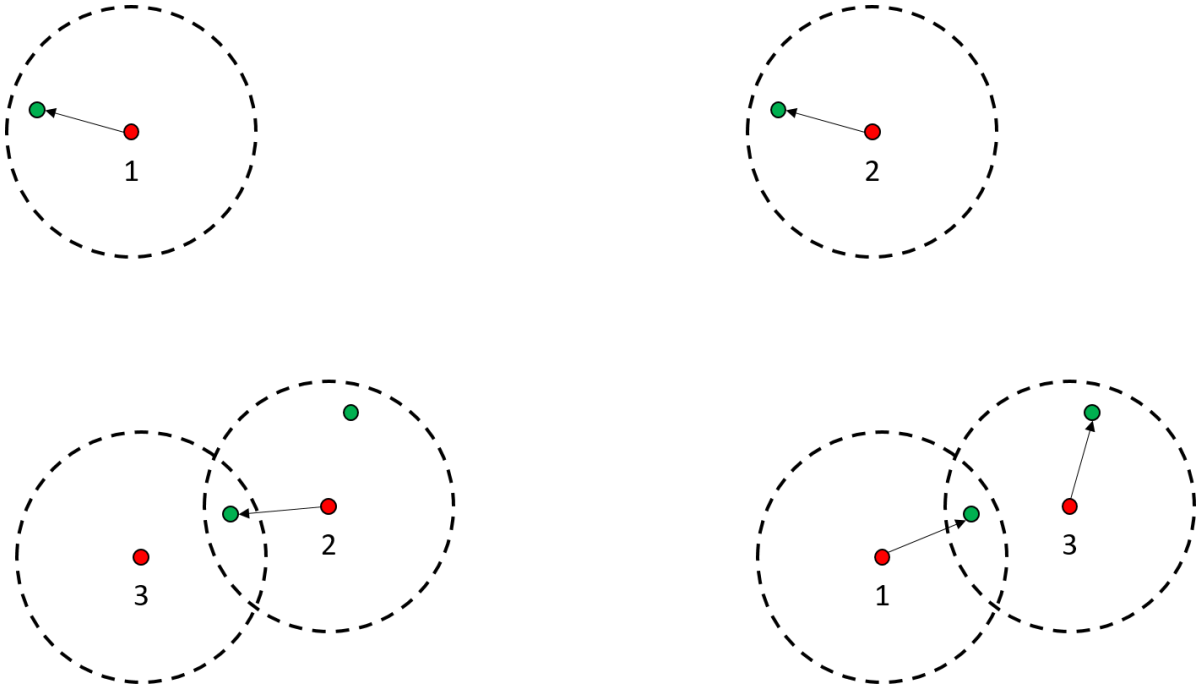

FIGURE 5.3 - A schematic picture of the research of closest pairs.
Left panel - A first configuration in which the 3^{rd} object is unpaired.
Right panel - A second configuration in which the index shuffling has allowed to pair all objects.

5.3.3 THE RIVA RECONSTRUCTION ALGORITHM

The second method considered to reconstruct the displacement field is `RIVA`. As already discussed, the Universe is currently characterised by an inhomogeneous distribution of extragalactic objects, the so-called *Cosmic Web*, as predicted by simulations and confirmed by galaxy redshift surveys. The spatial properties of cosmic structures can be quantified by the 2PCF (subsection 2.6.3, eq. (2.91)), that provides the excess in probability of finding object pairs with respect to a Poisson distribution. The matter distribution in the early Universe was approximately homogeneous and isotropic, thus

the 2PCF of matter was approximately null at all scales. So, a possible way to trace the orbits of extragalactic sources back in time is to "relax" the current matter distribution to reach the homogeneity, as explained in the following section.

5.3.3.1 THE ALGORITHM

The RIVA method consists in moving each object in a random direction and each time to measure the 2PCF. If the amplitude of the 2PCF decreases, as a result of the random movement of the object, the new configuration is kept. Otherwise, the previous distribution is restored. The procedure is repeated for all objects (more than once, if necessary) until the 2PCF is consistent with zero, within the uncertainties at all separations. Specifically, RIVA provides an estimate of the *reduced chi-squared*, $\tilde{\chi}^2$, between $\xi(r)$ and 0 at each time, and stops the procedure when $\tilde{\chi}^2 \simeq 1$.

The inclusion of the RIVA algorithm is still in progress. A previous version has been already presented in (Elyiv et al., 2015).

5.4 THE RECONSTRUCTION OF DIVERGENCE FIELD

Both the LaZeVo and RIVA methods can be used to compute the displacement field $\mathbf{\Psi}$, that links the Eulerian positions of objects to the Lagrangian ones. To take into account the shot noise uncertainties in the random field, the algorithm performs several reconstructions, each one obtained with a different initial *random seed*. All the reconstructed displacement fields are then averaged, at each position $\mathbf{q}$, by using a *Gaussian weighting*:

$$\langle \mathbf{\Psi}(\mathbf{q}) \rangle = \sum_j \Psi_j \cdot \exp(-d_j^2/2\sigma^2) / \sum_j \exp(-d_j^2/2\sigma^2), \tag{5.3}$$

where the subscript j identifies the reconstructed position at each iteration, d_j is the distance between the j-th object and the positions $\mathbf{q}$, and σ is a *Gaussian smoothing*, corresponding to the *mean interparticle distance*, necessary to generate a continuous vector field. Finally, the algorithm computes the divergence field that represents, by definition, the density at each point (eq. (5.2)).

In order to identify the *subvoids*, the algorithm searches for all the grid cells with a negative value of divergence. Each local minimum will define a subvoid. In fact, a negative value of the velocity field divergence implies the presence of a region acting as a *sink* of mass streamlines.

5.5 THE IDENTIFICATION OF COSMIC VOIDS

As discussed in the previous sections, the adimensional quantity Θ is used to identify subvoids and, then, voids in corrispondence of local minima of the divergence field. Specifically, a local minimum is a *grid node*, where the value of Θ is lower than in the adjacent $3^3 - 1$ nodes (as shown in Figure 5.4).

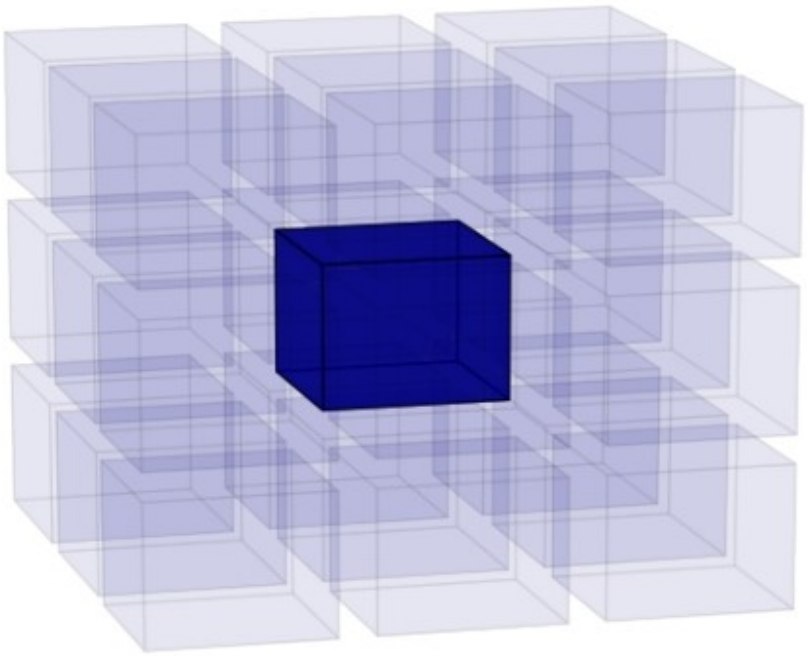

FIGURE 5.4 - A schematic picture of a grid node having a divergence value lower than the $3^3 - 1$ cube cells around it.

The algorithm takes into account only the local minima with a negative value of Θ. Through the *watershed* technique (see subsection 4.2.4), the near subvoids are then "filled" in order to identify, eventually, a local void. Specifically, starting from local minima, the *basins* are filled. As visible in Figure 5.5, if the increasing level reaches a local maximum which divides two adjacent subvoids, these buckets are not merged, but rather a *dam* is erected between them.

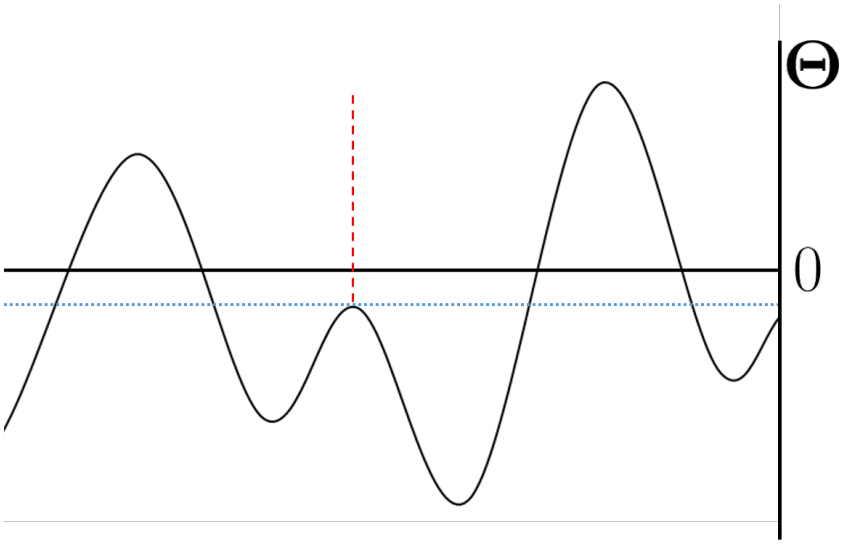

FIGURE 5.5 - A schematic picture of the divergence field. The wavy black line illustrates a fictitious divergence field, having both *ridges* (with $\Theta > 0$) and *basins* (with $\Theta < 0$). The thick horizontal black line separates regions with positive and negative values of divergence, respectively. The dotted horizontal blue line represents the "water" level that has reached a local maximum (but in a negative divergence region). In correspondence of this local maximum, a *dam* (dashed vertical red line) is erected in order not to join the two adjacent subvoids.

Subvoids close to the boundaries of the sample are rejected, to avoid an uncorrected estimate of the volumes. To provide a measure of the dimension of subvoids and, then, of voids, the *effective radius* is computed, as the radius of a sphere having the same volume of the considered structure:

$$R_{eff} = \left(\frac{3V_{void}}{4\pi}\right)^{1/3}, \tag{5.4}$$

where V_{void} is the volume of a given void.

In order to build up a void, a procedure based on joining contiguous subvoids has been adopted. After a sorting based on effective radius, voids are ordered from the largest to the smallest one. All voids with a R_{eff} value greater than a given R_{lim} are kept, while voids with a radius smaller than R_{lim}, and with no adjacent other voids, are removed. If a void, with an effective radius lower than R_{lim}, is close to one or more other voids, it is annexed to the largest one. This case implies a new estimation of the effective radius of the merged void, that will be the effective radius of the entire volume.

5.5.1 THE VOID CENTRE

Regarding void centres, many alternative definitions have been provided in the literature. In order to find the best definition of a void centre, Elyiv et al. (2015) compared four different definitions.

The simplest way to define the centre of a void is to consider the position of its *geometrical centre*:

$$\mathbf{r}_G = \frac{\sum_{i=1}^{n} r_i}{n}, \tag{5.5}$$

where r_i are the coordinates of the n grid nodes within a void. In the case in which a void has a constant density, the geometrical centre coincides with the *mass centre*.

An alternative definition is the *barycentre* of the objects hosted within a void:

$$\mathbf{r}_B = \frac{\sum_{i=1}^{n} v_i}{n}, \tag{5.6}$$

in which v_i is the i-th object position and n the number of objects.

Another definition is the *weighted centre* over the divergence field:

$$\mathbf{r}_W = \frac{\sum_{i=1}^{n} \Theta_i(r_i) r_i}{\sum_{i=1}^{n} \Theta_i(r_i)}, \tag{5.7}$$

where r_i represents the i-th coordinate of a grid node inside a void and n the total number of nodes.

Finally, the last definition considered is the *absolute minimum* value of the divergence field within a void:

$$\mathbf{r}_M = \min(\nabla \cdot \mathbf{v})_{void}\,. \tag{5.8}$$

As argued in Elyiv et al. (2015), who analysed the *divergence profiles* and their 1σ *standard deviations* (Figure 5.6), by using the four definitions, the best description of the central regions of detected voids has been provided by using the M centring. For this reason, we also decided to adopt this definition to compute the void centres of our catalogue.

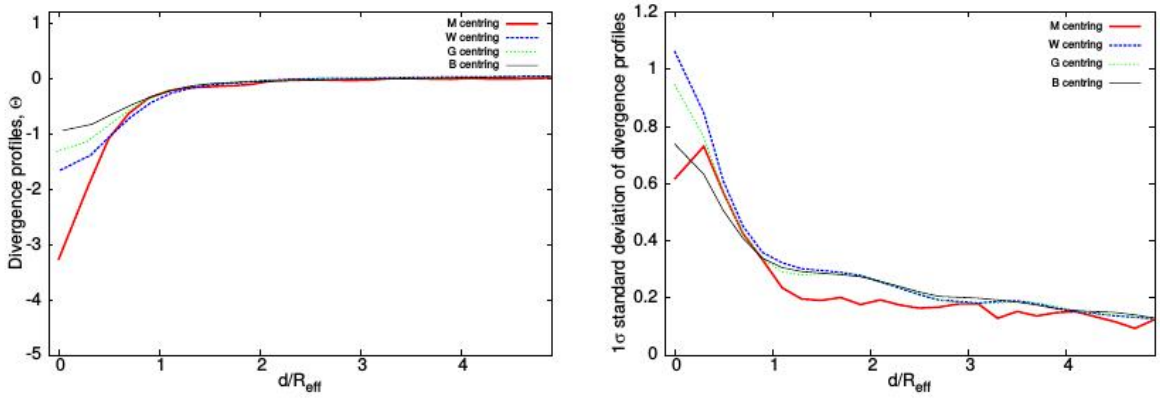

FIGURE 5.6 - The mean divergence profiles (*left panel*) with their 1σ standard deviations (*right panel*) of found voids as a function of fraction of effective radius, d/R_{eff}. The four profiles were obtained by assuming the four definitions of void centres: the *geometrical centre*, $\mathbf{r}_G$, the *barycentre*, $\mathbf{r}_B$, the *divergence-weighted centre*, $\mathbf{r}_W$ and the *minimum-divergence centre*, $\mathbf{r}_M$.
Credit: Elyiv et al. (2015).

CHAPTER 6

TESTING THE NEW VOID FINDER ON N-BODY SIMULATIONS

In this chapter we present the main results obtained by applying our new Void Finder on a $z = 0$ DM halo catalogue. We have obtained the final void catalogue by using `LaZeVo` as the displacement-reconstructor method. In section 6.1, we illustrate how the input parameters of our Void Finder have been set. In section 6.2, we describe the obtained maps of the reconstructed displacement field (see section 5.3) and their divergence field (see section 5.4). In section 6.3, we show the main properties of the final catalogue of voids obtained by the algorithm, in particular the void distribution and the positions of void centres. In section 6.4, we discuss the procedure adopted to obtain the stacked density profiles of the cosmic voids detected. The section 6.5 outlines the results obtained by the comparison between our new Void Finder and the `LZVF` proposed by Elyiv et al. (2015). Finally, in section 6.6, we present a first application of our Void Finder in the context of a challenge promoted inside the Euclid consortium.

6.1 SETTING THE INITIAL PARAMETERS

To test our Void Finder algorithm, we apply it to a $z = 0$ catalogue composed by 62497 DM haloes, in a box of 250 h^{-1} Mpc in side, extracted from a ΛCDM N-body simulation. To obtain the results shown in the following sections, we set the Void Finder parameters as follows:

- ◇ we consider the entire sample with no dilution;
- ◇ we averaged over 10 reconstructions of the displacement field;
- ◇ we did not consider *periodic* boundary conditions;
- ◇ the searching radius of the *chain-mesh* method has been set to 15 h^{-1}Mpc;
- ◇ the cell size of the *chain-mesh* method has been set to 0.1 times of the searching radius;
- ◇ the index shuffling has been performed 10 times per reconstruction.

6.2 THE DISPLACEMENT FIELD MAPS

In section 5.3, we have described the procedures adopted to reconstruct the displacement field, while in section 5.4 we have discussed how to estimate the divergence field. Figure 6.1 shows a slice of thickness 50 h^{-1}Mpc across our test box. The coloured map represents the velocity divergence field. Specifically, the reddest regions are those having the highest density values. Indeed, a large number of tracers (purple dots) are located in correspondence of these red areas. On the contrary, the blue areas correspond to the low-density regions, possible sites where to find the cosmic voids.

The reconstructed displacement field, $\mathbf{\Psi}$, has been overplotted on the divergence map in order to show the tracer flows (black arrows) from the high-density regions to the low-density ones, in this back-in-time evolution. Specifically, for clarity reasons, the displacement shown uses a 20×20 grid and each arrow represents the average outflow from each cell.

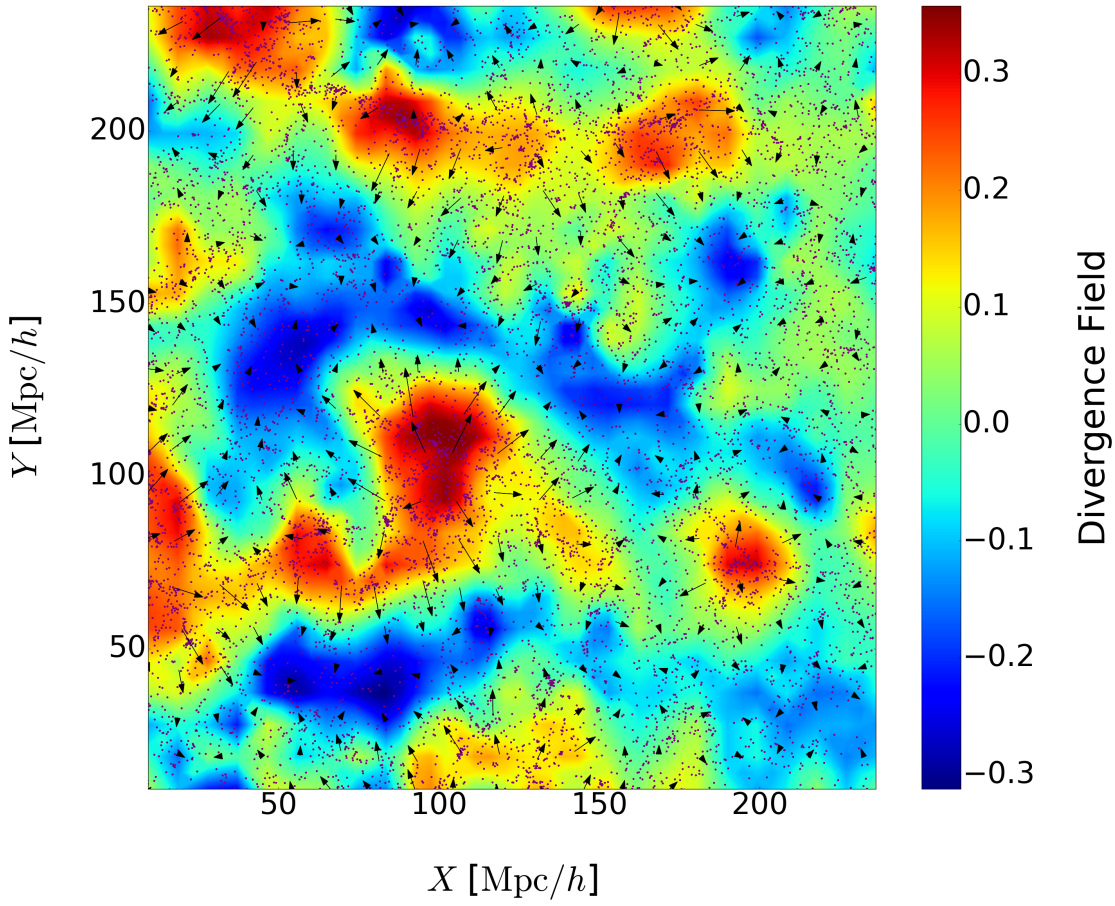

FIGURE 6.1 - The reconstructed displacement field, $\mathbf{\Psi}$, (black arrows) overplotted on its divergence field, $\mathbf{\Theta}$ (coloured map). The area of the displayed region is $(250\,h^{-1}\mathrm{Mpc})^2$, with a depth along the Z-axis covers the range $0-50\ h^{-1}\mathrm{Mpc}$.

6.3 THE VOID CATALOGUE

Our Void Finder detected 47 cosmic voids from the DM halo sample, having effective radii greater than $R_{lim} = 13\ h^{-1}$Mpc. Figure 6.2 shows the cumulative distribution of the detected cosmic voids as a function of the effective radius R_{eff}.

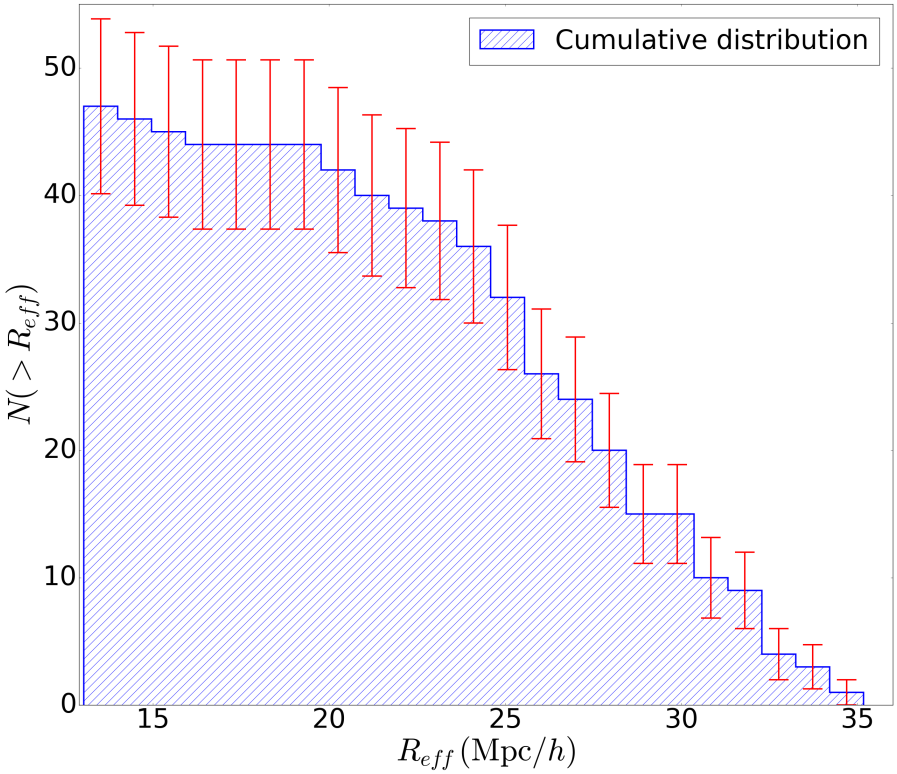

FIGURE 6.2 - The cumulative distribution of voids as a function of effective radius. The red error bars are the Poisson errors.

As expected, we found a good correlation between the effective radii of the detected voids and the corresponding minimum value of the divergence (corresponding to the centre of a void). Specifically, the larger the effective radius, the lower the minimum divergence, as shown in Figure 6.3. This result is in agreement with previous findings (e.g. Elyiv et al. (2015)).

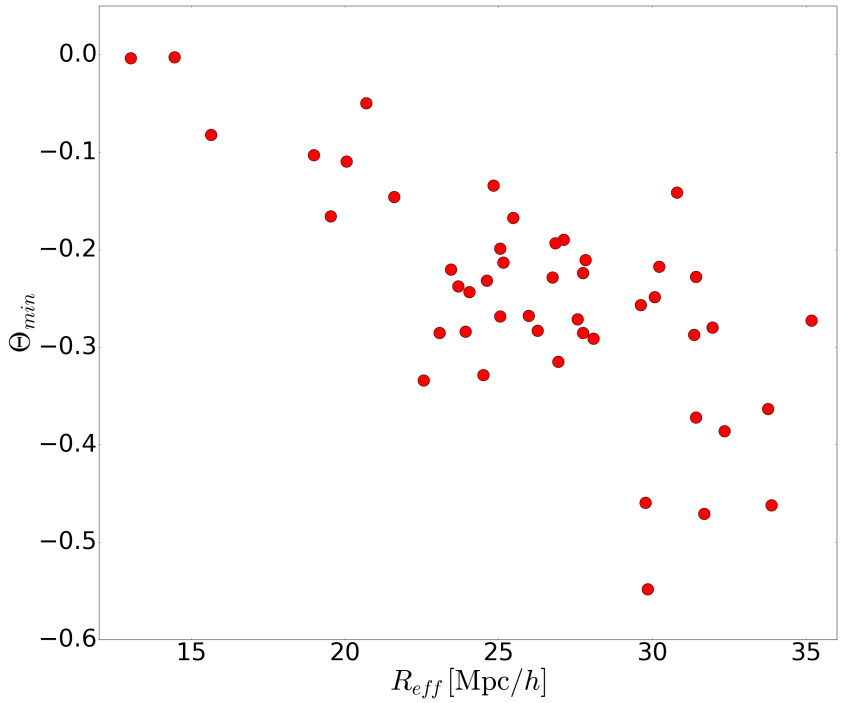

FIGURE 6.3 - Correlation between the effective radii, R_{eff}, and the minimum of divergence, $\boldsymbol{\Theta}_{min}$.

6.3.1 VOID SHAPES

In the following, we provide the same sample slice proposed in Figure 6.1, overlaying the spheres (white circles) having the same volumes of the corresponding cosmic voids centred at their minimum divergence positions (red crosses) (see subsection 5.5.1). Moreover, we have highlighted the contour levels (blue curves) corresponding to the zero-level of the divergence field, $\boldsymbol{\Theta} = 0$, which identify the void boundaries.

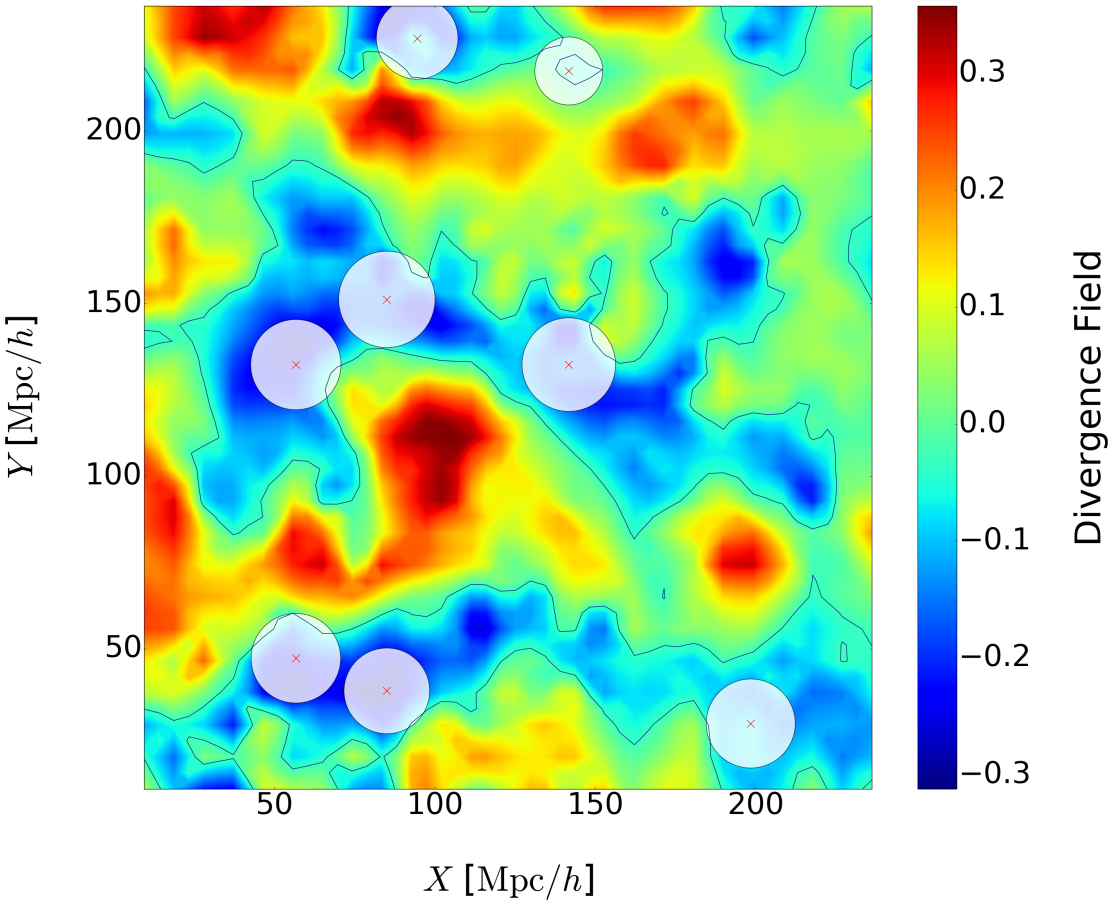

FIGURE 6.4 - The divergence field, $\boldsymbol{\Theta}$, (coloured map) corresponding to the slice in Figure 6.1. The white circles represent the spheres having the same effective radii of the detected cosmic voids. The red crosses represent the centre of each void, defined as the minimum value of the divergence field.

6.4 Stacked Density Profiles

According to the standard ΛCDM model, there is a *self-similar* phase during the cosmic void evolution, (section 3.4), with no dependence on the tracers used to identify the cosmic voids (Hamaus et al., 2014). This self-similar process ensures that the void structure can be characterised only by one parameter, that is the *effective radius*, R_{eff}. Despite the wide range of possible void radii, one can average the internal density distribution, rescaling the density to R_{eff}, to investigate the common behaviour of different voids.

Usually, in order to obtain a *stacked density profile*, the void sample is subdivided into groups, having similar effective radii. If the spherical evolution model is used to describe the void evolution, it is convenient to estimate the averaged density field in concentric shells around each void centre. We computed the number density of the haloes inside the detected voids in a logarithmic-spaced series of spherical shells

$$\bar{n}_i = \frac{1}{N} \sum_{j=0}^{N} \frac{n_i^j}{\langle n \rangle}, \tag{6.1}$$

where $\bar{n}_i$ is the mean density of haloes within voids included in the i-th bin, N is the number of voids in the i-th bin, n_i^j is the number density of the i-th bin of the j-th void and $\langle n \rangle$ is the mean number density of the tracer sample.

Figure 6.5 shows the density profiles of the entire void sample (spanning over the range $13-36\ h^{-1}$Mpc in R_{eff}), without applying the stacking procedure. Specifically, these profiles have been obtained by normalising the density of each void to the mean density value of the sample, and the distances from the centres are rescaled using the effective radius of each void.

In the following, we provide some examples of stacked density profiles. In particular, Figure 6.6 shows the stacked profile obtained by using voids in the entire range of effective radii. We have decided to use all the identified voids, due to the low statistics. Moreover, we removed voids whose centre is located at a distance lower than $2\times R_{eff}$ from the box boundaries, in order to reduce the underestimation of the density in the external regions, due to the lack of tracers. The green error bars, i.e. the *rms* for each bin, provide an estimate of the scatter from the stacked profile. Figure 6.7 and Figure 6.8 show two stacked density profiles obtained for the range of effective radii $20 < R_{eff}/[\mathrm{Mpc}/h] < 24$ and $24 < R_{eff}/[\mathrm{Mpc}/h] < 28$, respectively.

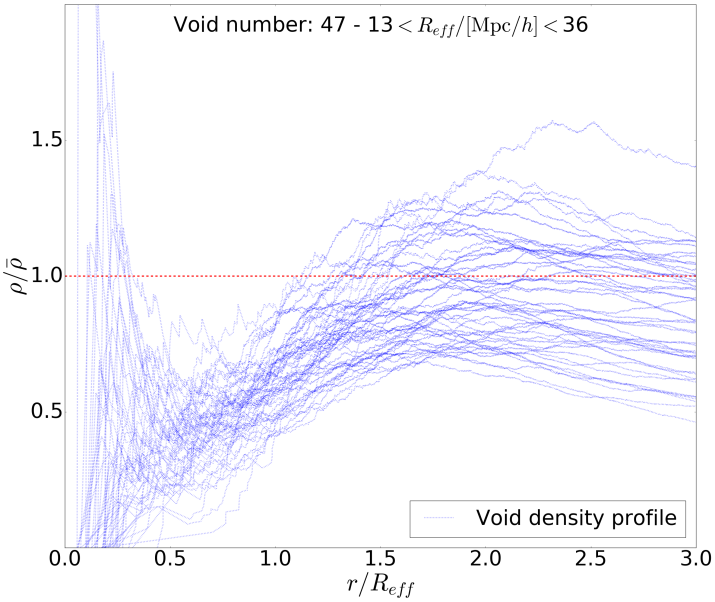

FIGURE 6.5 - The density profiles (blue dotted lines) of all the detected cosmic voids. The scale is in units of the effective radius, r/R_{eff}. The red dashed line represents the mean density in the simulation.

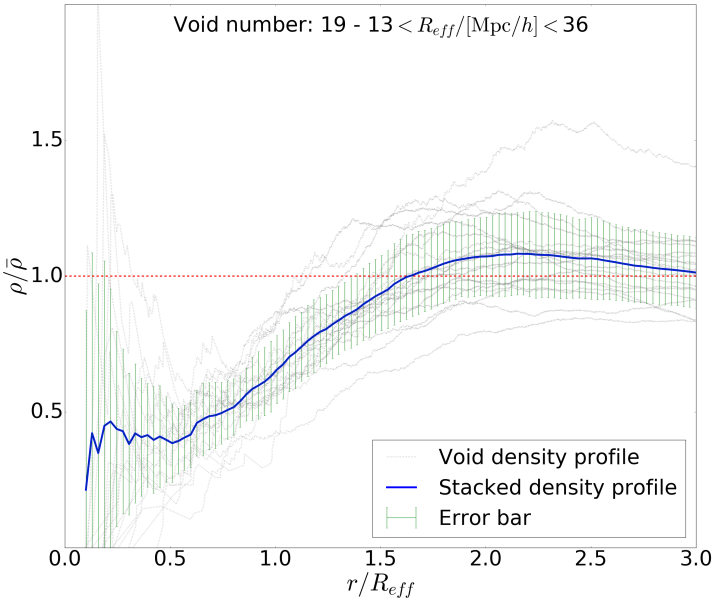

FIGURE 6.6 - The stacked density profile (blue thick line) with error bars overplotted on the single void density profiles (grey dotted lines). The considered voids have effective radii into the range $13 < R_{eff}/[\mathrm{Mpc}/h] < 36$.

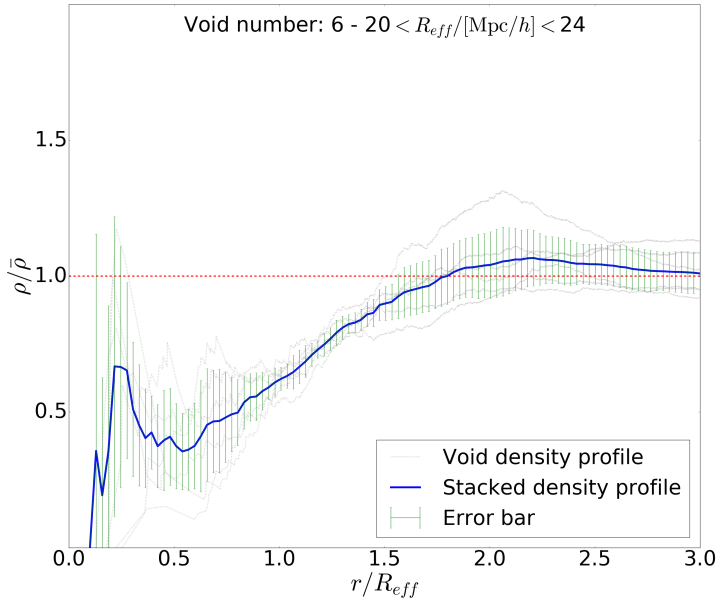

FIGURE 6.7 - Same as Figure 6.6, but for voids with R_{eff} in the range $20 < R_{eff}/[\mathrm{Mpc}/h] < 24$.

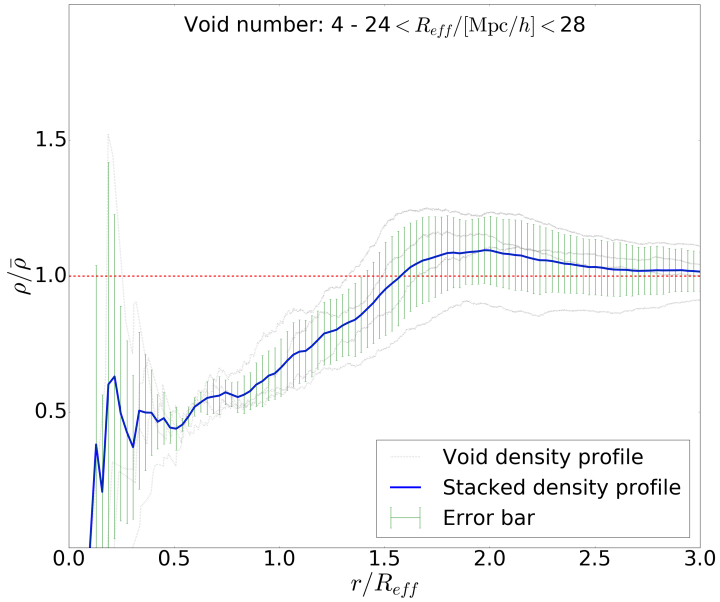

FIGURE 6.8 - Same as Figure 6.6, but for voids with R_{eff} in the range $24 < R_{eff}/[\mathrm{Mpc}/h] < 28$.

As expected, after an initial rising of the profiles, there is a small bump, due to the local presence of tracers in correspondence of the void boundaries, which implies a local enhancement of the density. Usually, this compensation can be identified in the profiles in correspondence of $r/R_{eff} = 1$, i.e. the void boundary. Instead, in our plots, the compensation is shifted at $r/R_{eff} = 1.5 - 2$, as clearly visible, for instance, in Figure 6.8. This shifting in r/R_{eff} could be due to the low statistics of our void sample in these stacked profiles, and even more to the elongated shapes (not quite spherical) of the detected underdense regions, as visible in Figure 6.4.

After the compensation, the stacked profile tends asymptotically to $\rho/\bar{\rho} = 1$, i.e. to the mean density value of the considered simulation.

6.5 Comparison with the LZVF Algorithm

We compare the results obtained by using our new Void Finder with the ones derived using the `LZVF` algorithm (Elyiv et al., 2015) (see subsection 4.2.7). In Table 6.1 we summarise the settings and the main results obtained by both algorithms, applying them to the same $z = 0$ DM halo catalogue.

TABLE 6.1 - Summary table showing the parameter settings and the main results obtained by our Void Finder and `LZVF`.

	Void Finder	`LZVF`
Settings		
# Reconstructions	10	10
Shuffle index	10	-
`PIZA` iterations	-	5000
Results		
Void number	47	41
Radius range [h^{-1}Mpc]	(13.0 – 35.2)	(15.9 – 37.8)

In the following, we provide five slices along the Z-axis, with a thickness of 50 h^{-1}Mpc, plotting the cosmic voids detected by both the algorithms (as Figure 6.4). Furthermore, for instance, Figure 6.10 shows the map of the difference of the divergence fields obtained with the two different codes. In this map, both the effective spheres obtained by our Void Finder (purple solid circles) and by `LZVF` (green dashed circles) and the void boundaries

(purple solid curves and green dashed curves, respectively) are displayed.

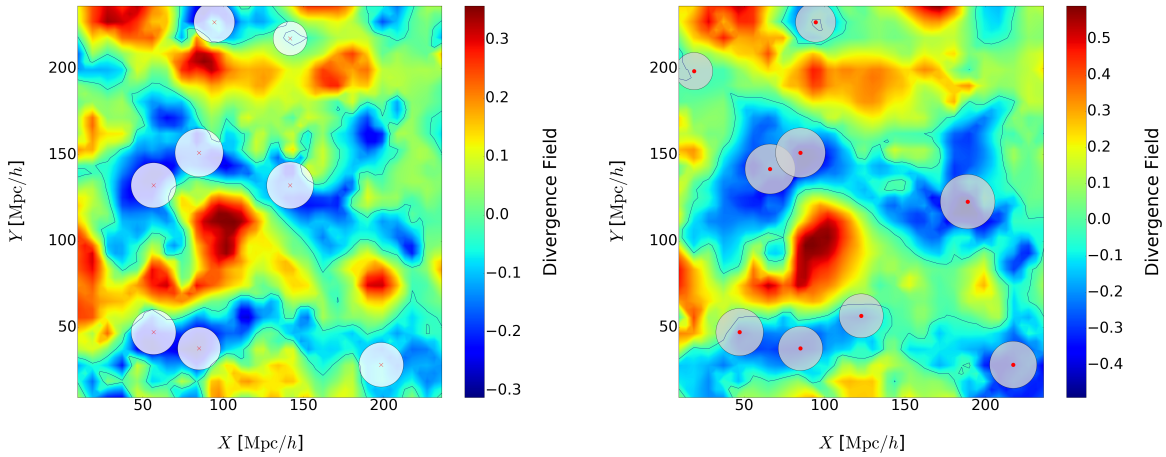

FIGURE 6.9 - Same slice of Figure 6.1 at $\Delta Z = 0 - 50\ h^{-1}$Mpc obtained by our Void Finder (*left panel*) and by the LZVF algorithm (*right panel*).

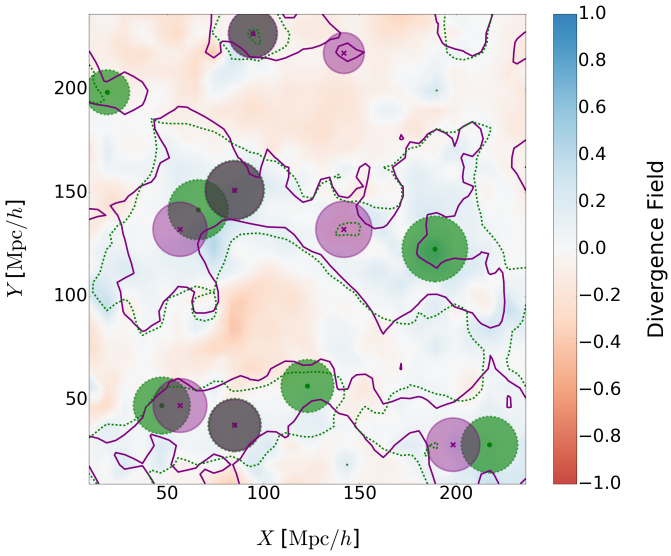

FIGURE 6.10 - Residual divergence map (coloured map) with the effective spheres (purple solid circles for our Void Finder and green dashed circles for LZVF) and the zero-contour levels of density (purple solid lines for our Void Finder and green dashed lines for LZVF).

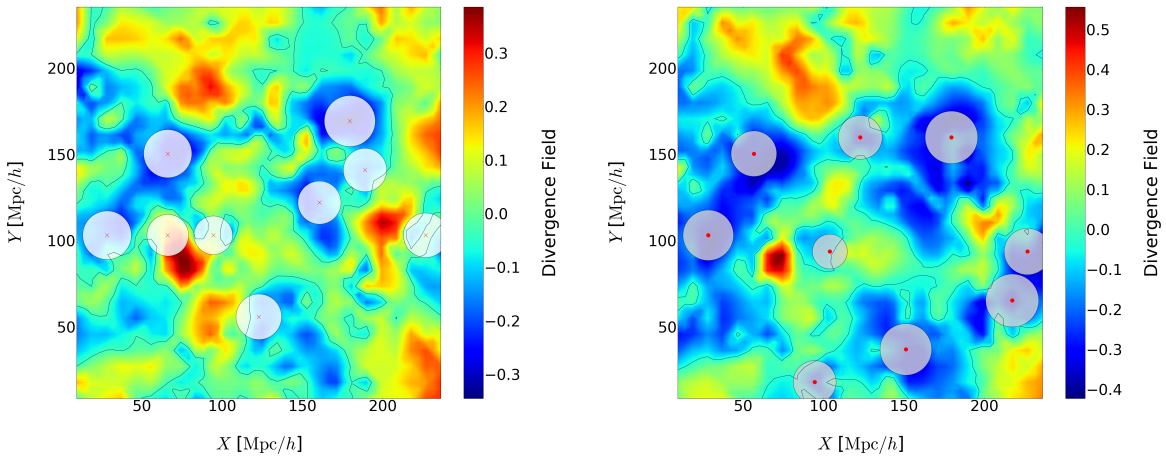

FIGURE 6.11 - Same as Figure 6.9, but for $\Delta Z = 50 - 100\ h^{-1}$Mpc.

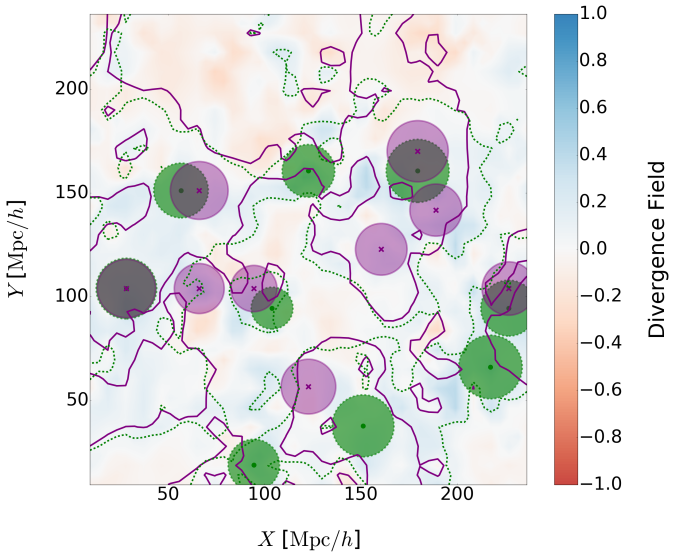

FIGURE 6.12 - Same as Figure 6.10, but for $\Delta Z = 50 - 100\ h^{-1}$Mpc.

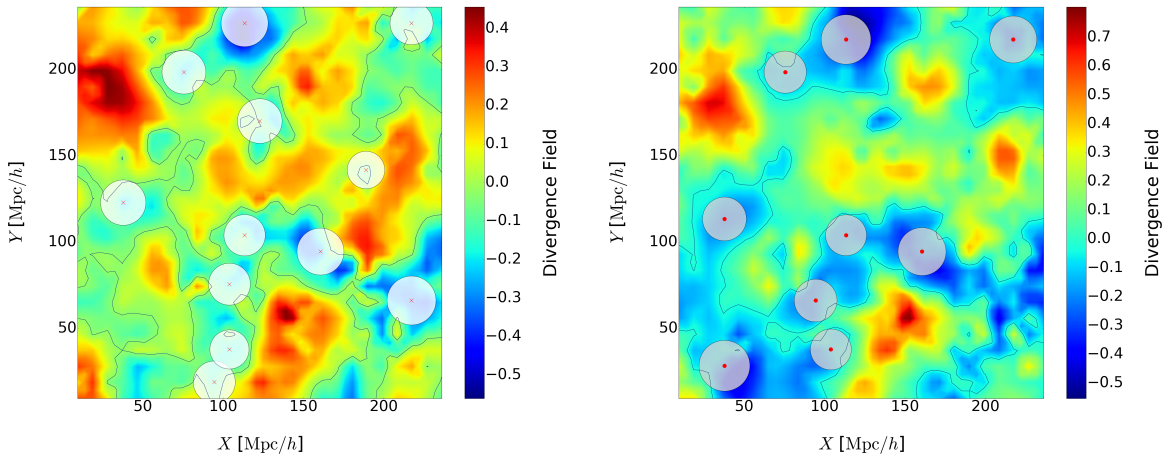

FIGURE 6.13 - Same as Figure 6.9, but for $\Delta Z = 100 - 150\ h^{-1}$Mpc.

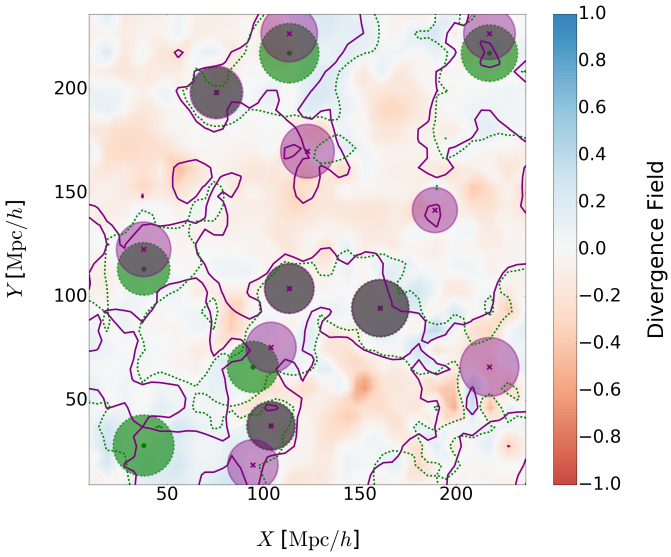

FIGURE 6.14 - Same as Figure 6.10, but for $\Delta Z = 100 - 150\ h^{-1}$Mpc.

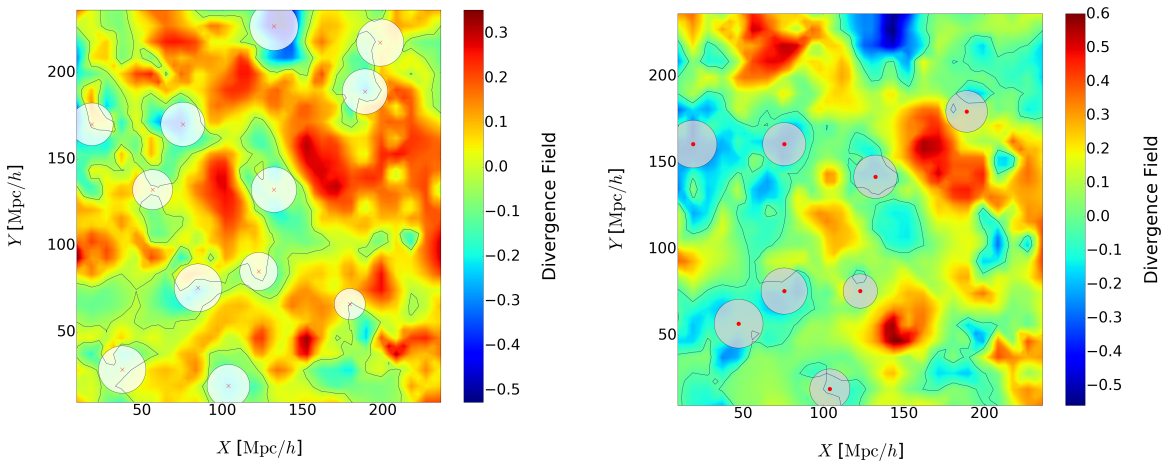

FIGURE 6.15 - Same as Figure 6.9, but for $\Delta Z = 150 - 200\ h^{-1}\text{Mpc}$.

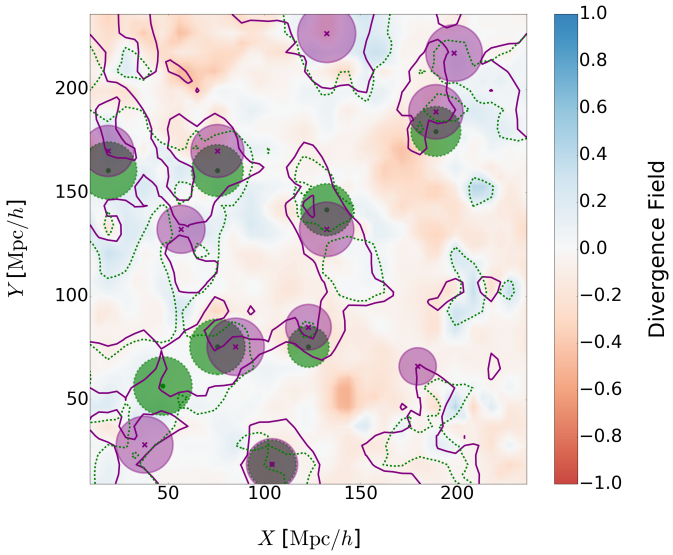

FIGURE 6.16 - Same as Figure 6.10, but for $\Delta Z = 150 - 200\ h^{-1}\text{Mpc}$.

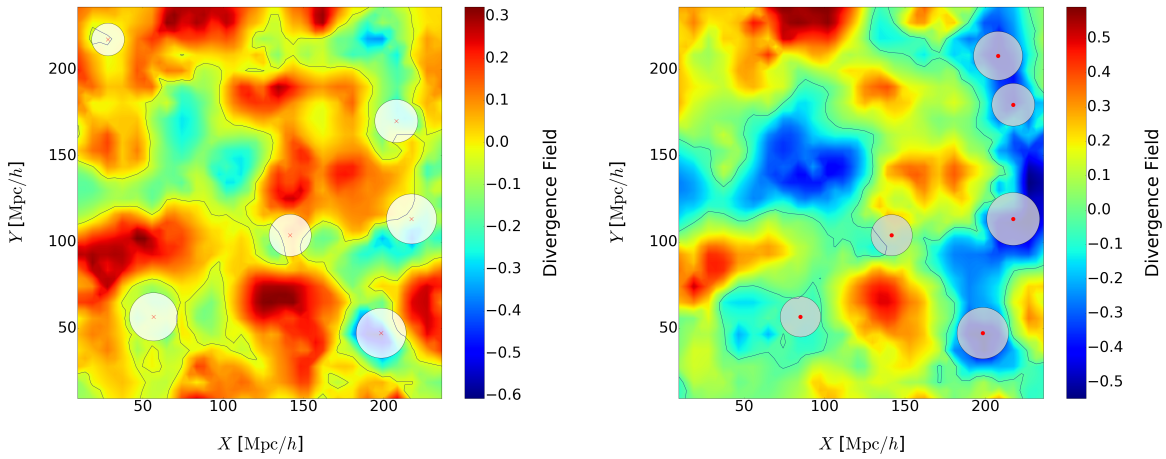

FIGURE 6.17 - Same as Figure 6.9, but for $\Delta Z = 200 - 250\ h^{-1}\,\mathrm{Mpc}$.

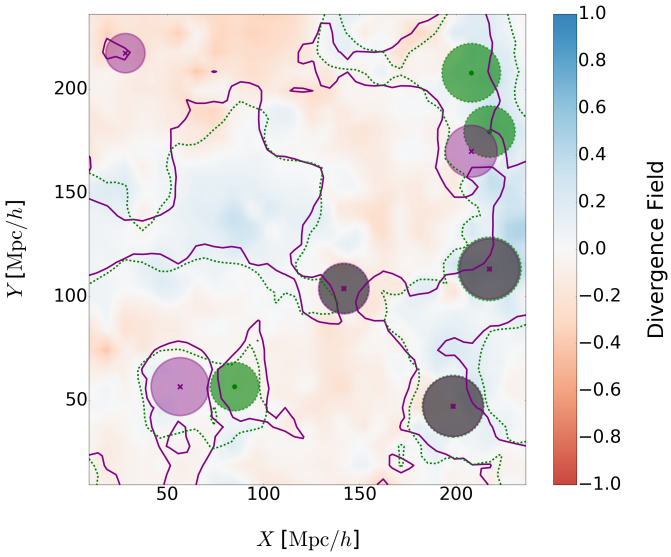

FIGURE 6.18 - Same as Figure 6.10, but for $\Delta Z = 200 - 250\ h^{-1}\,\mathrm{Mpc}$.

As it can be seen by looking at the same slices of the considered sample, the two Void Finders are in good agreement in the detection of the low-density regions. Though there are small differences in the number of detected voids by the two algorithms and in the range of the effective radii (see Table 6.1), the contour levels overplotted on the residual maps draw similar shapes of the found underdensities. Moreover, the divergence field in each cell computed by both algorithms does not differ significantly, as shown by the residual coloured map. In some cases, even both the local minima identified by our Void Finder and `LZVF`, and the computed effective radii coincide (grey overlapped circles).

Figure 6.19 shows a scatter distribution obtained by matching 1-1 the grid points where the divergence field is computed by both algorithms. As expected, the blue dots are distributed along the bisecting (red dashed line) of the graph, implying, on average, (as the previous residual divergence maps) a small difference in the estimate of the divergence field by both methods.

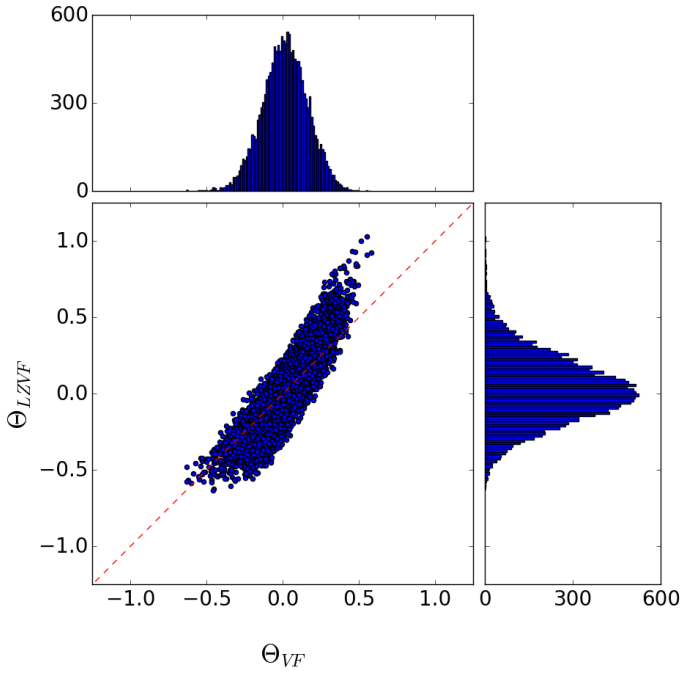

FIGURE 6.19 - The scatter distribution obtained by matching 1-1 the divergence grid points computed by our Void Finder ($\boldsymbol{\Theta}_{VF}$) and by `LZVF` ($\boldsymbol{\Theta}_{LZVF}$).

However, a small systematic deviation from the bisector can be noted in correspondence of the higher values in the scatter plot. This is an indication that the `LZVF` algorithm tends to overestimate the divergence field in some regions. This difference could be due to the different method used by the algorithms to reconstruct the displacement field.

Specifically, LZVF uses the PIZA method for the reconstruction (see subsection 4.2.7). Because of the random connection performed by PIZA between the haloes of the input catalogue and those of the random distribution, the reconstructed paths are, on average, longer w.r.t. the ones computed by our algorithm. This can originate a small bias in the reconstruction of the orbits. Instead, the research of the closest pairs performed by the LaZeVo method does not allow to link particles too far apart. This implies that, on average, the divergence field computed by our algorithm covers a range of values less wide than the one estimated using LZVF.

Figure 6.20 illustrates the differential distributions of the radii of the void identified by the two methods, the blue striped histogram for our Void Finder and the filled green one for LZVF, respectively. As it can be noted from the figure and as it can be seen in Table 6.1, the two distributions are not very different. However, in our case, the Void Finder detected smaller voids (the smallest one having a R_{eff} around 13 h^{-1}Mpc) with respect to LZVF, which, on the contrary, identified voids larger than 35 h^{-1}Mpc. Furthermore, our algorithm, on average, found a greater number of voids than LZVF, in the range $25-35$ h^{-1}Mpc.

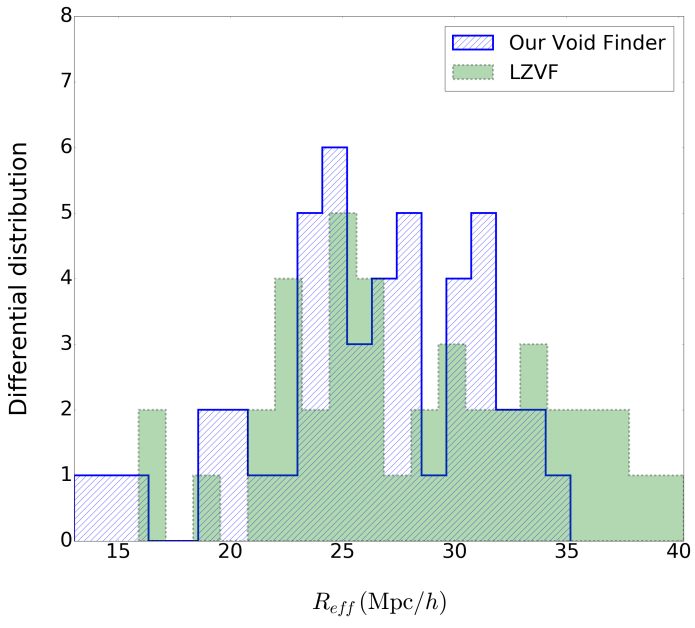

FIGURE 6.20 - The differential distribution of detected cosmic voids as a function of the effective radius, R_{eff}. The blue striped histogram represents the void distribution obtained by our Void Finder, while the green filled histogram is the distribution of the voids identified by the LZVF algorithm.

The small difference in the number counts and in the size distribution of the detected voids could be explained as due to the identification of a larger number of smaller voids (identified by our algorithm) in the same underdense regions where the LZVF algorithm detected just one larger void.

Finally, we compared the obtained stacked density profiles by the two methods, considering, as before, just the cosmic voids having centres located at a distance greater than $2 \times R_{eff}$ from the boundaries of the box. As visible in Figure 6.21, the two profiles are very similar, with the only notable exception that the one obtained by the LZVF method is a bit more overdense w.r.t the profile of our Void Finder. The considerations set out at the end of the section 6.4 about the shifted profile are also valid for the profile obtained by using the LZVF method. The similarity of the void distribution and even more of the elongated shapes (also drawn by LZVF) strengthens our possible explanations (together with the sparse sample one) about this shifting in R_{eff}.

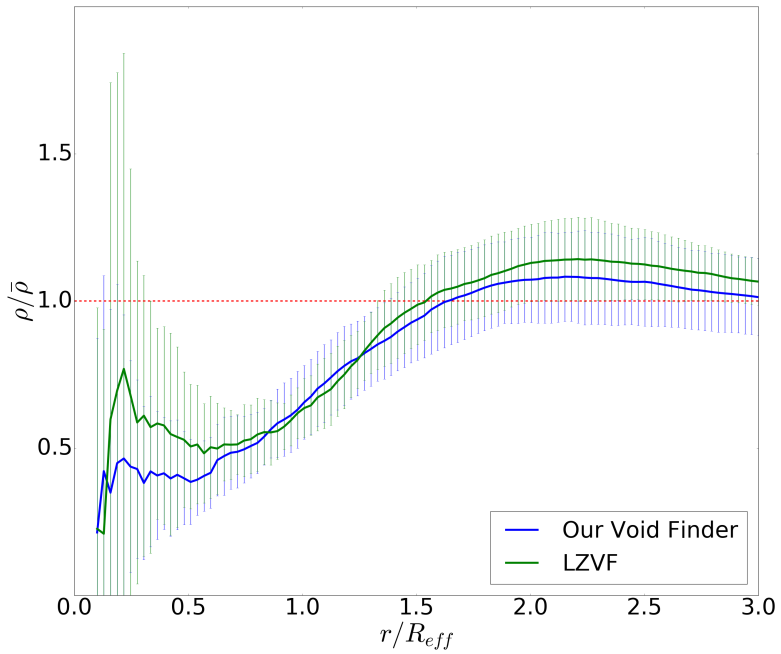

FIGURE 6.21 - The stacked density profiles obtained by our Void Finder algorithm (blue line) and by the LZVF algorithm.

Our Void Finder is able to locate in a better way the central position of the low-density regions, i.e. the ones with the lowest values of density. This is evident by looking to the range $[0.0 - 0.5]$ in the X-axis of the previous figure, where the blue profile takes on smaller values of $\rho/\bar{\rho}$, compared to the LZVF profile.

6.6 Towards a Cosmological Exploitation

As argued in Pisani et al. (2015), the most accurate theoretical models to predict the number of expected cosmic voids in the Universe, for a given cosmology, are strictly based on numerical simulations.

Theoretical models based on the *Press-Schechter formalism* (Press and Schechter, 1974) revisited *ad hoc* to describe the statistical properties of cosmic voids (Sheth and van de Weygaert, 2004) provide predictions of the expected number of voids in the DM distribution.

6.6.1 The Void Size Function

Sheth and van de Weygaert (2004) proposed a model to describe the size distribution of cosmic voids, following an approach similar to the one used by Press and Schechter (1974) for the *mass function* of DM haloes. The key point consists in defining a void as a depression in the cosmic density field which has grown until reaching *shell-crossing*.

From the excursion set theory (Bond et al., 1991) applied on low-density regions (Jennings et al., 2013; Sheth and van de Weygaert, 2004), the fraction of the Universe occupied by voids is:

$$f_{\ln\sigma} = 2\sum_{j=1}^{\infty} j\pi x^2 \sin(j\pi\mathscr{D}) \exp\left[-\frac{(j\pi x)^2}{2}\right], \tag{6.2}$$

where

$$\mathscr{D} = \frac{|\delta_v|}{\delta_c + |\delta_v|} \qquad \text{and} \qquad x = \frac{\mathscr{D}}{|\delta_v|}\sigma; \tag{6.3}$$

in the previous equation $\delta_v = -2.71$ is the shell-crossing threshold for voids, and $\delta_c = \delta_{lin}^{vir} = 1.686$ is the critical linear value of the density contrast, that can be computed in linear theory with the spherical collapse model (Gunn and Gott, 1972).

Because of the presence of the infinite series in the eq. (6.2), it is useful to find a sufficiently accurate alternative expression. Jennings et al. (2013) provided the following approximation, accurate at the 0.2% level across the validity domain:

$$f_{\ln\sigma} \approx \begin{cases} \sqrt{\dfrac{2}{\pi}}\dfrac{|\delta_v|}{\sigma}\exp\left(-\dfrac{\delta_v^2}{2\sigma^2}\right) & x \le 0.276 \\ \\ 2\displaystyle\sum_{j=1}^{4} j\pi x^2 \sin(j\pi\mathscr{D}) \exp\left[-\frac{(j\pi x)^2}{2}\right] & x > 0.276 \end{cases} . \tag{6.4}$$

This quantity has to be computed to predict the void size function. Different models have been proposed in literature. The abundance of voids in linear theory is given by:

$$\left(\frac{\mathrm{d}n}{\mathrm{d}\ln r}\right)_{\rm lin} = \frac{f_{\ln(\sigma)}}{V(r_{\rm lin})}\frac{\mathrm{d}\ln\sigma^{-1}}{\mathrm{d}\ln r_{\rm lin}} = \frac{\mathrm{d}n(r_{\rm lin})}{\mathrm{d}\ln r_{\rm lin}}, \tag{6.5}$$

where the number density of voids is expressed in terms of the linear theory radius of the void, $r_{\rm lin}$. During the spherical evolution, the void expands from its linear radius. At some epoch of shell-crossing, $\rho_v \approx 0.21\rho_B$, where ρ_v is the void density and ρ_B is the background density[1]. An underdensity, evolving towards shell-crossing, has expanded by a factor $r/r_{\rm lin} \simeq 1.72$, with respect to the initial size. Sheth and van de Weygaert (2004) (hereafter, SvdW) proposed another model. The basic idea of the SvdW model consists in matching the number density of voids derived from the linear theory to the one obtained in the non-linear regime:

$$\left(\frac{\mathrm{d}n}{\mathrm{d}\ln r}\right)_{\rm SvdW} = \left.\frac{\mathrm{d}n(r_{\rm lin})}{\mathrm{d}\ln r_{\rm lin}}\right|_{r_{\rm lin}=r/1.72}. \tag{6.6}$$

This model is shifted with respect to the linear one towards larger scales, with no changes in amplitude. It implies a conservation of the void number during the growth ($n = n_{\rm lin}$). However, this assumption may be wrong, in particular for large voids, which tend to overlap each other. To overcome this issue, Jennings et al. (2013) proposed a new model assuming instead the volume fraction and the shape of the abundance size function are constant during the evolution. In this context, the non-linear theory of void abundance is described by the so-called *Volume conserving model* (Vdn), as

$$\left(\frac{\mathrm{d}n}{\mathrm{d}\ln n}\right)_{\rm Vdn} = \frac{\mathrm{d}n(r_{\rm lin})}{\mathrm{d}\ln r_{\rm lin}}\frac{V(r_{\rm lin})}{V(r)}\frac{\mathrm{d}\ln r_{\rm lin}}{\mathrm{d}\ln r}. \tag{6.7}$$

6.6.2 The Cleaning Correction

One of the most important issues concerning voids consists in covering the gap between the theoretical models and the void detection. For this reason, we will use a method to clean a detected void sample to be directly compared to the theoretical predictions (Ronconi et al., 2017, in preparation). The method consists in the following three steps.

First step The first step consists in rejecting the underdensities with a central density value higher than $(1+\delta_v^{nl})\bar{\rho}$, where δ_v^{nl} is the threshold in a non-linear regime (arbitrarily

[1] In the most general form, the density contrast of a perturbation in a Universe having just one component can be obtained by $1+\delta(r,t) = \rho(r,t)/\rho_B(r,t)$. So, in a non-linear regime, the density contrast is given by $1+\delta_v^{nl}(r,t) \approx 0.21$.

chosen) and $\bar{\rho}$ is the mean density value of the catalogue. Then, all the low-density regions having an effective radius beyond a given range, $[r_{min}, r_{max}]$, are removed. Finally, the underdensities having a density contrast greater than a multiple of the typical density contrast due to Poisson deviations are rejected.

Second step The second step consists in rescaling the low-density regions. Specifically, this procedure reconstructs the density profile for each spherical volume centred at the centre of each void. The final effective radius is computed as the largest radius having a density contrast equal to δ_v.

Third step Finally, the overlapping volumes are identified. In particular, given a couple of overlapping voids, the one having the higher central density value or, equivalently, the higher density contrast is removed.

6.6.3 Comparing to Theoretical Predictions

As part of the scientific activities in preparation of the Euclid space mission (Laureijs et al., 2011), a Void Challenge has been recently organised. The first goal is to compare different methods to detect cosmic voids. Our new Void Finder is competing in this challenge, together with the other algorithms implemented in the CBL environment (see section 5.1), for a void analyses (Ronconi and Marulli, 2017, in preparation).

6.6.3.1 The DM Halo Catalogue

As a first test for the Void Challenge, we applied our Void Finder to a DM halo catalogue extracted from the DEMNuni (Dark Energy and Massive Neutrino Universe) simulations (Castorina et al., 2015), providing a void catalogue and its void size function. The DEMNuni simulation follows the evolution of structure formation in massive neutrino cosmological models. It represents the actual state-of-art in terms of neutrino runs, for what concerns volume and mass resolutions.

6.6.3.2 The Void Catalogue

We apply our Void Finder to a subsample of the DEMNuni simulation of $1\,h^{-1}\,\mathrm{Gpc}$ in side, with about 2.3 million of DM haloes, extracted from the original comoving volume of $8\,h^{-3}\,\mathrm{Gpc}^3$. We detected 2967 cosmic voids. Then, the cleaning correction procedure described in subsection 6.6.2 has been applied. In Figure 6.22 the obtained void size

distribution is illustrated. Specifically, the black solid line represents the Vdn model, opportunely corrected for the halo bias term (Ronconi et al., 2017, in preparation), while the blue dots are the cosmic voids identified by our algorithm and rescaled with the cleaning correction. As it can be noted, there is a fairly good agreement between the data and the theoretical predictions. Concerning the small radii, the deviation from the model is due to the resolution and subsampling (Ronconi et al., 2017, in preparation).

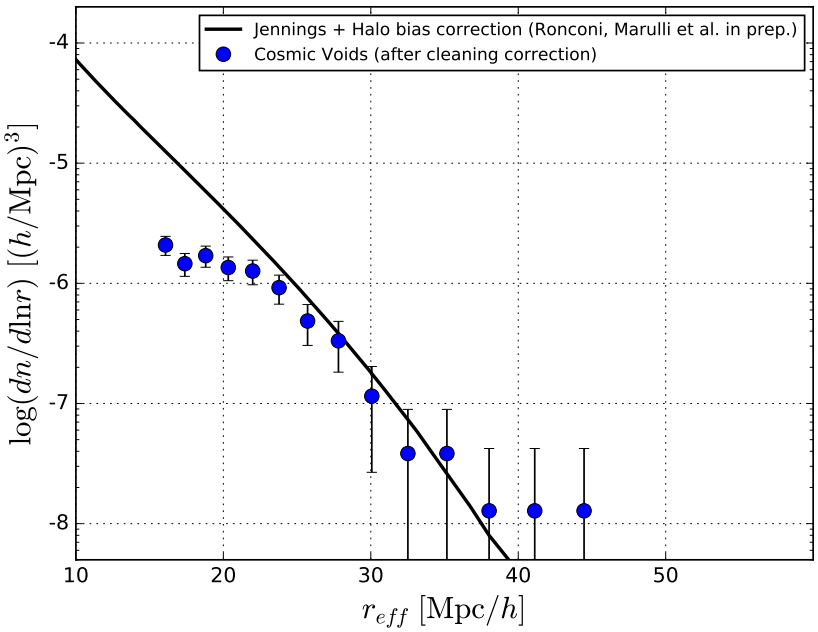

FIGURE 6.22 - Void size distribution of the catalogue obtained by our Void Finder on a subsample extracted from the DEMNuni simulations. The blue dots are the detected voids after the rescaling process. The black solid line is the Vdn model corrected for the halo bias.

CHAPTER 7

DISCUSSION AND CONCLUSIONS

In this final chapter we summarise the results of this thesis work, shedding light on the importance of implementing a new Void Finder based on a dynamical criterion, and we propose some related future perspectives.

We briefly describe the structure of our new Void Finder algorithm and its internal methods, from the reconstruction of the displacement field to the identification of local density minima, as candidate cosmic voids (section 7.1). In section 7.2, we expose the obtained results, discussing also the comparison made with the `LZVF` algortihm. Finally, in section 7.3, we discuss about the possible future developments of our project, looking for further improvements.

7.1 OUR PROJECT

Starting from the basic idea argued in Elyiv et al. (2015), we have developed a new Void Finder algorithm, which exploits the cosmic dynamics to identify the depressions in the density field. The proposed Void Finder is based on a dynamical criterion (according to the classification of Lavaux and Wandelt (2010)). We extensively tested it on a DM halo catalogue and made a comparison with the `LZVF` algorithm, by Elyiv et al. (2015).

This Void Finder is substantially composed by three main steps. The first part deals with the reconstruction of the displacement filed, by using an input tracer catalogue. The reconstruction may be performed by two methods: `LaZeVo` or `RIVA`. Briefly, by exploiting the Zel'dovich approximation (see subsubsection 2.6.4.1), `LaZeVo` looks for the closest

pairs between the input object catalogue and a random distribution (subsection 5.3.2). While the first tracer sample represents the current inhomogeneous distribution of sources, constituting the clumps and filaments of the Cosmic Web, the random field describes the early configuration of objects, in a homogeneous Universe. The Zel'dovich approximation is used to draw the back-in-time evolution of tracers, passing from an inhomogeneous to a homogeneous distribution. The `RIVA` methods relies on the properties of the two-point correlation function (see Equation 2.91). As `LaZeVo`, the aim of this method is to reach a random distribution of particles, starting from the initial one. It exploits the different correlations which characterise the two configurations. As a consequence of a random motion of the particles, the new configuration is kept, if the amplitude of the 2PCF has been reduced. This process ends when an almost zero-amplitude of the correlation function has been reached (see subsection 5.3.3).

Both these two methods use tracers as *test particles*, to reconstruct their initial Lagrangian positions. The resulting displacement field, obtained by the simple connection between the "starting" and "ending" points, is then used to compute the density field, starting from the velocity divergence (see subsection 5.3.1). The divergence of the displacement field is then used to identify the regions characterised by low-density values, that represent the cosmic void candidates. Therefore, in this reverse-vision, a void is a "sink" within which tracers flow. By using the watershed technique (subsection 4.2.4), the Void Finder detects single underdense structures, the subvoids, then merges or rejects them, under *ad hoc* conditions, in order to find a final void catalogue (see section 5.5).

7.2 Results

We tested our new Void Finder on a $z = 0$ catalogue composed by about 60000 DM haloes, extracted from a ΛCDM simulation. As shown in Figure 6.1, we reconstructed both the displacement field and the divergence map. As it can be noted, the longer arrows originate from the overdense regions and are directed towards the underdense ones, in agreement with what is expected in this time-reverse scenario.

From this halo catalogue, we extracted 47 voids, spanning a range in effective radii from around 13 h^{-1}Mpc to more than 35 h^{-1}Mpc, finding also a fairly good correlation between the void sizes and the divergence value of the void centres (as shown in Figure 6.3).

Furthermore, we computed the stacked density profiles (see section 6.4), finding the expected features, i.e. an initial rising of the profile in the inner regions, a compensation

(the characteristic small bump), as a result of the local overdensity due to the tracers arranged in filaments and clusters, and the asymptotic behaviour beyond the external edges, due to the reaching of the mean density value of the simulation. Although the characteristic profile shape has been well reproduced, we found a shift towards higher effective radii, as a consequence of the considered sparse sample and the elongated void shapes.

We also made a comparison between our new Void Finder and the LZVF algorithm, by Elyiv et al. (2015). From this direct comparison between the two dynamical detection methods, we found a good agreement in the number of identified voids and in their main properties.

One of the main advantages of our new Void Finder is in terms of computing time. Indeed, the parallel implementation of the *chain-mesh* method (see subsubsection 5.3.2.1), used both in the research of the closest pairs for LaZeVo and for the estimation of the 2PCF for RIVA, ensures a considerable reduction of the computing time. Moreover, the presence of an initial parameter file allows the user to easily manage the parameter settings with larger flexibility.

Our Void Finder is now part of the CBL (Marulli et al., 2016) *living project* (see section 5.1), an open source C++/Python library aimed at defining a common numerical environment for cosmological treatments. Together with other CBL algorithms developed by Ronconi and Marulli (2017, in preparation) for measuring and modelling the void abundances (Ronconi et al., 2017, in preparation), our Void Finder is currently competing in the new Void Challenge, recently proposed as part of the scientific activities for the preparation of the Euclid space mission (see section 6.6). In this context, we obtained a reasonable agreement between the size function of the cosmic voids detected by our Void Finder, on a preliminary Euclid mock catalogue, opportunely rescaled by the cleaning correction method (Ronconi and Marulli, 2017), described in subsection 6.6.2, and theoretical prescriptions.

7.3 Work in Progress & Future Perspectives

The results that we have outlined in the previous section need further validations. For this reason, there are many directions in which our project can be extended.

First of all, we are making our Void Finder public, as an extension of the CBL libraries, adding the following improvements.

- We are finalising the integration of the RIVA method, as a further reconstructor

method of the displacement field (subsection 5.3.3). Once the RIVA implementation will be finished, the user will be able to decide which method to use to reconstruct the displacement of tracers. Moreover, we want to integrate the reconstruction step with the other displacement methods available in the CBL, for the reconstruction of the density field used for BAO analyses, in order to make a comparison between the different methods in terms of void detection, time scaling, etc.

- We are going to integrate the cleaning correction method (described in subsection 6.6.2) as a fourth step of our code, in order to obtain a unique algorithm able to detect the local density minima, i.e. the voids, ready to be compared with the theoretical models of void abundances, for subsequent cosmological exploitation.

- We are implementing a set of plot scripts (that will be available together with the Void Finder algorithm in the CBL library) for the visualisation of the displacement and divergence maps, 2D & 3D graphical representations of the detected voids and more, by using the Matplotlib and Mayavi Python-packages, building-up a platform for more detailed and accurate analyses.

- We are going to extend the comparison with other Void Finders in literature, not only those based on dynamical approaches (e.g., LZVF), but also other algorithms exploiting different criteria, such as the geometrical-method VIDE, with the aim of better understanding how to match the identified cosmic voids by different codes, similarly to what has been done in the Aspen-Amsterdam project (see section 4.3).

In the following, we list some of the upcoming developments, concerning the Void Challenge proposed by the clustering science working group of the Euclid space mission, that will be presented to the Euclid annual meeting in London in the next summer.

- We are currently running our code on the entire DEMNuni DM halo catalogue (see subsubsection 6.6.3.1), in order to obtain the complete void catalogue, to compare with the detection methods developed by the other participant teams.

- The next step will be to use more realistic tracer catalogues, i.e. the PKDGRAV3 simulation (Potter et al., 2016). The PKDGRAV3 is a majestic cosmological simulation, composed by 2 trillion particles, run on the Piz Daint supercomputer, in Switzerland. The selected tracers will be $\sim 10^7$ galaxies extracted from the spectroscopic mock catalogue, which will be subdivided in different redshift slices.

Finally, we want to report some of the possible further future perspectives of this project.

- We want to conduct an accurate geometrical analyses of the void shapes. Specifically, to investigate the geometrical features of the identified voids, we will provide an estimate of the ellipticity of stacked voids, by using the second moments of the divergence field, $\mathbf{\Theta}$. To do that, we will compute the *inertial tensor*, $\mathscr{I}$, that is composed by the i,j components, χ_i and χ_j, defined in the Lagrangian space w.r.t. the void centre, as follows:

$$\mathscr{I} = \sum \chi_i \chi_j \mathbf{\Theta}(\mathbf{q}). \tag{7.1}$$

  By computing the eigenvalues, Λ_i, of the $\mathscr{I}_{i,j}$ matrix, the *ellipticity*, e , is defined as the axial ratio between these eigenvalues:

$$e_{i,j} = \sqrt{\Lambda_i / \Lambda_j}\,. \tag{7.2}$$

  where i,j are the permuted indices in the range [1,3], with $\Lambda_i \geq \Lambda_j$.

- Finally, we plan to apply our Void Finder to real data. Specifically, to VIPERS (Guzzo and The Vipers Team, 2013) and BOSS (Dawson et al., 2013) galaxy catalogues, and, in the next future, to the forthcoming Euclid one. In this context, we plan to investigate about the systematic observational effects in real surveys, so to validate the algorithm also for real object catalogues.

In conclusion, our new Void Finder is a promising tool for the investigation of the cosmic voids in the Universe, in order to improve the accuracy of the cosmological tests based on void statistics.

BIBLIOGRAPHY

K. N. Abazajian, J. K. Adelman-McCarthy, M. A. Agüeros, S. S. Allam, C. Allende Prieto, D. An, K. S. J. Anderson, S. F. Anderson, J. Annis, N. A. Bahcall, and et al.
The Seventh Data Release of the Sloan Digital Sky Survey.
Astrophysical Journal, Supplement, 182:543-558, June 2009.
doi: 10.1088/0067-0049/182/2/543.

G. O. Abell.
Evidence regarding second-order clustering of galaxies and interactions between clusters of galaxies.
Astronomical Journal, 66:607, December 1961.
doi: 10.1086/108472.

C. P. Ahn, R. Alexandroff, C. Allende Prieto, F. Anders, S. F. Anderson, T. Anderton, B. H. Andrews, É. Aubourg, S. Bailey, F. A. Bastien, and et al.
The Tenth Data Release of the Sloan Digital Sky Survey: First Spectroscopic Data from the SDSS-III Apache Point Observatory Galactic Evolution Experiment.
Astrophysical Journal, Supplement, 211:17, April 2014.
doi: 10.1088/0067-0049/211/2/17.

J. Aikio and P. Mähönen.
A Simple Void-searching Algorithm.
Astrophysical Journal, 497:534–540, April 1998.
doi: 10.1086/305509.

S. Alam, F. D. Albareti, C. Allende Prieto, F. Anders, S. F. Anderson, T. Anderton, B. H. Andrews, E. Armengaud, É. Aubourg, S. Bailey, and et al.
The Eleventh and Twelfth Data Releases of the Sloan Digital Sky Survey: Final Data from SDSS-III.
Astrophysical Journal, Supplement, 219:12, July 2015.
doi: 10.1088/0067-0049/219/1/12.

C. Alcock and B. Paczynski.
An evolution free test for non-zero cosmological constant.
Nature, 281:358, October 1979.
doi: 10.1038/281358a0.

D. Alonso.
CUTE solutions for two-point correlation functions from large cosmological datasets.
ArXiv e-prints, October 2012.

L. Amendola.
Coupled quintessence.
Physical Review D, 62(4):043511, August 2000.
doi: 10.1103/PhysRevD.62.043511.

L. Amendola.
Linear and nonlinear perturbations in dark energy models.
Physical Review D, 69(10):103524, May 2004.
doi: 10.1103/PhysRevD.69.103524.

Neta A. Bahcall.
Clustering and Large Scale Structure with the SDSS.
Publ.Astron.Soc.Pac. 107 (1995) 790, March 1995.
doi: 10.1086/133625.

M. Baldi.
Time-dependent couplings in the dark sector: from background evolution to non-linear structure formation.
Monthly Notices of the RAS, 411:1077–1103, February 2011.
doi: 10.1111/j.1365-2966.2010.17758.x.

M. Baldi.
The CoDECS project: a publicly available suite of cosmological N-body simulations for interacting dark energy models.
Monthly Notices of the RAS, 422:1028–1044, May 2012.
doi: 10.1111/j.1365-2966.2012.20675.x.

J. M. Bardeen, J. R. Bond, N. Kaiser, and A. S. Szalay.
The statistics of peaks of Gaussian random fields.
Astrophysical Journal, 304:15–61, May 1986.

doi: 10.1086/164143.

J. Barnes and P. Hut.
A hierarchical O(N log N) force-calculation algorithm.
Nature, 324:446–449, December 1986.
doi: 10.1038/324446a0.

E. Bertschinger.
Cosmological detonation waves.
Astrophysical Journal, 295:1–13, August 1985.
doi: 10.1086/163342.

G. R. Blumenthal, L. N. da Costa, D. S. Goldwirth, M. Lecar, and T. Piran.
The largest possible voids.
Astrophysical Journal, 388:234–241, April 1992.
doi: 10.1086/171147.

J. R. Bond, S. Cole, G. Efstathiou, and N. Kaiser.
Excursion set mass functions for hierarchical Gaussian fluctuations.
Astrophysical Journal, 379:440–460, October 1991.
doi: 10.1086/170520.

J. R. Bond, L. Kofman, D. Pogosyan, and J. Wadsley.
Theoretical Tools for Large Scale Structure, October 1998.

Y. Brenier, U. Frisch, M. Hénon, G. Loeper, S. Matarrese, R. Mohayaee, and A. Sobolevskiĭ.
Reconstruction of the early Universe as a convex optimization problem.
Monthly Notices of the RAS, 346:501–524, December 2003.
doi: 10.1046/j.1365-2966.2003.07106.x.

R. Brunino, I. Trujillo, F. R. Pearce, and P. A. Thomas.
The orientation of galaxy dark matter haloes around cosmic voids.
Monthly Notices of the RAS, 375:184–190, February 2007.
doi: 10.1111/j.1365-2966.2006.11282.x.

Y.-C. Cai, M. C. Neyrinck, I. Szapudi, S. Cole, and C. S. Frenk.
A Possible Cold Imprint of Voids on the Microwave Background Radiation.
Astrophysical Journal, 786:110, May 2014.
doi: 10.1088/0004-637X/786/2/110.

Y.-C. Cai, N. Padilla, and B. Li.
Testing gravity using cosmic voids.
Monthly Notices of the RAS, 451:1036–1055, July 2015.
doi: 10.1093/mnras/stv777.

E. Castorina, C. Carbone, J. Bel, E. Sefusatti, and K. Dolag.
DEMNUni: the clustering of large-scale structures in the presence of massive neutrinos.
Journal of Cosmology and Astroparticle Physics, 7:043, July 2015.
doi: 10.1088/1475-7516/2015/07/043.

M. Chevallier and D. Polarski.
Accelerating Universes with Scaling Dark Matter.
International Journal of Modern Physics D, 10:213–223, 2001.
doi: 10.1142/S0218271801000822.

R. Cid Fernandes, G. Stasińska, A. Mateus, and N. Vale Asari.
A comprehensive classification of galaxies in the Sloan Digital Sky Survey: how to tell true from fake AGN?
Monthly Notices of the RAS, 413:1687–1699, May 2011.
doi: 10.1111/j.1365-2966.2011.18244.x.

J. Clampitt and B. Jain.
Lensing measurements of the mass distribution in SDSS voids.
Monthly Notices of the RAS, 454:3357–3365, December 2015.
doi: 10.1093/mnras/stv2215.

T. Clifton, P. G. Ferreira, A. Padilla, and C. Skordis.
Modified gravity and cosmology.
Physics Reports, 513:1–189, March 2012.
doi: 10.1016/j.physrep.2012.01.001.

J. M. Colberg, R. K. Sheth, A. Diaferio, L. Gao, and N. Yoshida.
Voids in a ΛCDM universe.
Monthly Notices of the RAS, 360:216–226, June 2005.
doi: 10.1111/j.1365-2966.2005.09064.x.

J. M. Colberg, F. Pearce, C. Foster, E. Platen, R. Brunino, M. Neyrinck, S. Basilakos, A. Fairall, H. Feldman, S. Gottlöber, O. Hahn, F. Hoyle, V. Müller, L. Nelson, M. Plionis, C. Porciani, S. Shandarin, M. S. Vogeley, and R. van de Weygaert.
The Aspen-Amsterdam void finder comparison project.
Monthly Notices of the RAS, 387:933–944, June 2008.
doi: 10.1111/j.1365-2966.2008.13307.x.

S. Cole, W. J. Percival, J. A. Peacock, P. Norberg, C. M. Baugh, C. S. Frenk, I. Baldry, J. Bland-Hawthorn, T. Bridges, R. Cannon, M. Colless, C. Collins, W. Couch, N. J. G. Cross, G. Dalton, V. R. Eke, R. De Propris, S. P. Driver, G. Efstathiou, R. S. Ellis, K. Glazebrook, C. Jackson, A. Jenkins, O. Lahav, I. Lewis, S. Lumsden, S. Maddox, D. Madgwick, B. A. Peterson, W. Sutherland, and K. Taylor.
The 2dF Galaxy Redshift Survey: power-spectrum analysis of the final data set and cosmological implications.
Monthly Notices of the RAS, 362:505–534, September 2005.
doi: 10.1111/j.1365-2966.2005.09318.x.

P. Coles and F. Lucchin.
Cosmology: The Origin and Evolution of Cosmic Structure, Second Edition.
July 2002.

M. Colless, B. A. Peterson, C. Jackson, J. A. Peacock, S. Cole, P. Norberg, I. K. Baldry, C. M. Baugh, J. Bland-Hawthorn, T. Bridges, R. Cannon, C. Collins, W. Couch, N. Cross, G. Dalton, R. De Propris, S. P. Driver, G. Efstathiou, R. S. Ellis, C. S. Frenk, K. Glazebrook, O. Lahav, I. Lewis, S. Lumsden, S. Maddox, D. Madgwick, W. Sutherland, and K. Taylor.
The 2dF Galaxy Redshift Survey: Final Data Release.
ArXiv Astrophysics e-prints, June 2003.

R. A. C. Croft and E. Gaztanaga.
Reconstruction of cosmological density and velocity fields in the Lagrangian Zel'dovich approximation.
Monthly Notices of the RAS, 285:793–805, March 1997.
doi: 10.1093/mnras/285.4.793.

D. J. Croton, V. Springel, S. D. M. White, G. De Lucia, C. S. Frenk, L. Gao, A. Jenkins, G. Kauffmann, J. F. Navarro, and N. Yoshida.

The many lives of active galactic nuclei: cooling flows, black holes and the luminosities and colours of galaxies.
Monthly Notices of the RAS, 365:11–28, January 2006.
doi: 10.1111/j.1365-2966.2005.09675.x.

K. S. Dawson, D. J. Schlegel, C. P. Ahn, S. F. Anderson, É. Aubourg, S. Bailey, R. H. Barkhouser, J. E. Bautista, A. Beifiori, A. A. Berlind, V. Bhardwaj, D. Bizyaev, C. H. Blake, M. R. Blanton, M. Blomqvist, A. S. Bolton, A. Borde, J. Bovy, W. N. Brandt, H. Brewington, J. Brinkmann, P. J. Brown, J. R. Brownstein, K. Bundy, N. G. Busca, W. Carithers, A. R. Carnero, M. A. Carr, Y. Chen, J. Comparat, N. Connolly, F. Cope, R. A. C. Croft, A. J. Cuesta, L. N. da Costa, J. R. A. Davenport, T. Delubac, R. de Putter, S. Dhital, A. Ealet, G. L. Ebelke, D. J. Eisenstein, S. Escoffier, X. Fan, N. Filiz Ak, H. Finley, A. Font-Ribera, R. Génova-Santos, J. E. Gunn, H. Guo, D. Haggard, P. B. Hall, J.-C. Hamilton, B. Harris, D. W. Harris, S. Ho, D. W. Hogg, D. Holder, K. Honscheid, J. Huehnerhoff, B. Jordan, W. P. Jordan, G. Kauffmann, E. A. Kazin, D. Kirkby, M. A. Klaene, J.-P. Kneib, J.-M. Le Goff, K.-G. Lee, D. C. Long, C. P. Loomis, B. Lundgren, R. H. Lupton, M. A. G. Maia, M. Makler, E. Malanushenko, V. Malanushenko, R. Mandelbaum, M. Manera, C. Maraston, D. Margala, K. L. Masters, C. K. McBride, P. McDonald, I. D. McGreer, R. G. McMahon, O. Mena, J. Miralda-Escudé, A. D. Montero-Dorta, F. Montesano, D. Muna, A. D. Myers, T. Naugle, R. C. Nichol, P. Noterdaeme, S. E. Nuza, M. D. Olmstead, A. Oravetz, D. J. Oravetz, R. Owen, N. Padmanabhan, N. Palanque-Delabrouille, K. Pan, J. K. Parejko, I. Pâris, W. J. Percival, I. Pérez-Fournon, I. Pérez-Ràfols, P. Petitjean, R. Pfaffenberger, J. Pforr, M. M. Pieri, F. Prada, A. M. Price-Whelan, M. J. Raddick, R. Rebolo, J. Rich, G. T. Richards, C. M. Rockosi, N. A. Roe, A. J. Ross, N. P. Ross, G. Rossi, J. A. Rubiño-Martin, L. Samushia, A. G. Sánchez, C. Sayres, S. J. Schmidt, D. P. Schneider, C. G. Scóccola, H.-J. Seo, A. Shelden, E. Sheldon, Y. Shen, Y. Shu, A. Slosar, S. A. Smee, S. A. Snedden, F. Stauffer, O. Steele, M. A. Strauss, A. Streblyanska, N. Suzuki, M. E. C. Swanson, T. Tal, M. Tanaka, D. Thomas, J. L. Tinker, R. Tojeiro, C. A. Tremonti, M. Vargas Magaña, L. Verde, M. Viel, D. A. Wake, M. Watson, B. A. Weaver, D. H. Weinberg, B. J. Weiner, A. A. West, M. White, W. M. Wood-Vasey, C. Yeche, I. Zehavi, G.-B. Zhao, and Z. Zheng.
The Baryon Oscillation Spectroscopic Survey of SDSS-III.
Astronomical Journal, 145:10, January 2013.
doi: 10.1088/0004-6256/145/1/10.

V. de Lapparent, M. J. Geller, and J. P. Huchra.
A slice of the universe.
Astrophysical Journal, Letters, 302:L1–L5, March 1986.
doi: 10.1086/184625.

Avishai Dekel and Ofer Lahav.
Stochastic Nonlinear Galaxy Biasing.
Astrophys.J.520:24-34,1999, November 1998.
doi: 10.1086/307428.

B. Delaunay.
Sur la sphere vide.
Izv. Akad. Nauk SSSR, Otdelenie Matematicheskii i Estestvennyka Nauk, 7:793–800, 1934.

A. Dressler.
Galaxy morphology in rich clusters - Implications for the formation and evolution of galaxies.
Astrophysical Journal, 236:351–365, March 1980.
doi: 10.1086/157753.

J. Dubinski, L. N. da Costa, D. S. Goldwirth, M. Lecar, and T. Piran.
Void evolution and the large-scale structure.
Astrophysical Journal, 410:458–468, June 1993.
doi: 10.1086/172762.

G. Efstathiou, W. J. Sutherland, and S. J. Maddox.
The cosmological constant and cold dark matter.
Nature, 348:705–707, December 1990.
doi: 10.1038/348705a0.

A. Einstein.
Zur allgemeinen Relativitätstheorie.
Sitzungsberichte der Königlich Preußischen Akademie der Wissenschaften (Berlin), Seite 778-786., 1915.

D. J. Eisenstein, D. H. Weinberg, E. Agol, H. Aihara, C. Allende Prieto, S. F. Anderson, J. A. Arns, É. Aubourg, S. Bailey, E. Balbinot, and et al.

SDSS-III: Massive Spectroscopic Surveys of the Distant Universe, the Milky Way, and Extra-Solar Planetary Systems.
Astronomical Journal, 142:72, September 2011.
doi: 10.1088/0004-6256/142/3/72.

H. El-Ad, T. Piran, and L. N. Dacosta.
A catalogue of the voids in the IRAS 1.2-Jy survey.
Monthly Notices of the RAS, 287:790–798, June 1997.
doi: 10.1093/mnras/287.4.790.

A. Elyiv, F. Marulli, G. Pollina, M. Baldi, E. Branchini, A. Cimatti, and L. Moscardini.
Cosmic voids detection without density measurements.
Monthly Notices of the RAS, 448:642–653, March 2015.
doi: 10.1093/mnras/stv043.

A. A. Elyiv, I. D. Karachentsev, V. E. Karachentseva, O. V. Melnyk, and D. I. Makarov.
Low-density structures in the Local Universe. II. Nearby cosmic voids.
Astrophysical Bulletin, 68:1–13, January 2013.
doi: 10.1134/S199034131301001X.

A. E. Evrard, T. J. MacFarland, H. M. P. Couchman, J. M. Colberg, N. Yoshida, S. D. M. White, A. Jenkins, C. S. Frenk, F. R. Pearce, J. A. Peacock, and P. A. Thomas.
Galaxy Clusters in Hubble Volume Simulations: Cosmological Constraints from Sky Survey Populations.
Astrophysical Journal, 573:7–36, July 2002.
doi: 10.1086/340551.

P. A. Fairall and G. Kauffman.
Large-scale structures.
In A. Blanchard, L. Celnikier, M. Lachieze-Rey, and J. Tran Thanh Van, editors, *Physical Cosmology*, page 580, 1991.

G. R. Farrar and P. J. E. Peebles.
Interacting Dark Matter and Dark Energy.
Astrophysical Journal, 604:1–11, March 2004.
doi: 10.1086/381728.

F. Finelli, J. García-Bellido, A. Kovács, F. Paci, and I. Szapudi.
A Supervoid Explanation of the Cosmic Microwave Background Cold Spot.

In A. Heavens, J.-L. Starck, and A. Krone-Martins, editors, *Statistical Challenges in 21st Century Cosmology*, volume 306 of *IAU Symposium*, pages 153–155, May 2014a. doi: 10.1017/S1743921314013714.

F. Finelli, J. Garcia-Bellido, A. Kovacs, F. Paci, and I. Szapudi.
Supervoids in the WISE-2MASS catalogue imprinting Cold Spots in the Cosmic Microwave Background.
ArXiv e-prints, May 2014b.

R.A. Fisher.
Statistical methods for research workers.
Edinburgh Oliver & Boyd, 1925.

D. J. Fixsen.
The Temperature of the Cosmic Microwave Background.
Astrophysical Journal, 707:916–920, December 2009.
doi: 10.1088/0004-637X/707/2/916.

J. E. Forero-Romero, Y. Hoffman, S. Gottlöber, A. Klypin, and G. Yepes.
A dynamical classification of the cosmic web.
Monthly Notices of the RAS, 396:1815–1824, July 2009.
doi: 10.1111/j.1365-2966.2009.14885.x.

C. Foster and L. A. Nelson.
The Size, Shape, and Orientation of Cosmological Voids in the Sloan Digital Sky Survey.
Astrophysical Journal, 699:1252–1260, July 2009.
doi: 10.1088/0004-637X/699/2/1252.

L. Gao, S. D. M. White, A. Jenkins, F. Stoehr, and V. Springel.
The subhalo populations of ΛCDM dark haloes.
Monthly Notices of the RAS, 355:819–834, December 2004.
doi: 10.1111/j.1365-2966.2004.08360.x.

J. Garcia-Bellido and T. Haugbølle.
Confronting Lemaitre Tolman Bondi models with observational cosmology.
Journal of Cosmology and Astroparticle Physics, 4:003, April 2008.
doi: 10.1088/1475-7516/2008/04/003.

B. Garilli, L. Guzzo, M. Scodeggio, M. Bolzonella, U. Abbas, C. Adami, S. Arnouts, J. Bel, D. Bottini, E. Branchini, A. Cappi, J. Coupon, O. Cucciati, I. Davidzon, G. De Lucia, S. de la Torre, P. Franzetti, A. Fritz, M. Fumana, B. R. Granett, O. Ilbert, A. Iovino, J. Krywult, V. Le Brun, O. Le Fèvre, D. Maccagni, K. Małek, F. Marulli, H. J. McCracken, L. Paioro, M. Polletta, A. Pollo, H. Schlagenhaufer, L. A. M. Tasca, R. Tojeiro, D. Vergani, G. Zamorani, A. Zanichelli, A. Burden, C. Di Porto, A. Marchetti, C. Marinoni, Y. Mellier, L. Moscardini, R. C. Nichol, J. A. Peacock, W. J. Percival, S. Phleps, and M. Wolk.
The VIMOS Public Extragalactic Survey (VIPERS). First Data Release of 57 204 spectroscopic measurements.
Astronomy and Astrophysics, 562:A23, February 2014.
doi: 10.1051/0004-6361/201322790.

M. J. Geller and J. P. Huchra.
Mapping the universe.
Science, 246:897–903, November 1989.
doi: 10.1126/science.246.4932.897.

D. M. Goldberg and M. S. Vogeley.
Simulating Voids.
Astrophysical Journal, 605:1–6, April 2004.
doi: 10.1086/382143.

S. Gottlöber, E. L. Łokas, A. Klypin, and Y. Hoffman.
The structure of voids.
Monthly Notices of the RAS, 344:715–724, September 2003.
doi: 10.1046/j.1365-8711.2003.06850.x.

B. R. Granett, M. C. Neyrinck, and I. Szapudi.
An Imprint of Superstructures on the Microwave Background due to the Integrated Sachs-Wolfe Effect.
Astrophysical Journal, Letters, 683:L99, August 2008.
doi: 10.1086/591670.

S. A. Gregory and L. A. Thompson.
The Coma/A1367 supercluster and its environs.
Astrophysical Journal, 222:784–799, June 1978.
doi: 10.1086/156198.

Jan Niklas Grieb, Ariel G. Sánchez, Salvador Salazar-Albornoz, Román Scoccimarro, Martín Crocce, Claudio Dalla Vecchia, Francesco Montesano, Héctor Gil-Marín, Ashley J. Ross, Florian Beutler, Sergio Rodríguez-Torres, Chia-Hsun Chuang, Francisco Prada, Francisco-Shu Kitaura, Antonio J. Cuesta, Daniel J. Eisenstein, Will J. Percival, Mariana Vargas-Magana, Jeremy L. Tinker, Rita Tojeiro, Joel R. Brownstein, Claudia Maraston, Robert C. Nichol, Matthew D. Olmstead, Lado Samushia, Hee-Jong Seo, Alina Streblyanska, and Gong-bo Zhao.
The clustering of galaxies in the completed SDSS-III Baryon Oscillation Spectroscopic Survey: Cosmological implications of the Fourier space wedges of the final sample, November 2016.

William Gropp, Ewing Lusk, Nathan Doss, and Anthony Skjellum.
A high-performance, portable implementation of the {MPI} message passing interface standard.
Parallel Computing, 22(6):789 – 828, 1996.
ISSN 0167-8191.
doi: http://dx.doi.org/10.1016/0167-8191(96)00024-5.

J. E. Gunn and J. R. Gott, III.
On the Infall of Matter Into Clusters of Galaxies and Some Effects on Their Evolution.
Astrophysical Journal, 176:1, August 1972.
doi: 10.1086/151605.

A. H. Guth.
Inflationary universe: A possible solution to the horizon and flatness problems.
Physical Review D, 23:347–356, January 1981.
doi: 10.1103/PhysRevD.23.347.

L. Guzzo and The Vipers Team.
VIPERS: An Unprecedented View of Galaxies and Large-scale Structure Halfway Back in the Life of the Universe.
The Messenger, 151:41–46, March 2013.

O. Hahn, C. Porciani, A. Dekel, and C. M. Carollo.
Tidal effects and the environment dependence of halo assembly.
Monthly Notices of the RAS, 398:1742–1756, October 2009.
doi: 10.1111/j.1365-2966.2009.15271.x.

N. Hamaus, A. Pisani, P. M. Sutter, G. Lavaux, S. Escoffier, B. D. Wandelt, and J. Weller.
Constraints on Cosmology and Gravity from the Dynamics of Voids.
Physical Review Letters, 117(9):091302, August 2016.
doi: 10.1103/PhysRevLett.117.091302.

Nico Hamaus, P. M. Sutter, and Benjamin D. Wandelt.
Universal density profile for cosmic voids.
Phys. Rev. Lett., 112:251302, Jun 2014.
doi: 10.1103/PhysRevLett.112.251302.

M. A. Hausman, D. W. Olson, and B. D. Roth.
The evolution of voids in the expanding universe.
Astrophysical Journal, 270:351–359, July 1983.
doi: 10.1086/161128.

F. Hoyle and M. S. Vogeley.
Voids in the Point Source Catalogue Survey and the Updated Zwicky Catalog.
Astrophysical Journal, 566:641–651, February 2002.
doi: 10.1086/338340.

E. Hubble.
A Relation between Distance and Radial Velocity among Extra-Galactic Nebulae.
Proceedings of the National Academy of Science, 15:168–173, March 1929.
doi: 10.1073/pnas.15.3.168.

E. P. Hubble.
Realm of the Nebulae.
1936.

J. P. Huchra, M. J. Geller, V. de Lapparent, and R. Burg.
The CFA Redshift Survey.
In J. Audouze, M.-C. Pelletan, A. Szalay, Y. B. Zel'dovich, and P. J. E. Peebles, editors, *Large Scale Structures of the Universe*, volume 130 of *IAU Symposium*, page 105, 1988.

V. Icke.
Voids and filaments.
Monthly Notices of the RAS, 206:1P–3P, January 1984.
doi: 10.1093/mnras/206.1.1P.

K. T. Inoue.
On the origin of the cold spot.
Monthly Notices of the RAS, 421:2731–2736, April 2012.
doi: 10.1111/j.1365-2966.2012.20513.x.

K. T. Inoue and J. Silk.
Local Voids as the Origin of Large-Angle Cosmic Microwave Background Anomalies. I.
Astrophysical Journal, 648:23–30, September 2006.
doi: 10.1086/505636.

K. T. Inoue and J. Silk.
Local Voids as the Origin of Large-Angle Cosmic Microwave Background Anomalies: The Effect of a Cosmological Constant.
Astrophysical Journal, 664:650–659, August 2007.
doi: 10.1086/517603.

K. T. Inoue, N. Sakai, and K. Tomita.
Evidence of Quasi-linear Super-structures in the Cosmic Microwave Background and Galaxy Distribution.
Astrophysical Journal, 724:12–25, November 2010.
doi: 10.1088/0004-637X/724/1/12.

M. Jõeveer, J. Einasto, and E. Tago.
Spatial distribution of galaxies and of clusters of galaxies in the southern galactic hemisphere.
Monthly Notices of the RAS, 185:357–370, November 1978.
doi: 10.1093/mnras/185.2.357.

J. H. Jeans.
The Stability of a Spherical Nebula.
Philosophical Transactions of the Royal Society of London Series A, 199:1–53, 1902.
doi: 10.1098/rsta.1902.0012.

E. Jennings, Y. Li, and W. Hu.
The abundance of voids and the excursion set formalism.
Monthly Notices of the RAS, 434:2167–2181, September 2013.
doi: 10.1093/mnras/stt1169.

G. Jungman, M. Kamionkowski, and K. Griest.

Supersymmetric dark matter.
Physics Reports, 267:195–373, March 1996.
doi: 10.1016/0370-1573(95)00058-5.

N. Kaiser.
On the spatial correlations of Abell clusters.
Astrophysical Journal, Letters, 284:L9–L12, September 1984.
doi: 10.1086/184341.

G. Kauffmann and A. P. Fairall.
Voids in the distribution of galaxies - an assessment of their significance and derivation of a void spectrum.
Monthly Notices of the RAS, 248:313–324, January 1991.
doi: 10.1093/mnras/248.2.313.

G. Kauffmann, J. M. Colberg, A. Diaferio, and S. D. M. White.
Clustering of galaxies in a hierarchical universe - II. Evolution to high redshift.
Monthly Notices of the RAS, 307:529–536, August 1999.
doi: 10.1046/j.1365-8711.1999.02711.x.

R. P. Kirshner, A. Oemler, Jr., P. L. Schechter, and S. A. Shectman.
A million cubic megaparsec void in Bootes.
Astrophysical Journal, Letters, 248:L57–L60, September 1981.
doi: 10.1086/183623.

R. P. Kirshner, A. Oemler, Jr., P. L. Schechter, and S. A. Shectman.
A survey of the Bootes void.
Astrophysical Journal, 314:493–506, March 1987.
doi: 10.1086/165080.

F.-S. Kitaura, C.-H. Chuang, Y. Liang, C. Zhao, C. Tao, S. Rodríguez-Torres, D. J. Eisenstein, H. Gil-Marín, J.-P. Kneib, C. McBride, W. J. Percival, A. J. Ross, A. G. Sánchez, J. Tinker, R. Tojeiro, M. Vargas-Magana, and G.-B. Zhao.
Signatures of the Primordial Universe from Its Emptiness: Measurement of Baryon Acoustic Oscillations from Minima of the Density Field.
Physical Review Letters, 116(17):171301, April 2016.
doi: 10.1103/PhysRevLett.116.171301.

A. Kovács and J. García-Bellido.

Cosmic troublemakers: the Cold Spot, the Eridanus supervoid, and the Great Walls.
Monthly Notices of the RAS, 462:1882–1893, October 2016.
doi: 10.1093/mnras/stw1752.

A. Kovács and B. R. Granett.
Cold imprint of supervoids in the cosmic microwave background re-considered with Planck and Baryon Oscillation Spectroscopic Survey DR10.
Monthly Notices of the RAS, 452:1295–1302, September 2015.
doi: 10.1093/mnras/stv1371.

A. Kovács and I. Szapudi.
Star-galaxy separation strategies for WISE-2MASS all-sky infrared galaxy catalogues.
Monthly Notices of the RAS, 448:1305–1313, April 2015.
doi: 10.1093/mnras/stv063.

K. Kreckel, J. H. van Gorkom, B. Beygu, R. van de Weygaert, J. M. van der Hulst, M. A. Aragon-Calvo, and R. F. Peletier.
The Void Galaxy Survey: Galaxy Evolution and Gas Accretion in Voids.
ArXiv e-prints, October 2014.

C. Lacey.
Semi-Analytical Models of Galaxy Formation.
In M. Umemura and H. Susa, editors, *The Physics of Galaxy Formation*, volume 222 of *Astronomical Society of the Pacific Conference Series*, page 273, 2001.

R. Laureijs, J. Amiaux, S. Arduini, J. . Augueres, J. Brinchmann, R. Cole, M. Cropper, C. Dabin, L. Duvet, A. Ealet, and et al.
Euclid Definition Study Report.
ArXiv e-prints, October 2011.

G. Lavaux and B. D. Wandelt.
Precision cosmology with voids: definition, methods, dynamics.
Monthly Notices of the RAS, 403:1392–1408, April 2010.
doi: 10.1111/j.1365-2966.2010.16197.x.

G. Lavaux and B. D. Wandelt.
Precision Cosmography with Stacked Voids.
Astrophysical Journal, 754:109, August 2012.
doi: 10.1088/0004-637X/754/2/109.

J. Lee and D. Park.
Rotation of Cosmic Voids and Void Spin Statistics.
Astrophysical Journal, 652:1–5, November 2006.
doi: 10.1086/507936.

J. Lee and D. Park.
Constraining the Dark Energy Equation of State with Cosmic Voids.
Astrophysical Journal, Letters, 696:L10–L12, May 2009.
doi: 10.1088/0004-637X/696/1/L10.

J. C. Lee, J. J. Salzer, D. A. Law, and J. L. Rosenberg.
Erratum: Emission-Line Galaxy Surveys as Probes of the Spatial Distribution of Dwarf Galaxies. I. The University of Michigan Survey.
Astrophysical Journal, 538:980–984, August 2000.
doi: 10.1086/309187.

X.-D. Li, C. Park, C. G. Sabiu, and J. Kim.
Cosmological constraints from the redshift dependence of the Alcock-Paczynski test and volume effect: galaxy two-point correlation function.
Monthly Notices of the RAS, 450:807–814, June 2015.
doi: 10.1093/mnras/stv622.

P. B. Lilje and O. Lahav.
Evolution of velocity and density fields around clusters of galaxies.
Astrophysical Journal, 374:29–43, June 1991.
doi: 10.1086/170094.

E. V. Linder.
Exploring the Expansion History of the Universe.
Physical Review Letters, 90(9):091301, March 2003.
doi: 10.1103/PhysRevLett.90.091301.

U. Lindner, J. Einasto, M. Einasto, W. Freudling, K. Fricke, and E. Tago.
The structure of supervoids. I. Void hierarchy in the Northern Local Supervoid.
Astronomy and Astrophysics, 301:329, September 1995.

M. López-Corredoira.
Alcock-Paczyński Cosmological Test.
Astrophysical Journal, 781:96, February 2014.

doi: 10.1088/0004-637X/781/2/96.

S. J. Maddox, G. Efstathiou, W. J. Sutherland, and J. Loveday.
Galaxy correlations on large scales.
Monthly Notices of the RAS, 242:43P–47P, January 1990.
doi: 10.1093/mnras/242.1.43P.

H. Martel and I. Wasserman.
Simulation of cosmological voids in Lambda greater than 0 Friedmann models.
Astrophysical Journal, 348:1–25, January 1990.
doi: 10.1086/168208.

F. Marulli, A. Veropalumbo, and M. Moresco.
CosmoBolognaLib: C++ libraries for cosmological calculations.
Astronomy and Computing, 14:35–42, January 2016.
doi: 10.1016/j.ascom.2016.01.005.

F. Melia and M. Lopez-Corredoira.
Alcock-Paczynski Test with Model-independent BAO Data.
ArXiv e-prints, March 2015.

B. Ménard, T. Hamana, M. Bartelmann, and N. Yoshida.
Improving the accuracy of cosmic magnification statistics.
Astronomy and Astrophysics, 403:817–828, June 2003.
doi: 10.1051/0004-6361:20030406.

D. Micheletti, A. Iovino, A. J. Hawken, B. R. Granett, M. Bolzonella, A. Cappi, L. Guzzo, U. Abbas, C. Adami, S. Arnouts, J. Bel, D. Bottini, E. Branchini, J. Coupon, O. Cucciati, I. Davidzon, G. De Lucia, S. de la Torre, A. Fritz, P. Franzetti, M. Fumana, B. Garilli, O. Ilbert, J. Krywult, V. Le Brun, O. Le Fèvre, D. Maccagni, K. Małek, F. Marulli, H. J. McCracken, M. Polletta, A. Pollo, C. Schimd, M. Scodeggio, L. A. M. Tasca, R. Tojeiro, D. Vergani, A. Zanichelli, A. Burden, C. Di Porto, A. Marchetti, C. Marinoni, Y. Mellier, T. Moutard, L. Moscardini, R. C. Nichol, J. A. Peacock, W. J. Percival, and G. Zamorani.
The VIMOS Public Extragalactic Redshift Survey. Searching for cosmic voids.
Astronomy and Astrophysics, 570:A106, October 2014.
doi: 10.1051/0004-6361/201424107.

H. J. Mo and S. D. M. White.
An analytic model for the spatial clustering of dark matter haloes.

Monthly Notices of the RAS, 282:347–361, September 1996.
doi: 10.1093/mnras/282.2.347.

S. Nadathur and S. Hotchkiss.
A robust public catalogue of voids and superclusters in the SDSS Data Release 7 galaxy surveys.
Monthly Notices of the RAS, 440:1248–1262, May 2014.
doi: 10.1093/mnras/stu349.

S. Nadathur, M. Lavinto, S. Hotchkiss, and S. Räsänen.
Can a supervoid explain the cold spot?
Physical Review D, 90(10):103510, November 2014.
doi: 10.1103/PhysRevD.90.103510.

K. Naidoo, A. Benoit-Lévy, and O. Lahav.
Could multiple voids explain the cosmic microwave background Cold Spot anomaly?
Monthly Notices of the RAS, 459:L71–L75, June 2016.
doi: 10.1093/mnrasl/slw043.

M. C. Neyrinck.
ZOBOV: a parameter-free void-finding algorithm.
Monthly Notices of the RAS, 386:2101–2109, June 2008.
doi: 10.1111/j.1365-2966.2008.13180.x.

M. C. Neyrinck, N. Y. Gnedin, and A. J. S. Hamilton.
VOBOZ: an almost-parameter-free halo-finding algorithm.
Monthly Notices of the RAS, 356:1222–1232, February 2005.
doi: 10.1111/j.1365-2966.2004.08505.x.

N. Padilla, D. Paz, M. Lares, L. Ceccarelli, D. Garcia Lambas, Y.-C. Cai, and B. Li.
Void Dynamics.
ArXiv e-prints, October 2014.

N. D. Padilla, L. Ceccarelli, and D. G. Lambas.
Spatial and dynamical properties of voids in a Λ cold dark matter universe.
Monthly Notices of the RAS, 363:977–990, November 2005.
doi: 10.1111/j.1365-2966.2005.09500.x.

T. Padmanabhan.

Structure Formation in the Universe.
May 1993.

D. C. Pan, M. S. Vogeley, F. Hoyle, Y.-Y. Choi, and C. Park.
Cosmic voids in Sloan Digital Sky Survey Data Release 7.
Monthly Notices of the RAS, 421:926–934, April 2012.
doi: 10.1111/j.1365-2966.2011.20197.x.

D. Park and J. Lee.
Void-Supercluster Alignments.
Astrophysical Journal, 665:96–101, August 2007.
doi: 10.1086/519449.

S. G. Patiri, J. E. Betancort-Rijo, F. Prada, A. Klypin, and S. Gottlöber.
Statistics of voids in the two-degree Field Galaxy Redshift Survey.
Monthly Notices of the RAS, 369:335–348, June 2006.
doi: 10.1111/j.1365-2966.2006.10305.x.

J. A. Peacock and S. J. Dodds.
Non-linear evolution of cosmological power spectra.
Monthly Notices of the RAS, 280:L19–L26, June 1996.
doi: 10.1093/mnras/280.3.L19.

P. J. E. Peebles.
The large-scale structure of the universe.
1980.

P. J. E. Peebles.
The Void Phenomenon.
Astrophysical Journal, 557:495–504, August 2001.
doi: 10.1086/322254.

S. J. Penny, M. J. I. Brown, K. A. Pimbblet, M. E. Cluver, D. J. Croton, M. S. Owers, R. Lange, M. Alpaslan, I. Baldry, J. Bland-Hawthorn, S. Brough, S. P. Driver, B. W. Holwerda, A. M. Hopkins, T. H. Jarrett, D. H. Jones, L. S. Kelvin, M. A. Lara-López, J. Liske, A. R. López-Sánchez, J. Loveday, M. Meyer, P. Norberg, A. S. G. Robotham, and M. Rodrigues.
Galaxy And Mass Assembly (GAMA): the bright void galaxy population in the optical and mid-IR.

Monthly Notices of the RAS, 453:3519–3539, November 2015.
doi: 10.1093/mnras/stv1926.

S. Perlmutter, G. Aldering, G. Goldhaber, R. A. Knop, P. Nugent, P. G. Castro, S. Deustua, S. Fabbro, A. Goobar, D. E. Groom, I. M. Hook, A. G. Kim, M. Y. Kim, J. C. Lee, N. J. Nunes, R. Pain, C. R. Pennypacker, R. Quimby, C. Lidman, R. S. Ellis, M. Irwin, R. G. McMahon, P. Ruiz-Lapuente, N. Walton, B. Schaefer, B. J. Boyle, A. V. Filippenko, T. Matheson, A. S. Fruchter, N. Panagia, H. J. M. Newberg, W. J. Couch, and T. S. C. Project.
Measurements of Ω and Λ from 42 High-Redshift Supernovae.
The Astrophysical Journal, 517:565–586, June 1999.
doi: 10.1086/307221.

A. Pisani, P. M. Sutter, N. Hamaus, E. Alizadeh, R. Biswas, B. D. Wandelt, and C. M. Hirata.
Counting voids to probe dark energy.
Physical Review D, 92(8):083531, October 2015.
doi: 10.1103/PhysRevD.92.083531.

Planck Collaboration, P. A. R. Ade, N. Aghanim, M. Arnaud, M. Ashdown, J. Aumont, C. Baccigalupi, A. J. Banday, R. B. Barreiro, J. G. Bartlett, and et al.
Planck 2015 results. XIII. Cosmological parameters.
Astronomy and Astrophysics, 594:A13, September 2016.
doi: 10.1051/0004-6361/201525830.

E. Platen, R. van de Weygaert, and B. J. T. Jones.
A cosmic watershed: the WVF void detection technique.
Monthly Notices of the RAS, 380:551–570, September 2007.
doi: 10.1111/j.1365-2966.2007.12125.x.

E. Platen, R. van de Weygaert, and B. J. T. Jones.
Alignment of voids in the cosmic web.
Monthly Notices of the RAS, 387:128–136, June 2008.
doi: 10.1111/j.1365-2966.2008.13019.x.

M. Plionis and S. Basilakos.
The size and shape of local voids.
Monthly Notices of the RAS, 330:399–404, February 2002.

doi: 10.1046/j.1365-8711.2002.05069.x.

G. Pollina, M. Baldi, F. Marulli, and L. Moscardini.
Cosmic voids in coupled dark energy cosmologies: the impact of halo bias.
Monthly Notices of the RAS, 455:3075–3085, January 2016.
doi: 10.1093/mnras/stv2503.

D. Potter, J. Stadel, and R. Teyssier.
PKDGRAV3: Beyond Trillion Particle Cosmological Simulations for the Next Era of Galaxy Surveys.
ArXiv e-prints, September 2016.

W. H. Press and P. Schechter.
Formation of Galaxies and Clusters of Galaxies by Self-Similar Gravitational Condensation.
Astrophysical Journal, 187:425–438, February 1974.
doi: 10.1086/152650.

M. J. Rees and D. W. Sciama.
Large-scale Density Inhomogeneities in the Universe.
Nature, 217:511–516, February 1968.
doi: 10.1038/217511a0.

E. Regos and M. J. Geller.
The evolution of void-filled cosmological structures.
Astrophysical Journal, 377:14–28, August 1991.
doi: 10.1086/170332.

Adam G. Riess, Alexei V. Filippenko, Peter Challis, Alejandro Clocchiattia, Alan Diercks, Peter M. Garnavich, Ron L. Gilliland, Craig J. Hogan, Saurabh Jha, Robert P. Kirshner, B. Leibundgut, M. M. Phillips, David Reiss, Brian P. Schmidt, Robert A. Schommer, R. Chris Smith, J. Spyromilio, Christopher Stubbs, Nicholas B. Suntzeff, and John Tonry.
Observational Evidence from Supernovae for an Accelerating Universe and a Cosmological Constant.
Astron.J.116:1009-1038,1998, May 1998.
doi: 10.1086/300499.

R. R. Rojas, M. S. Vogeley, F. Hoyle, and J. Brinkmann.

Spectroscopic Properties of Void Galaxies in the Sloan Digital Sky Survey.
Astrophysical Journal, 624:571–585, May 2005.
doi: 10.1086/428476.

T. Ronconi and F. Marulli.
In preparation.
2017.

T. Ronconi, F. Marulli, L. Moscardini, and et al.
In preparation.
2017.

V. C. Rubin and W. K. Ford, Jr.
Rotation of the Andromeda Nebula from a Spectroscopic Survey of Emission Regions.
Astrophysical Journal, 159:379, February 1970.
doi: 10.1086/150317.

R. K. Sachs and A. M. Wolfe.
Perturbations of a Cosmological Model and Angular Variations of the Microwave Background.
Astrophysical Journal, 147:73, January 1967.
doi: 10.1086/148982.

J. J. Salzer, M. M. Hanson, and G. Gavazzi.
The relative spatial distributions of high- and low-luminosity galaxies toward Coma.
Astrophysical Journal, 353:39–50, April 1990.
doi: 10.1086/168587.

C. Sánchez, J. Clampitt, A. Kovacs, B. Jain, J. García-Bellido, S. Nadathur, D. Gruen, N. Hamaus, D. Huterer, P. Vielzeuf, A. Amara, C. Bonnett, J. DeRose, W. G. Hartley, M. Jarvis, O. Lahav, R. Miquel, E. Rozo, E. S. Rykoff, E. Sheldon, R. H. Wechsler, J. Zuntz, T. M. C. Abbott, F. B. Abdalla, J. Annis, A. Benoit-Lévy, G. M. Bernstein, R. A. Bernstein, E. Bertin, D. Brooks, E. Buckley-Geer, A. C. Rosell, M. C. Kind, J. Carretero, M. Crocce, C. E. Cunha, C. B. D'Andrea, L. N. da Costa, S. Desai, H. T. Diehl, J. P. Dietrich, P. Doel, A. E. Evrard, A. F. Neto, B. Flaugher, P. Fosalba, J. Frieman, E. Gaztanaga, R. A. Gruendl, G. Gutierrez, K. Honscheid, D. J. James, E. Krause, K. Kuehn, M. Lima, M. A. G. Maia, J. L. Marshall, P. Melchior, A. A. Plazas, K. Reil, A. K. Romer, E. Sanchez, M. Schubnell, I. Sevilla-Noarbe, R. C. Smith,

M. Soares-Santos, F. Sobreira, E. Suchyta, G. Tarle, D. Thomas, A. R. Walker, J. Weller, and DES Collaboration.
Cosmic voids and void lensing in the Dark Energy Survey Science Verification data.
Monthly Notices of the RAS, 465:746–759, February 2017.
doi: 10.1093/mnras/stw2745.

W. E. Schaap.
DTFE: the Delaunay Tessellation Field Estimator.
PhD thesis, Kapteyn Astronomical Institute <EMAIL>w_schaap@live.nl</EMAIL>, 2007.

W. E. Schaap and R. van de Weygaert.
Continuous fields and discrete samples: reconstruction through Delaunay tessellations.
Astronomy and Astrophysics, 363:L29–L32, November 2000.

Brian P. Schmidt, Nicholas B. Suntzeff, M. M. Phillips, Robert A. Schommer, Alejandro Clocchiatti, Robert P. Kirshner, Peter Garnavich, Peter Challis, B. Leibundgut, J. Spyromilio, Adam G. Riess, Alexei V. Filippenko, Mario Hamuy, R. Chris Smith, Craig Hogan, Christopher Stubbs, Alan Diercks, David Reiss, Ron Gilliland, John Tonry, Jose Maza, A. Dressler, J. Walsh, and R. Ciardullo.
The High-Z Supernova Search: Measuring Cosmic Deceleration and Global Cur vature of the Universe Using Type Ia Supernovae.
Astrophys.J. 507 (1998) 46-63, May 1998.
doi: 10.1086/306308.

R. Scoccimarro.
The Bispectrum: From Theory to Observations.
Astrophysical Journal, 544:597–615, December 2000.
doi: 10.1086/317248.

S. Shandarin, H. A. Feldman, K. Heitmann, and S. Habib.
Shapes and sizes of voids in the Lambda cold dark matter universe: excursion set approach.
Monthly Notices of the RAS, 367:1629–1640, April 2006.
doi: 10.1111/j.1365-2966.2006.10062.x.

R. K. Sheth and R. van de Weygaert.

A hierarchy of voids: much ado about nothing.
Monthly Notices of the RAS, 350:517–538, May 2004.
doi: 10.1111/j.1365-2966.2004.07661.x.

D. Spergel, N. Gehrels, J. Breckinridge, M. Donahue, A. Dressler, B. S. Gaudi, T. Greene, O. Guyon, C. Hirata, J. Kalirai, N. J. Kasdin, W. Moos, S. Perlmutter, M. Postman, B. Rauscher, J. Rhodes, Y. Wang, D. Weinberg, J. Centrella, W. Traub, C. Baltay, J. Colbert, D. Bennett, A. Kiessling, B. Macintosh, J. Merten, M. Mortonson, M. Penny, E. Rozo, D. Savransky, K. Stapelfeldt, Y. Zu, C. Baker, E. Cheng, D. Content, J. Dooley, M. Foote, R. Goullioud, K. Grady, C. Jackson, J. Kruk, M. Levine, M. Melton, C. Peddie, J. Ruffa, and S. Shaklan.
Wide-Field InfraRed Survey Telescope-Astrophysics Focused Telescope Assets WFIRST-AFTA Final Report.
ArXiv e-prints, May 2013a.

D. Spergel, N. Gehrels, J. Breckinridge, M. Donahue, A. Dressler, B. S. Gaudi, T. Greene, O. Guyon, C. Hirata, J. Kalirai, N. J. Kasdin, W. Moos, S. Perlmutter, M. Postman, B. Rauscher, J. Rhodes, Y. Wang, D. Weinberg, J. Centrella, W. Traub, C. Baltay, J. Colbert, D. Bennett, A. Kiessling, B. Macintosh, J. Merten, M. Mortonson, M. Penny, E. Rozo, D. Savransky, K. Stapelfeldt, Y. Zu, C. Baker, E. Cheng, D. Content, J. Dooley, M. Foote, R. Goullioud, K. Grady, C. Jackson, J. Kruk, M. Levine, M. Melton, C. Peddie, J. Ruffa, and S. Shaklan.
WFIRST-2.4: What Every Astronomer Should Know.
ArXiv e-prints, May 2013b.

D. N. Spergel, L. Verde, H. V. Peiris, E. Komatsu, M. R. Nolta, C. L. Bennett, M. Halpern, G. Hinshaw, N. Jarosik, A. Kogut, M. Limon, S. S. Meyer, L. Page, G. S. Tucker, J. L. Weiland, E. Wollack, and E. L. Wright.
First-Year Wilkinson Microwave Anisotropy Probe (WMAP) Observations: Determination of Cosmological Parameters.
Astrophysical Journal, Supplement, 148:175–194, September 2003.
doi: 10.1086/377226.

V. Springel, S. D. M. White, A. Jenkins, C. S. Frenk, N. Yoshida, L. Gao, J. Navarro, R. Thacker, D. Croton, J. Helly, J. A. Peacock, S. Cole, P. Thomas, H. Couchman, A. Evrard, J. Colberg, and F. Pearce.
Simulations of the formation, evolution and clustering of galaxies and quasars.

Nature, 435:629–636, June 2005.
doi: 10.1038/nature03597.

P. M. Sutter, G. Lavaux, B. D. Wandelt, and D. H. Weinberg.
A First Application of the Alcock-Paczynski Test to Stacked Cosmic Voids.
Astrophysical Journal, 761:187, December 2012.
doi: 10.1088/0004-637X/761/2/187.

P. M. Sutter, G. Lavaux, B. D. Wandelt, D. H. Weinberg, and M. S. Warren.
The dark matter of galaxy voids.
Monthly Notices of the RAS, 438:3177–3187, March 2014a.
doi: 10.1093/mnras/stt2425.

P. M. Sutter, A. Pisani, B. D. Wandelt, and D. H. Weinberg.
A measurement of the Alcock-Paczyński effect using cosmic voids in the SDSS.
Monthly Notices of the RAS, 443:2983–2990, October 2014b.
doi: 10.1093/mnras/stu1392.

P. M. Sutter, E. Carlesi, B. D. Wandelt, and A. Knebe.
On the observability of coupled dark energy with cosmic voids.
Monthly Notices of the RAS, 446:L1–L5, January 2015a.
doi: 10.1093/mnrasl/slu155.

P. M. Sutter, G. Lavaux, N. Hamaus, A. Pisani, B. D. Wandelt, M. Warren,
F. Villaescusa-Navarro, P. Zivick, Q. Mao, and B. B. Thompson.
VIDE: The Void IDentification and Examination toolkit.
Astronomy and Computing, 9:1–9, March 2015b.
doi: 10.1016/j.ascom.2014.10.002.

I. Szapudi, A. Kovács, B. R. Granett, Z. Frei, J. Silk, J. Garcia-Bellido, W. Burgett,
S. Cole, P. W. Draper, D. J. Farrow, N. Kaiser, E. A. Magnier, N. Metcalfe, J. S.
Morgan, P. Price, J. Tonry, and R. Wainscoat.
The Cold Spot in the Cosmic Microwave Background: the Shadow of a Supervoid.
ArXiv e-prints, June 2014.

S. Tavasoli, K. Vasei, and R. Mohayaee.
The challenge of large and empty voids in the SDSS DR7 redshift survey.
Astronomy and Astrophysics, 553:A15, May 2013.
doi: 10.1051/0004-6361/201220774.

M. Tegmark, M. R. Blanton, M. A. Strauss, F. Hoyle, D. Schlegel, R. Scoccimarro, M. S. Vogeley, D. H. Weinberg, I. Zehavi, A. Berlind, T. Budavari, A. Connolly, D. J. Eisenstein, D. Finkbeiner, J. A. Frieman, J. E. Gunn, A. J. S. Hamilton, L. Hui, B. Jain, D. Johnston, S. Kent, H. Lin, R. Nakajima, R. C. Nichol, J. P. Ostriker, A. Pope, R. Scranton, U. Seljak, R. K. Sheth, A. Stebbins, A. S. Szalay, I. Szapudi, L. Verde, Y. Xu, J. Annis, N. A. Bahcall, J. Brinkmann, S. Badsurles, F. J. Castander, I. Csabai, J. Loveday, M. Doi, M. Fukugita, J. R. Gott, III, G. Hennessy, D. W. Hogg, Ž. Ivezić, G. R. Knapp, D. Q. Lamb, B. C. Lee, R. H. Lupton, T. A. McKay, P. Kunszt, J. A. Munn, L. O'Connell, J. Peoples, J. R. Pier, M. Richmond, C. Rockosi, D. P. Schneider, C. Stoughton, D. L. Tucker, D. E. Vanden Berk, B. Yanny, D. G. York, and SDSS Collaboration.
The Three-Dimensional Power Spectrum of Galaxies from the Sloan Digital Sky Survey.
Astrophysical Journal, 606:702–740, May 2004.
doi: 10.1086/382125.

L. A. Thompson.
Markarian galaxies and voids in the galaxy distribution.
Astrophysical Journal, 266:446–450, March 1983.
doi: 10.1086/160791.

Laird A. Thompson and Stephen A. Gregory.
An Historical View: The Discovery of Voids in the Galaxy Distribution, September 2011.

A. V. Tikhonov and I. D. Karachentsev.
Minivoids in the Local Volume.
Astrophysical Journal, 653:969–976, December 2006.
doi: 10.1086/508981.

A. V. Tikhonov, S. Gottlöber, G. Yepes, and Y. Hoffman.
The sizes of minivoids in the local Universe: an argument in favour of a warm dark matter model?
Monthly Notices of the RAS, 399:1611–1621, November 2009.
doi: 10.1111/j.1365-2966.2009.15381.x.

J. L. Tinker and C. Conroy.
The Void Phenomenon Explained.

Astrophysical Journal, 691:633–639, January 2009.
doi: 10.1088/0004-637X/691/1/633.

M. A. M. van de Weygaert.
Voids and the geometry of large scale structure.
PhD thesis, Ph. D. thesis, University of Leiden (1991), 1991.

R. van de Weygaert and V. Icke.
Fragmenting the universe. II - Voronoi vertices as Abell clusters.
Astronomy and Astrophysics, 213:1–9, April 1989.

R. van de Weygaert and E. Platen.
Cosmic Voids: Structure, Dynamics and Galaxies.
In *International Journal of Modern Physics Conference Series*, volume 1 of *International Journal of Modern Physics Conference Series*, pages 41–66, 2011.
doi: 10.1142/S2010194511000092.

R. van de Weygaert and W. Schaap.
The Cosmic Web: Geometric Analysis.
In V. J. Martínez, E. Saar, E. Martínez-González, and M.-J. Pons-Bordería, editors, *Data Analysis in Cosmology*, volume 665 of *Lecture Notes in Physics, Berlin Springer Verlag*, pages 291–413, 2009.
doi: 10.1007/978-3-540-44767-2_11.

R. van de Weygaert and E. van Kampen.
Voids in Gravitational Instability Scenarios - Part One - Global Density and Velocity Fields in an Einstein - De-Sitter Universe.
Monthly Notices of the RAS, 263:481, July 1993.
doi: 10.1093/mnras/263.2.481.

R. van de Weygaert, M. A. Aragon-Calvo, B. J. T. Jones, and E. Platen.
Geometry and Morphology of the Cosmic Web: Analyzing Spatial Patterns in the Universe.
ArXiv e-prints, December 2009.

H. E. S. Velten, R. F. vom Marttens, and W. Zimdahl.
Aspects of the cosmological "coincidence problem".
Eur.Phys.J. C74 (2014) 11, 3160, October 2014.
doi: 10.1140/epjc/s10052-014-3160-4.

P. Vielva, E. Martínez-González, R. B. Barreiro, J. L. Sanz, and L. Cayón.
Detection of Non-Gaussianity in the Wilkinson Microwave Anisotropy Probe First-Year Data Using Spherical Wavelets.
Astrophysical Journal, 609:22–34, July 2004.
doi: 10.1086/421007.

M. G. Voronoi.
Nouvelles applications des parametres continus a la theorie des formes quadratiques.
J. Reine Angew. Math., 134:1028–1044, January 1908.

C. Wetterich.
An asymptotically vanishing time-dependent cosmological ”constant”.
Astronomy and Astrophysics, 301:321, September 1995.

L. F. Yang, M. C. Neyrinck, M. A. Aragón-Calvo, B. Falck, and J. Silk.
Warmth elevating the depths: shallower voids with warm dark matter.
Monthly Notices of the RAS, 451:3606–3614, August 2015.
doi: 10.1093/mnras/stv1087.

Y. B. Zel'dovich.
Gravitational instability: An approximate theory for large density perturbations.
Astronomy and Astrophysics, 5:84–89, March 1970.

P. Zivick, P. M. Sutter, B. D. Wandelt, B. Li, and T. Y. Lam.
Using cosmic voids to distinguish f(R) gravity in future galaxy surveys.
Monthly Notices of the RAS, 451:4215–4222, August 2015.
doi: 10.1093/mnras/stv1209.

F. Zwicky.
On the Masses of Nebulae and of Clusters of Nebulae.
Astrophysical Journal, 86:217, October 1937.
doi: 10.1086/143864.